STATE OF THE CLIMATE IN 2019

GLOBAL OCEANS

Rick Lumpkin, Ed.

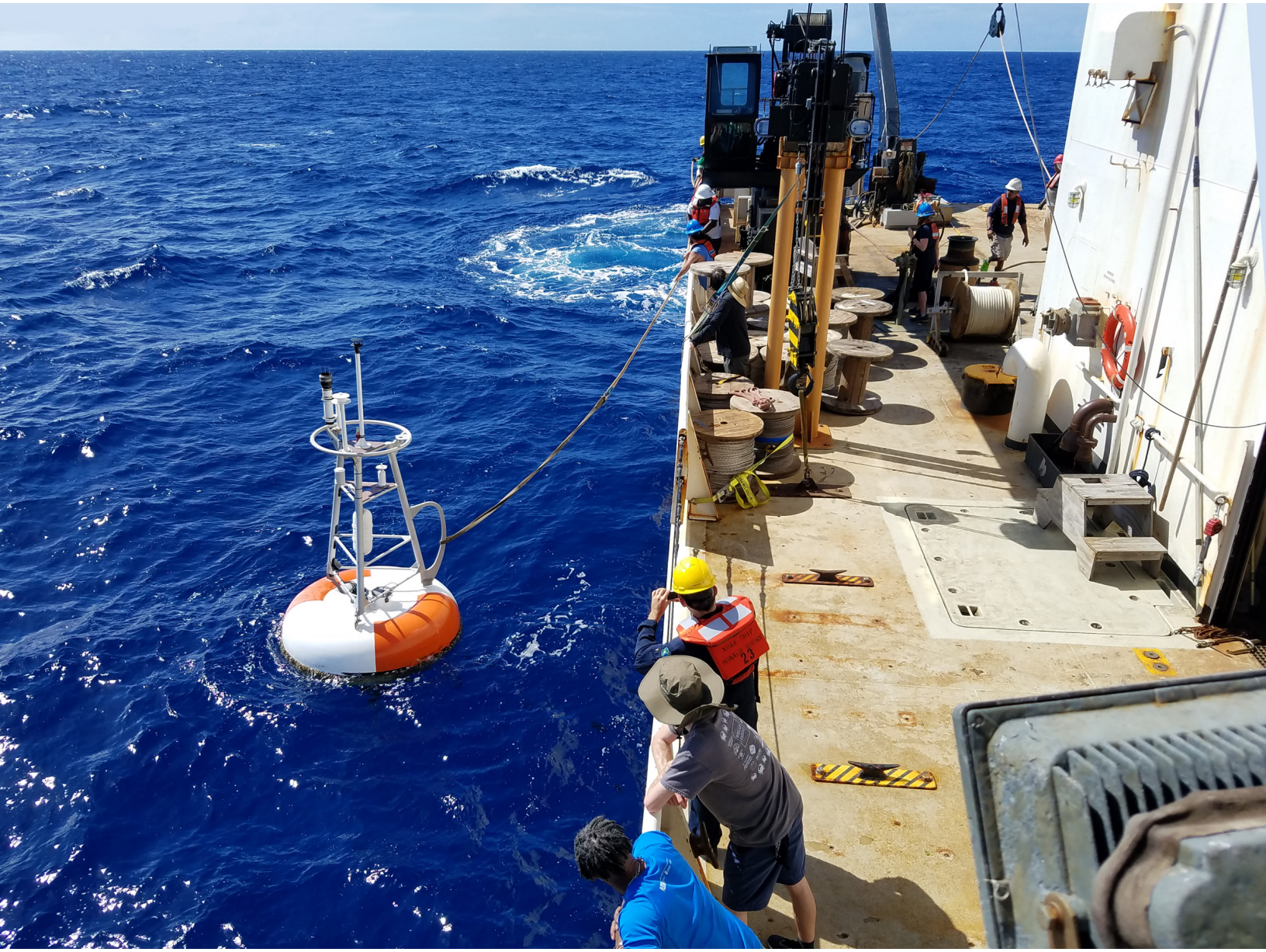

Special Supplement to the Bulletin of the American Meteorological Society Vol.101, No. 7, July, 2020

https://doi.org/10.1175/BAMS-D-XX-XXXX.1

Corresponding author: Rick Lumpkin / Rick.Lumpkin@noaa.gov

In final form XX XXXXXX XXXX

STATE OF THE CLIMATE IN 2019

Global Oceans

Editors

Jessica Blunden
Derek S. Arndt

Chapter Editors

Peter Bissolli
Howard J. Diamond
Matthew L. Druckenmiller
Robert J. H. Dunn
Catherine Ganter
Nadine Gobron
Rick Lumpkin
Jacqueline A. Richter-Menge
Tim Li
Ademe Mekonnen
Ahira Sànchez-Lugo
Ted A. Scambos
Carl J. Schreck III
Sharon Stammerjohn
Diane M. Stanitski
Kate M. Willett

Technical Editor

Andrea Andersen

BAMS Special Editor for Climate

Richard Rosen

American Meteorological Society

Cover credit:
2019 PIRATA Northeast Extension cruise on the NOAA ship Ronald H. Brown
Photo courtesy Dr. Renellys Perez (NOAA/AOML)

Global Oceans is one chapter from the State of the Climate in 2019 annual report. Compiled by NOAA's National Centers for Environmental Information, State of the Climate in 2019 is based on contributions from scientists from around the world. It provides a detailed update on global climate indicators, notable weather events, and other data collected by environmental monitoring stations and instruments located on land, water, ice, and in space. The full report is available from https://doi.org...."

How to cite this document:

Citing the complete report:
Blunden, J. and D. S. Arndt, Eds., 2020: State of the Climate in 2019. *Bull. Amer. Meteor. Soc.*, **101** (7), Si–S###, doi:10.1175/2020BAMSStateoftheClimate.1.

Citing this chapter:
Lumpkin, R. L., Ed., 2020: Global Oceans [in "State of the Climate in 2019"]. *Bull. Amer. Meteor. Soc.*, **101** (7), S##–S###, doi:10.1175/2020BAMSStateoftheClimate.1.

Citing a section (example):
Franz, B. A., I. Cetinić, J. P. Scott, D. A. Siegel, and T. K. Westberry, 2020: Global ocean phytoplankton [in "State of the Climate in 2019"]. *Bull. Amer. Meteor. Soc.*, **101** (7), S##–S###, doi:10.1175/2020BAMSStateoftheClimate.1.

Editor and Author Affiliations (alphabetical by name)

Baringer, Molly, NOAA/OAR Atlantic Oceanographic and Meteorological Laboratory, Miami, Florida
Bif, Mariana B., Monterey Bay Aquarium Research Institute, Moss Landing, California
Boyer, Tim, NOAA/NESDIS National Centers for Environmental Information, Silver Spring, Maryland
Bushinsky, Seth M., University of Hawai'i at Mānoa, Honolulu, Hawai'i
Carter, Brendan R., Joint Institute for the Study of the Atmosphere and Ocean, University of Washington, and NOAA/OAR Pacific Marine Environmental Laboratory, Seattle, Washington
Cetinić, Ivona, NASA Goddard Space Flight Center, Greenbelt, Maryland, and Universities Space Research Association, Columbia, Maryland
Chambers, Don P., College of Marine Science, University of South Florida, St. Petersburg, Florida
Cheng, Lijing, International Center for Climate and Environment Sciences, Institute of Atmospheric Physics, Chinese Academy of Sciences, Beijing, China
Chiba, Sanai, Japan Agency for Marine-Earth Science and Technology, Yokosuka, Japan
Dai, Minhan, Xiamen University, Xiamen, China
Domingues, Catia M., Institute for Marine and Antarctic Studies, University of Tasmania, Antarctic Climate and Ecosystems Cooperative Research Centre, and Australian Research Council's Centre of Excellence for Climate System Science, Hobart, Tasmania, Australia
Dong, Shenfu, NOAA/OAR Atlantic Oceanographic and Meteorological Laboratory, Miami, Florida
Fassbender, Andrea J., Monterey Bay Aquarium Research Institute, Moss Landing, California
Feely, Richard A., NOAA/OAR Pacific Marine Environmental Laboratory, Seattle, Washington
Frajka-Williams, Eleanor, National Oceanography Centre, Southampton, United Kingdom
Franz, Bryan A., NASA Goddard Space Flight Center, Greenbelt, Maryland
Gilson, John, Scripps Institution of Oceanography, University of California at San Diego, La Jolla, California
Goni, Gustavo, NOAA/OAR Atlantic Oceanographic and Meteorological Laboratory, Miami, Florida
Hamlington, Benjamin D., NASA Jet Propulsion Laboratory, Pasadena, California
Hu, Zeng-Zhen, NOAA/NCEP Climate Prediction Center, College Park, Maryland
Huang, Boyin, NOAA/NESDIS National Centers for Environmental Information, Asheville, North Carolina
Ishii, Masayoshi, Department of Atmosphere, Ocean and Earth System Modeling Research, Meteorological Research Institute, Japan Meteorological Agency, Tsukuba, Japan
Jevrejeva, Svetlana, National Oceanography Centre, Liverpool, United Kingdom
Johns, William E., Rosenstiel School of Marine and Atmospheric Science, University of Miami, Miami, Florida
Johnson, Gregory C., NOAA/OAR Pacific Marine Environmental Laboratory, Seattle, Washington
Johnson, Kenneth S., Monterey Bay Aquarium Research Institute, Moss Landing, California
Kennedy, John, Met Office Hadley Centre, Exeter, United Kingdom
Kersalé, Marion, Cooperative Institute for Marine and Atmospheric Studies, University of Miami, Miami, Florida and NOAA/OAR Atlantic Oceanographic and Meteorological Laboratory (AOML), Miami, Florida
Killick, Rachel E., Met Office Hadley Centre, Exeter, United Kingdom
Landschützer, Peter, Max Planck Institute for Meteorology, Hamburg, Germany
Lankhorst, Matthias, Scripps Institution of Oceanography, University of California at San Diego, La Jolla, California
Lee, Tong, NASA Jet Propulsion Laboratory, Pasadena, California
Leuliette, Eric, NOAA/NESDIS Center for Satellite Applications and Research, College Park, Maryland
Li, Feili, College of Sciences, Georgia Institute of Technology, Atlanta, Georgia
Lindstrom, Eric, Saildrone Inc., Alameda, California
Locarnini, Ricardo, NOAA/NESDIS National Centers for Environmental Information, Silver Spring, Maryland
Lozier, Susan, College of Sciences, Georgia Institute of Technology, Atlanta, Georgia
Lumpkin, Rick, NOAA/OAR Atlantic Oceanographic and Meteorological Laboratory, Miami, Florida
Lyman, John M., NOAA/OAR Pacific Marine Environmental Laboratory, Seattle, Washington, and Joint Institute for Marine and Atmospheric Research, University of Hawaii, Honolulu, Hawai'i
Marra, John J., NOAA/NESDIS National Centers for Environmental Information, Honolulu, Hawai'i
Meinen, Christopher S., NOAA/OAR Atlantic Oceanographic and Meteorological Laboratory, Miami, Florida
Merrifield, Mark A., Scripps Institution of Oceanography, University of California at San Diego, La Jolla, California
Mitchum, Gary T., College of Marine Science, University of South Florida, St. Petersburg, Florida
Moat, Ben, National Oceanography Centre, Southampton, United Kingdom
Monselesan, Didier, CSIRO Oceans and Atmosphere, Hobart, Tasmania, Australia
Nerem, R. Steven, Colorado Center for Astrodynamics Research, Cooperative Institute for Research in Environmental Sciences, University of Colorado Boulder, Boulder, Colorado
Perez, Renellys C., NOAA/OAR Atlantic Oceanographic and Meteorological Laboratory, Miami, Florida
Purkey, Sarah G., Scripps Institution of Oceanography, University of California at San Diego, La Jolla, California
Rayner, Darren, National Oceanography Centre, Southampton, United Kingdom
Reagan, James, Earth System Science Interdisciplinary Center/Cooperative Institute for Climate and Satellites, University of Maryland, College Park, Maryland and NOAA/NESDIS National Centers for Environmental Information, Silver Spring, Maryland
Rome, Nicholas, Consortium for Ocean Leadership, Washington, D.C.
Sanchez-Franks, Alejandra, National Oceanography Centre, Southampton, United Kingdom
Schmid, Claudia, NOAA/OAR Atlantic Oceanographic and Meteorological Laboratory, Miami, Florida
Scott, Joel P., NASA Goddard Space Flight Center, Greenbelt, Maryland and Science Application International Corporation, Beltsville, Maryland
Send, Uwe, Scripps Institution of Oceanography, University of California at San Diego, La Jolla, California
Siegel, David A., University of California at Santa Barbara, Santa Barbara, California
Smeed, David A., National Oceanography Centre, Southampton, United Kingdom
Speich, Sabrina, École Normale Supérieure Laboratoire de Météorologie Dynamique, Paris, France
Stackhouse Jr., Paul W., NASA Langley Research Center, Hampton, Virginia
Sweet, William, NOAA/NOS Center for Operational Oceanographic Products and Services, Silver Spring, Maryland
Takeshita, Yuichiro, Monterey Bay Aquarium Research Institute, Moss Landing, California

Thompson, Philip R., Department of Oceanography, University of Hawai'i at Mānoa, Honolulu, Hawai'i
Triñanes, Joaquin A., Laboratory of Systems, Technological Research Institute, Universidad de Santiago de Compostela, Campus Universitario Sur, Santiago de Compostela, Spain; NOAA/OAR Atlantic Oceanographic and Meteorological Laboratory, Miami, Florida, and Cooperative Institute for Marine and Atmospheric Studies, University of Miami, Miami, Florida
Visbeck, Martin, GEOMAR Helmholtz Centre for Ocean Research Kiel, Kiel, Germany
Volkov, Denis L., Cooperative Institute for Marine and Atmospheric Studies, University of Miami, Miami, Florida and NOAA/OAR Atlantic Oceanographic and Meteorological Laboratory (AOML), Miami, Florida
Wanninkhof, Rik, NOAA/OAR Atlantic Oceanographic and Meteorological Laboratory, Miami, Florida
Weller, Robert A., Woods Hole Oceanographic Institution, Woods Hole, Massachusetts
Westberry, Toby K., Oregon State University, Corvallis, Oregon
Widlansky, Matthew J., Joint Institute for Marine and Atmospheric Research, University of Hawai'i at Mānoa, Honolulu, Hawai'i
Wijffels, Susan E., Woods Hole Oceanographic Institution, Woods Hole, Massachusetts
Wilber, Anne C., Science Systems and Applications, Inc., Hampton, Virginia
Yu, Lisan, Woods Hole Oceanographic Institution, Woods Hole, Massachusetts
Yu, Weidong, National Marine Environmental Forecasting Center, State Oceanic Administration, Beijing, China
Zhang, Huai-Min, NOAA/NESDIS National Centers for Environmental Information, Asheville, North Carolina

Editorial and Production Team

Andersen, Andrea, Technical Editor, TeleSolv Consulting LLC, NOAA/NESDIS National Centers for Environmental Information, Asheville, North Carolina
Griffin, Jessicca, Graphics Support, Cooperative Institute for Satellite Earth System Studies, North Carolina State University, Asheville, North Carolina
Hammer, Gregory, Content Team Lead, Communications and Outreach, NOAA/NESDIS National Centers for Environmental Information, Asheville, North Carolina
Love-Brotak, S. Elizabeth, Lead Graphics Production, NOAA/NESDIS National Centers for Environmental Information, Asheville, North Carolina
Misch, Deborah J., Graphics Support, Innovative Consulting & Management Services, LLC, NOAA/NESDIS National Centers for Environmental Information, Asheville, North Carolina
Riddle, Deborah B., Graphics Support, NOAA/NESDIS National Centers for Environmental Information, Asheville, North Carolina
Veasey, Sara W., Visual Communications Team Lead, Communications and Outreach, NOAA/NESDIS National Centers for Environmental Information, Asheville, North Carolina

3. Table of Contents

3. GLOBAL OCEANS

Rick Lumpkin, Ed.

a. Overview—R. Lumpkin

In this chapter, we examine the state of the global oceans in 2019, focusing both on changes from 2018 to 2019 and on the longer-term perspective. Sidebars focus on the significance and ongoing scientific results from the growing array of Argo floats measuring biogeochemical properties, and on the OceanObs'19 conference, a once-per-decade event focusing on sustaining and enhancing the global ocean-observing system.

The year 2019 marks the eighth consecutive year that global mean sea level increased relative to the previous year, reaching a new record: 87.6 mm above the 1993 average (Fig. 3.14a) and peaking in the middle of the year. The globally averaged 2019 sea surface temperature anomaly (SSTA) was the second highest on record, surpassed only by the record El Niño year of 2016. The warming trend of ocean heat content (OHC) from 2004 to 2019 corresponds to 0.18°–0.20°C decade^{-1} near the surface, declining to <0.03°C decade^{-1} below 300 m (Fig. 3.5). Over the period 1993–2019, 2019 was a record high for OHC from 0–700 m depth (Fig. 3.6a) and from 700–2000 m depth (Fig. 3.6b), consistent with heat gain of approximately 0.4 W m^{-2} applied over the surface of Earth from 1993 to 2019 (Table 3.2). The year also set a new record for net ocean uptake of CO_2 for the period 1982–present, ~2.4 Pg C (Fig. 3.26), an increase of 0.2 Pg C from 2018. This continues a trend that started in 2000–02. As a consequence of the increased oceanic CO_2, surface ocean pH has declined by 0.018 ± 0.004 units decade^{-1} in most of the ocean since the pre-industrial period, particularly in colder water (Fig. 3.28b).

The Indian Ocean dipole (IOD), defined as the difference between western and eastern Indian Ocean basin SSTAs, reached its highest level since 1997 in October 2019, associated with dramatic upper ocean warming in the western Indian Ocean basin (Figs. 3.1a, 3.4a). This SSTA pattern resulted in a significant weakening of the trade winds (Fig. 3.12a), more precipitation in the west, and drier conditions in the east in 2019 (Fig. 3.11), and thus anomalously salty surface waters in the east and fresh in the west (Figs. 3.7a,b). Indian Ocean net heat gain anomalies for 2019 reached maxima of >30 W m^{-2} and were much larger than climatology in most of the central and eastern tropical Indian Ocean basin (Fig. 3.10a). This heat gain was associated with increased surface radiation (Fig. 3.10c) and drove increased turbulent heat loss to the atmosphere (Fig. 3.10d). In the lead-up to the extreme dipole event, westward geostrophic current anomalies developed across the basin, reaching maxima of ~40 cm s^{-1} at the peak of the dipole (Fig. 3.18). By the end of the year, there was a significant east-to-west sea level anomaly gradient across the tropical Indian Ocean (Fig. 3.15d).

The tropical Pacific was characterized by a transition from a diminishing La Niña in 2018 to the development of a weak El Niño by early 2019. Sustained negative values of the Oceanic Niño Index over the last decade produced positive anomalies in the flux of CO_2 from the ocean to the atmosphere in the eastern tropical Pacific (Fig. 3.27c). In the North Pacific, sea surface temperatures (SSTs) increased significantly in the latter half of 2019 (Figs. 3.2c,d), leading to the reemergence of a "warm blob" that was associated with a decrease in precipitation (Fig. 3.11d) and winds (Fig. 3.12a). In the northwest subpolar Pacific and western Bering Sea, positive anomalies in the flux of CO_2 from the ocean to the atmosphere were related to sustained above-average SSTA there (Fig. 3.27c).

Positive SSTAs were observed in the tropical Atlantic, corresponding to the development of an Atlantic Niño. The North Atlantic was characterized by a tripole-like SSTA pattern (Fig. 3.1a), associated with positive net heat flux anomalies from 30°S to 60°N (Figs. 3.10a,b). Dramatic SST increase in the Labrador Sea (Fig. 3.1a) was associated with the reduction of sea ice coverage. Upper ocean heat content south of Greenland, which had been anomalously low since 2009, increased in 2019 (Fig. 3.4a).

The October 2018–September 2019 globally-averaged concentration of chlorophyll-*a* (chl*a*) varied from its 22-year monthly climatology by ±6% (Fig. 3.25b), while the concentration of phytoplanktonic carbon (C_{phy}) varied by ±2% (Fig. 3.25d), indicating neutral El Niño–Southern Oscillation conditions. Regionally, chl*a* was suppressed by 10%–30% where SST anomalies were positive, while variations of C_{phy} were far less dramatic. This is because above-average SST anomalies are associated with shallow mixed layers and thus increased light exposure to phytoplankton in that layer, leading in turn to reduced cellular chl*a* and a decoupling of chl*a* and C_{phy} concentrations.

For this year's report, we are pleased to re-introduce a section focusing on the Atlantic meridional overturning circulation (AMOC). In this section, we learn that decadal-scale variability of the southward deep western boundary current in the subtropical North Atlantic is poorly correlated with the relatively constant (at these time scales) northward-flowing Florida Current, and that rapid changes in the Florida Current can be driven by hurricanes; the passage of Hurricane Dorian coincided with the lowest transport measurement of the current ever recorded. The strength of the AMOC in the subtropical North Atlantic significantly decreased between 2004–08 and 2008–12 (Smeed et al. 2018) and has remained lower since then (Moat et al. 2019, 2020), consistent with a reduction of deep water production farther north. Direct measurements in the subpolar North Atlantic, collected by the Overturning in the Subpolar North Atlantic Program (OSNAP) array, challenge the conventional wisdom that deep water formation changes are strongly associated with changes in convection in the Labrador Sea, instead pointing to changes solely in the Irminger and Iceland basins (Lozier et al. 2019). In the South Atlantic, interannual variations in the AMOC strength are associated with both density-driven and pressure-driven fluctuations (Meinen et al. 2018).

b. Sea surface temperature—B. Huang, Z.-Z. Hu, J. J. Kennedy, and H.-M. Zhang

The sea surface temperature (SST) over the global ocean (all water surfaces, including seas and great lakes) in 2019 is assessed using three updated products of SST and its uncertainty. These products are the Extended Reconstruction Sea-Surface Temperature version 5 (ERSSTv5; Huang et al. 2017, 2020), Daily Optimum Interpolation SST version 2 (DOISST; Reynolds et al. 2007), and U.K. Met Office Hadley Centre SST (HadSST.3.1.1.0 and HadSST.4.0.0.0; Kennedy et al. 2011a, b, 2019). See the *State of the Climate in 2018* report for details of these calculations. SST anomalies (SSTAs) are calculated relative to their own climatologies over 1981–2010. The magnitudes of SSTAs are compared against SST standard deviations (std. dev.) over 1981–2010.

Averaged over the global oceans, ERSSTv5 analysis shows that SSTAs increased significantly from 0.33° ± 0.03°C in 2018 to 0.41° ± 0.03°C in 2019. The uncertainty in ERSSTv5 is slightly smaller than that in ERSSTv4, as determined by a Student's t-test using a 1000-member ensemble based on ERSSTv5 with randomly drawn parameter values within reasonable ranges in the SST reconstructions (Huang et al. 2015, 2020).

Figure 3.1a shows annually averaged SSTA in 2019. In most of the North Pacific, SSTAs were between +0.5°C and +1.0°C except for near the Bering Strait (+1.5°C), about +0.5°C in the western South Pacific, and between −0.2°C and +0.2°C in the eastern South Pacific. The extreme warm event in the northeast Pacific is referred to as Blob 2.0 (Amaya et al. 2020). In the Atlantic, SSTAs were between +0.2°C and +0.5°C except for the tropical North Atlantic and near the coast of Africa (−0.2°C to 0°C), central North Atlantic near 45°N and 30°W (0°C), and the Labrador Sea (about +1.5°C). In the Indian Ocean, SSTAs were +0.5°C west of 90°E and slightly below average

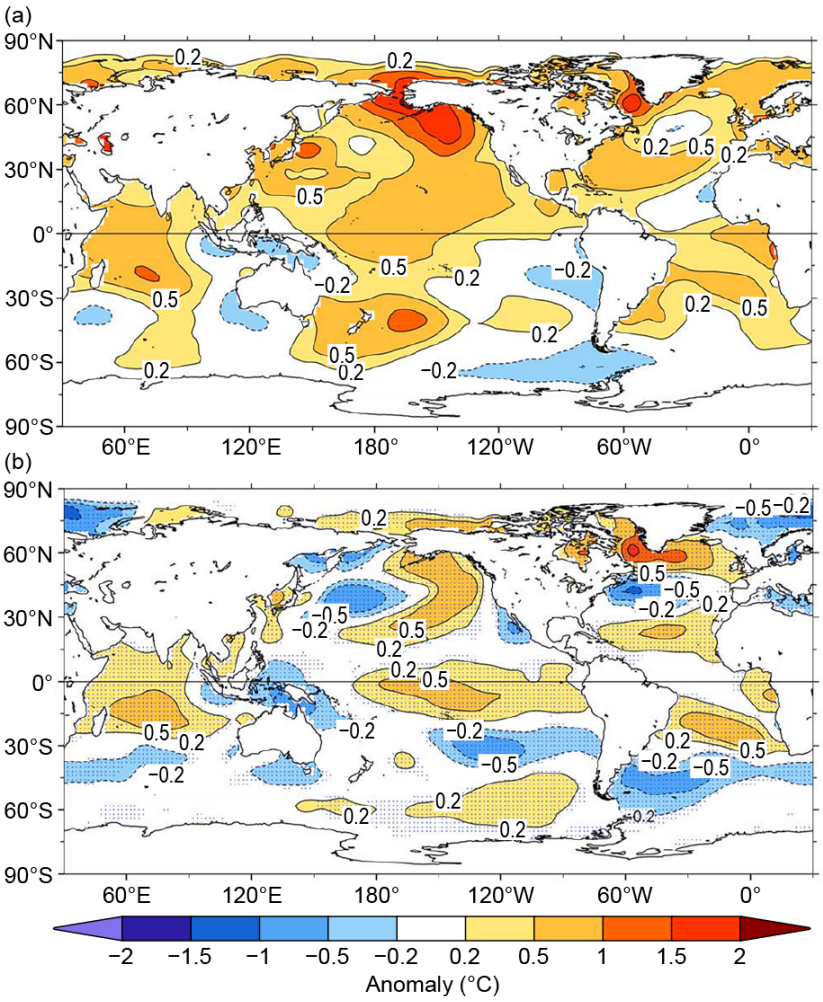

Fig. 3.1. (a) Annually averaged SSTAs (°C) in 2019 and (b) difference of annually averaged SSTAs between 2019 and 2018. SSTAs are relative to 1981–2010 climatology. The SST difference in (b) is significant at 95% level in stippled areas.

(−0.2°C) in the regions surrounding the Maritime Continent and western Australia.

In comparison with averaged SST in 2018, the averaged SST in 2019 increased by +1.0°C to +1.5°C south of Greenland (Fig. 3.1b) and was +0.2°C to +0.5°C higher in the northeastern Pacific stretching from Alaska and Canada toward the central North Pacific, in the central-eastern tropical Pacific, in the Pacific sector of the Southern Ocean south of 50°S, in the tropical North Atlantic over 10°–30°N, in the tropical South Atlantic over 10°–30°S, in the eastern equatorial Atlantic, and in most of the Indian Ocean. In contrast, the SST decreased by −0.2°C to −0.5°C in the North Atlantic poleward of 60°N, in the subtropical North Atlantic between 30°N and 45°N, in the subpolar South Atlantic south of 35°S, in the northwestern North Pacific between 30°N and 65°N, in the western tropical Pacific, in the subtropical South Pacific between 20°S and 40°S, and in the southern Indian Ocean between 30°S and 45°S. These SST changes are statistically significant at the 95% confidence level based on an ensemble analysis of 1000 members.

The pattern of cooling in the western North Pacific and warming in the eastern North Pacific (Fig. 3.1b) may be associated with a shift of the Pacific Decadal Oscillation (PDO; Mantua and Hare 2002) index from a negative phase in 2018 to near neutral in 2019. The warming in the central-eastern tropical Pacific (Fig. 3.1b) is associated with a transition from the weak La Niña over 2017/18 to the weak El Niño over 2018/19. The warming in the western Indian Ocean is associated with an enhanced Indian Ocean dipole (IOD; Saji et al. 1999; see section 4h) from 0.3°C in 2018 to 0.8°C in 2019. The monthly IOD index reached a its highest level since 1997 in October 2019 that affected patterns of precipitation and precipitation-minus-evaporation over the Maritime Continent and Australia (Fig. 3.11, see section 7h4).

The seasonal variations in SST in 2019 were profound. In most of the North Pacific, SSTAs were +0.2°C to +0.5°C (1 std. dev. above average) in December–February (DJF) and March–May (MAM) (Figs. 3.2a,b). The anomaly increase ranged from +0.5°C to +2.0°C (2 std. dev.) in June–August (JJA) and September–November (SON; Figs. 3.2c,d). In contrast, in the western South Pacific, SSTAs were high (+1.0°C; ≥2 std. dev.) in DJF, MAM, and JJA and lower in SON, albeit still above average (+0.5°C; ≥1 std. dev.). In the eastern South Pacific, SSTAs persisted at about −0.2°C, although these anomalies stretched farther westward and equatorward in JJA and SON (Figs. 3.2c,d) than in DJF and MAM (Figs. 3.2a,b) following the evolution of the equatorial Pacific cold tongue. In the

Southern Ocean between the date line and 30°W, SSTAs were −0.5°C to −1.5°C (1 std. dev. below average) in DJF and MAM but were closer to average in JJA and SON.

It should be noted that there was an unusual heat content anomaly during the summer and spring around New Zealand (Figs. 3.2a,b). The Tasman Sea has seen a series of marine heatwaves in the past few years (Oliver et al. 2017; Perkins-Kirkpatrick et al. 2019; Babcock et al. 2019). In December 2019, SSTAs to the east of New Zealand were significantly above average.

In the western Indian Ocean, SSTAs persisted in the range of +0.5°C to +1.0°C (1–2 std. dev. above average) throughout all seasons (Fig. 3.2), while SSTAs were from −0.5°C to −1.0°C (1–2 std. dev. below average) in the eastern Indian Ocean and regions of the Maritime Continent. The warm western Indian Ocean and the cold southeastern Indian Ocean resulted in an extremely strong positive phase of the IOD event and the highest IOD index value since 1997.

Along the coasts of the Arctic, SSTs were near average in DJF and MAM (Figs. 3.2a,b) but above average (+1.0°C to +2.0°C; ≥2 std. dev.) in JJA and SON (Figs. 3.2c,d), which may be directly associated with the reduction of sea ice concentration. Similarly, south of Greenland, SSTs were near average in DJF and MAM but significantly above average in JJA and SON (+1.0°C to +2.0°C; ≥2 std. dev.), associated with the reduction of sea ice concentration in these areas. In the Labrador Sea, SSTAs were high in JJA and SON but lower in DJF and MAM.

In the northern North Atlantic between 60°N and 80°N, above-average SSTs persisted throughout all seasons (+0.5°C to 1.0°C; 1 to 2 std. dev.). In the North Atlantic between 30°N and 60°N, SSTAs were negative (−0.5°C) in DJF, MAM, and JJA (Figs. 3.2a,b,c) but closer to average in SON (Fig. 3.2d). In the tropical North Atlantic, SSTAs were slightly below average (−0.5°C) throughout all seasons. In the equatorial Atlantic, SSTAs were +0.5°C above average in DJF and MAM, weakening in JJA, and strengthening again in SON, associated with the emergence of a weak Atlantic Niño that usually peaks in JJA (Chang et al. 2006). In the subtropical South Atlantic, SSTAs were

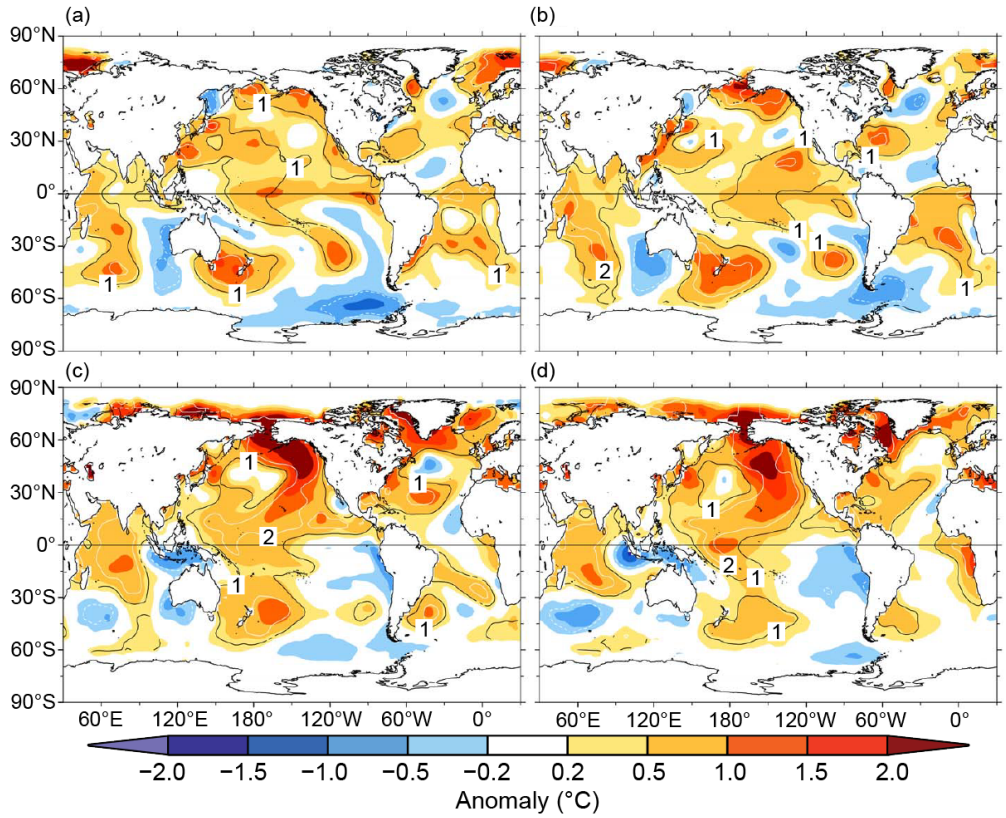

Fig. 3.2. Seasonally averaged SSTAs of ERSSTv5 (°C; shading) for (a) Dec–Feb 2018/19, (b) Mar–May 2019, (c) Jun–Aug 2019, and (d) Sep–Nov 2019. The normalized seasonal mean SSTA based on seasonal mean 1 std. dev. over 1981–2010, indicated by contours of –1 (dashed white), 1 (solid black), and 2 (solid white).

+0.5°C to +1.0°C (1 to 2 std. dev.) in DJF and MAM, and the area of warm SSTAs was reduced in JJA and further diminished in SON.

Overall, the global ocean warming trends of SSTs since the 1950s remained significant (Figs. 3.3a,b; Table 3.1), with noticeably higher SSTAs in 2019 (+0.41°C) than in 2018 (+0.33°C). The year 2019 was the second-warmest year since 1950 after the record year of 2016 (+0.44°C). The linear trends of globally annually averaged SSTAs were 0.10° ± 0.01°C decade^{-1} over 1950–2019 (Table 3.1). The warming appeared largest in the tropical Indian Ocean (Fig. 3.3e; 0.14° ± 0.02°C decade^{-1}) and smallest in the North Pacific (Fig. 3.3d; 0.09° ± 0.03°C decade^{-1}). The uncertainty of the trends represents the 95% confidence level of the linear fitting uncertainty and 1000-member data uncertainty.

Table 3.1. Linear trends (°C decade^{-1}) of annually and regionally averaged SSTAs from ERSSTv5, HadSST3, and DOISST. The uncertainties at 95% confidence level are estimated by accounting for the effective sampling number quantified by lag-1 auto correlation on the degrees of freedom of annually-averaged SST series.

Product	Region	2000–2019 (°C decade^{-1})	1905–2019 (°C decade^{-1})
HadSST.3.1.1.0	Global	0.140 ± 0.065	0.086 ± 0.016
DOISST	Global	0.156 ± 0.058	N/A
ERSSTv5	Global	0.170 ± 0.075	0.101 ± 0.013
ERSSTv5	Tropical Pacific (30°N–30°S)	0.188 ± 0.185	0.102 ± 0.028
ERSSTv5	North Pacific (30°–60°N)	0.287 ± 0.172	0.087 ± 0.028
ERSSTv5	Tropical Indian Ocean (30°N–30°S)	0.199 ± 0.098	0.141 ± 0.018
ERSSTv5	North Atlantic (30°–60°N)	0.142 ± 0.087	0.101 ± 0.034
ERSSTv5	Tropical Atlantic (30°N–30°S)	0.133 ± 0.097	0.109 ± 0.020
ERSSTv5	Southern Ocean (30°–60°S)	0.129 ± 0.060	0.099 ± 0.016

In addition to the long-term SST trend and interannual variability, interdecadal variations of SSTAs can be seen in all ocean basins, although the amplitude of the variations was smaller in the Southern Ocean (Fig. 3.3h). The variations associated with the Atlantic Multidecadal Variability (Schlesinger and Ramankutty 1994) can be identified in the North Atlantic with warm periods in the 1950s and over the 1990s–2010s, and a cold period over the 1960s–80s (Fig. 3.3f). Similarly, SSTAs in the North Pacific (Fig. 3.3d) decreased from the 1950s to the late 1980s, followed by an increase from the later 1980s to the 2010s.

SSTAs in ERSSTv5 were compared with those in DOISST, HadSST3.1.1.0, and HadSST.4.0.0.0. All data sets were averaged to an annual 2° × 2° grid for comparison purposes. Comparisons (Fig. 3.3) indicate that the SSTA departures of DOISST and HadSST.3.1.1.0 from ERSSTv5 are largely within 2 std. dev. (gray shading in Fig. 3.3). The 2 std. dev. was derived from a 1000-member ensemble analysis based on ERSSTv5 (Huang et al. 2020) and centered to SSTAs of ERSSTv5. Overall, the HadSST4.0.0.0 is more consistent with ERSSTv5 than HadSST.3.1.1.0. In the 2000s–10s, SSTAs in the Southern Ocean were slightly higher in DOISST than in ERSSTv5. Previous studies (Huang et al. 2015; Kent et al. 2017) have indicated that these SSTA differences are mostly attributed to the differences in bias corrections to ship observations in those products. These SST differences resulted in a slightly weaker SSTA trend in HadSST.3.1.1.0 over both 1950–2019 and 2000–19 (Table 3.1). In contrast, SST trends were slightly higher in DOISST over 2000–19.

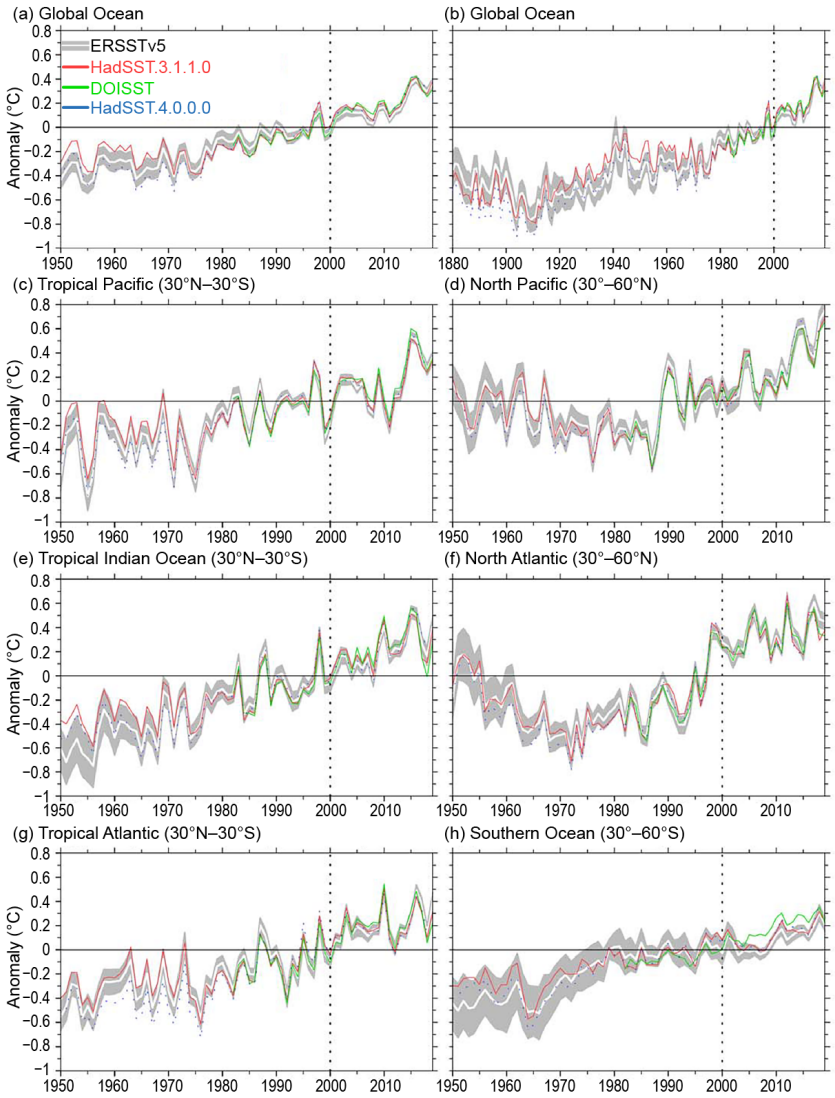

Fig. 3.3. Annually averaged SSTAs (°C) of ERSSTv5 (solid white) and 2 std. dev. (gray shading) of ERSSTv5, SSTAs of DOISST (solid green), and SSTAs of HadSST.3.1.1.0 (solid red) and HadSST.4.0.0.0 (dotted blue) in 1950–2019 except for (b). (a) Global, (b) global in 1880–2019, (c) tropical Pacific Ocean, (d) North Pacific Ocean, (e) tropical Indian Ocean, (f) North Atlantic Ocean, (g) tropical Atlantic Ocean, and (h) Southern Ocean. The year 2000 is indicated by a vertical black dotted line.

c. Ocean heat content—G. C. Johnson, J. M. Lyman, T. Boyer, L. Cheng, C. M. Domingues, J. Gilson, M. Ishii, R. E. Killick, D. Monselesan, S. G. Purkey, and S. E. Wijffels

One degree of warming in the global ocean stores more than 1000 times the heat energy of one degree of warming in the atmosphere owing to the higher mass of the ocean (280 times that of the atmosphere) and the larger heat capacity of water (four times that of air). Ocean warming accounts for about 89% of the total increase in Earth's energy storage from 1960 to 2018, compared to the atmosphere's 1%. Ocean currents also transport substantial amounts of heat (Talley 2003). Ocean heat storage and transport play large roles in the El Niño–Southern Oscillation (ENSO; Johnson and Birnbaum 2017), tropical cyclone activity (Goni et al. 2009), sea level variability and rates of change (section 3f), and melting of ice sheet outlet glaciers around Greenland (Castro de la Guardia et al. 2015) and Antarctica (Schmidtko et al. 2014).

Maps of annual (Fig. 3.4) upper (0–700 m) ocean heat content anomaly (OHCA) relative to a 1993–2019 baseline mean are generated from a combination of in situ ocean temperature data and satellite altimetry data following Willis et al. (2004), but using Argo (Riser et al. 2016) data downloaded in January 2020. Near-global average seasonal temperature anomalies (Fig. 3.5) versus

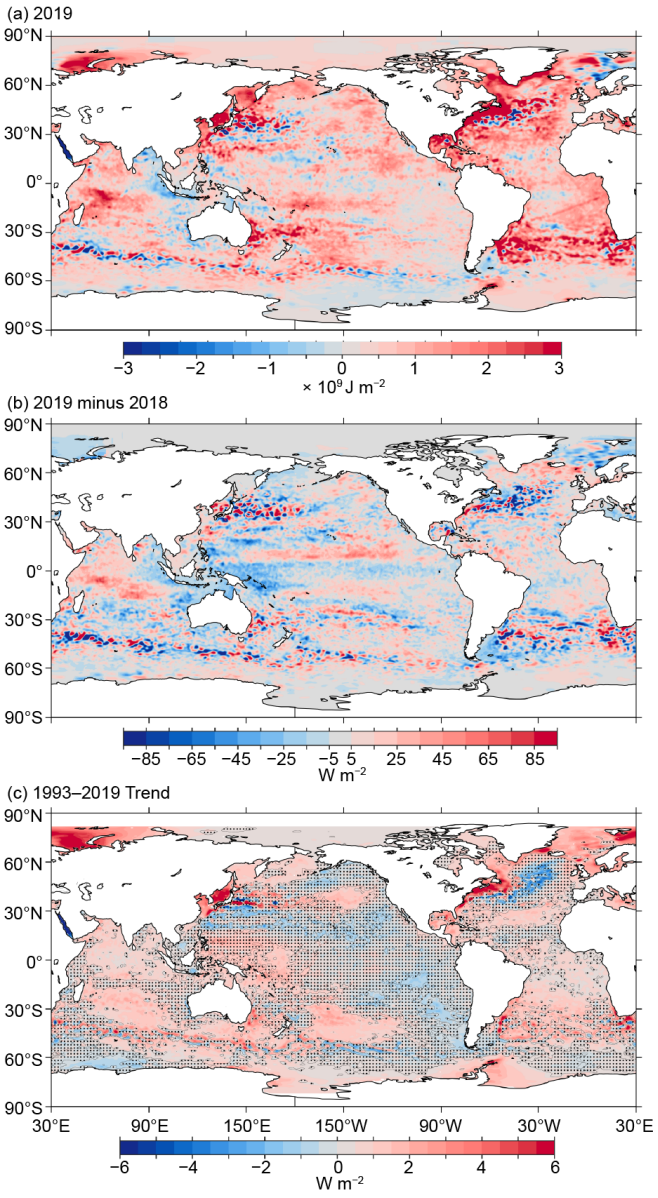

Fig. 3.4. (a) Combined satellite altimeter and in situ ocean temperature data estimate of upper (0–700 m) OHCA (× 10^9 J m^{-2}) for 2019 analyzed following Willis et al. (2004), but using an Argo monthly climatology and displayed relative to the 1993–2019 baseline. (b) 2019 minus 2018 combined estimates of OHCA expressed as a local surface heat flux equivalent (W m^{-2}). For (a) and (b) comparisons, note that 95 W m^{-2} applied over one year results in a 3 × 10^9 J m^{-2} change of OHCA. (c) Linear trend from 1993–2019 of the combined estimates of upper (0–700 m) annual OHCA (W m^{-2}). Areas with statistically insignificant trends are stippled.

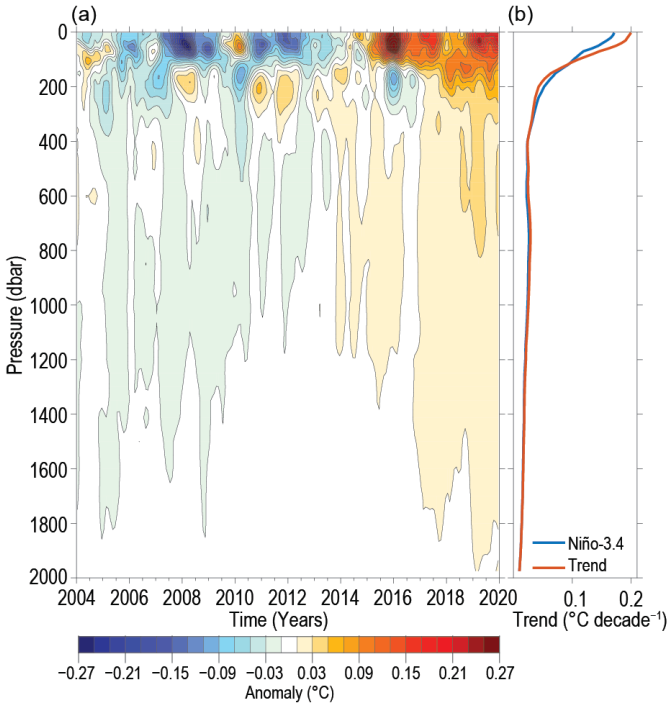

Fig. 3.5. (a) Near-global (80°N–65°S, excluding continental shelves, the Indonesian seas, and the Sea of Okhostk) integrals of monthly ocean temperature anomalies (°C; updated from Roemmich and Gilson 2009) relative to record-length average monthly values, smoothed with a 5-month Hanning filter and contoured at odd 0.02°C intervals (see color bar) versus pressure and time. (b) Linear trend of temperature anomalies over time for the length of the record in (a) plotted versus pressure in °C $decade^{-1}$ (orange line), and trend with a Niño3.4 regression removed (blue line) following Johnson and Birnbaum (2017).

pressure from Argo data (Roemmich and Gilson 2009, updated) since 2004 and in situ global estimates of OHCA (Fig. 3.6) for three pressure layers (0–700 m, 700–2000 m, and 2000–6000 m) from seven different research groups are also discussed.

The 2018/19 tendency of 0–700 m OHCA (Fig. 3.4b) in the Pacific shows a decrease along the equator, with a near-zonal band of increase just to the north, consistent with the discharge of heat from the equatorial region after the weak El Niño of 2018/19 and a decrease in eastward surface current anomalies north of the equator from 2018 to 2019 (see Fig. 3.17b). Outside of the equatorial region in the Pacific, there are nearly zonal bands of increases and decreases that tend to tilt equatorward to the west. Structures like these are quite common in the OHCA tendency maps from previous years and are reminiscent of Rossby wave dynamics. There are also, as usual, small-scale increases and decreases at eddy scales especially visible in and poleward of the subtropical gyres. Throughout much of the Pacific, the 2019 upper OHCA is generally above the long-term average (Fig. 3.4a), with the most notable departures being patches of below-average values southwest and south of Hawaii and low values in the Southern Ocean from Drake Passage to about 150°W.

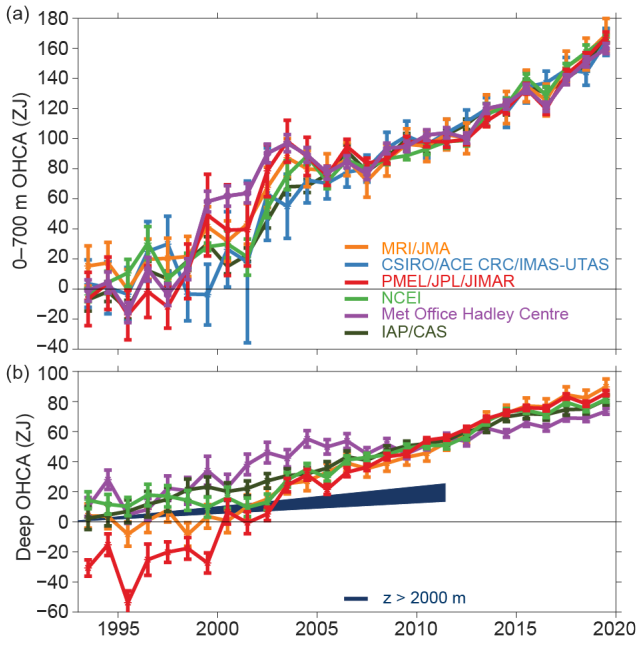

Fig. 3.6. (a) Annual average global integrals of in situ estimates of upper (0–700 m) OHCA (ZJ; 1 ZJ = 10^{21} J) for 1993–2019 with standard errors of the mean. The MRI/JMA estimate is an update of Ishii et al. (2017). The CSIRO/ACE CRC/IMAS-UTAS estimate is an update of Domingues et al. (2008). The PMEL/JPL/JIMAR estimate is an update and refinement of Lyman and Johnson (2014). The NCEI estimate follows Levitus et al. (2012). The Met Office Hadley Centre estimate is computed from gridded monthly temperature anomalies (relative to 1950–2019) following Palmer et al. (2007). The IAP/CAS estimate is reported in Cheng et al. (2020). See Johnson et al. (2014) for details on uncertainties, methods, and datasets. For comparison, all estimates have been individually offset (vertically on the plot), first to their individual 2005–19 means (the best-sampled time period), and then to their collective 1993 mean. (b) Annual average global integrals of in situ estimates of intermediate (700–2000 m) OHCA for 1993–2018 with standard errors of the mean, and a long-term trend with one standard error uncertainty shown from 1992.4–2011.5 for deep and abyssal (z > 2000 m) OHCA following Purkey and Johnson (2010) but updated using all repeat hydrographic section data available from https://cchdo.ucsd.edu/ as of January 2020.

In the Indian Ocean, the 2018/19 tendency of 0–700-m OHCA (Fig. 3.4b) shows the strongest increases in a near-zonal band that again tilts equatorward to the west, starting at about 12°S well off the west coast of Australia and ending at about 6°S near Africa. The largest decreases are observed in the eastern portion of the basin, just to the west of Indonesia and Australia, as well as patchy decreases between 35°S and 20°S across the basin and south of Australia. Smaller increases are evident across much of the Arabian Sea and the western portion of the Bay of Bengal. Upper OHCA values for 2019 were above the 1993–2019 mean in much of the Indian Ocean (Fig. 3.4a), with especially high values northeast of Madagascar and below-average values mostly found west of Indonesia and Australia. This pattern is consistent with a positive Indian Ocean dipole (IOD) pattern of SSTs (section 3b), which has been linked to bushfires in Australia and flooding in East Africa (see sections 7h4 and 7e3, respectively). It is also consistent with the increase in westward surface current anomalies along and south of the equator in the Indian Ocean from 2018 to 2019 (see Fig. 3.17b).

The 2018/19 tendencies of 0–700-m OHCA (Fig. 3.4b) in the Atlantic Ocean are generally toward warming in the tropics and subtropics, as well as in the subpolar North Atlantic from northern Europe to northern Canada. Large-scale 2018/19 cooling tendencies are located east of Argentina and east of Canada from Nova Scotia to St. John's, Newfoundland. The only large-scale regions in the Atlantic with below-average heat content in 2019 (Fig. 3.4a) were east of Argentina and north of Norway. In a change from recent years, upper OHCA in 2019 was above the 1993–2019 average south of Greenland, in the vicinity of the Irminger Sea, where a cold area had persisted since around 2009 (see previous *State of the Climate* reports). However, the warm conditions off the east coast of North America that have also persisted since around 2009 intensified further. In 2019, there were no large areas in the North Atlantic that were cooler than average.

The large-scale statistically significant (Fig. 3.4c) regional patterns in the 1993–2019 local linear trends of upper OHCA are quite similar to those from 1993–2018 (Johnson et al. 2019). The limited areas with statistically significant negative trends are found mostly south of Greenland in the North Atlantic, south of the Kuroshio Extension across the North Pacific, in portions of the eastern South Pacific, and in the Red Sea. The much larger areas with statistically significant positive trends include much of the rest of the Atlantic Ocean, the western tropical Pacific, the central North Pacific, most of the Indian Ocean, most of the marginal seas except the Red Sea, and

much of the South Pacific Ocean. The Arctic and portions of the Southern Ocean show warming as well, although those regions have limited in situ data.

Near-global average seasonal temperature anomalies (Fig. 3.5a) from the start of 2004 through the end of 2019 exhibit a clear record-length warming trend (Fig. 3.5b, orange line). In addition, during El Niño events (e.g., 2009/10 and 2014–16) the surface-to-100-dbar is warmer than surrounding years and 100–400 dbar is cooler as the east-west tilt of the equatorial Pacific thermocline flattens out (e.g., Roemmich and Gilson 2011; Johnson and Birnbaum 2017). The opposite pattern holds during La Niña events (e.g., 2007/08 and 2010–12) as the equatorial Pacific thermocline shoals in the east and deepens in the west. The overall warming trend (Fig. 3.5b, orange line) from 2004 to 2019 exceeds 0.2°C decade^{-1} near the surface, declining to less than 0.03°C decade^{-1} below 300 dbar and about 0.01°C decade^{-1} by 2000 dbar. Removing a linear regression against the Niño3.4 index, which is correlated with ocean warming rates (e.g., Johnson and Birnbaum 2017), results in a decadal warming trend (Fig. 3.5b, blue line) that is slightly smaller in the upper 100 dbar, at about 0.18°C decade^{-1} near the surface and slightly larger than the simple linear trend from about 100 dbar to 300 dbar, as expected given the large El Niño near the end of the record. Since the start of 2017, temperatures from the surface to almost 2000 dbar are higher than the 2004–19 average (Fig. 3.5a). While 2018 was slightly warmer than 2019 from 110–225 dbar, 2019 was as warm or warmer than all other years over the full measured depth range.

The analysis is extended back in time from the Argo period to 1993 using sparser, more heterogeneous historical data collected mostly from ships (e.g., Abraham et al. 2013). The six different estimates of annual globally integrated 0–700-m OHCA (Fig. 3.6a) all reveal a large increase since 1993, with all of the analyses reporting 2019 as a record high. The globally integrated 700–2000-m OCHA annual values (Fig. 3.6b) vary more among analyses, but all report 2019 as a record high, and the long-term warming trend in this layer is also clear. Globally integrated OHCA values in both layers vary more both from year to year for individual years and from estimate to estimate in any given year prior to the achievement of a near-global Argo array around 2005. The water column from 0–700 and 700–2000 m gained 14 (±5) and 6 (±1) Zettajoules (ZJ), respectively (means and standard deviations given) from 2018 to 2019. Causes of differences among estimates are discussed in Johnson et al. (2015).

The rate of heat gain from linear fits to each of the six global integral estimates of 0–700 m OHCA from 1993 through 2019 (Fig. 3.6a) ranges from 0.36 (±0.06) to 0.41 (±0.04) W m^{-2} applied over the surface area of Earth (Table 3.2). Linear trends from 700 m to 2000 m over the same time period range from 0.14 (±0.04) to 0.32 (±0.03) W m^{-2}. Trends in the 0–700-m layer all agree within their 5%–95% uncertainties, but as noted in previous reports, the Precision Measurement Equipment Laboratory/Joint Institute of Marine and Atmsopheric Research/Jet Propulsion Laboratory (PMEL/JIMAR/JPL) trend in the 700–2000 m layer, which is quite sparsely sampled prior to the start of the Argo era (circa 2005), does not. Different methods for dealing with under-sampled regions in analyses likely cause this disagreement. For 2000–6000 m, the linear trend is 0.06 (±0.03) W m^{-2}

Table 3.2. Trends of ocean heat content increase (in W m^{-2} applied over the 5.1 × 10^{14} m^2 surface area of Earth) from seven different research groups over three depth ranges (see Fig 3.6 for details). For the 0–700 m and 700–2000 m depth ranges, estimates cover 1993–2019, with 5%–95% uncertainties based on the residuals taking their temporal correlation into account when estimating degrees of freedom (Von Storch and Zwiers 1999). The 2000–6000-m depth range estimate, an update of Purkey and Johnson (2010), uses data from 1981 to 2019, but the globally averaged first and last years are 1992.4 and 2011.5, again with 5%–95% uncertainty

	Global ocean heat content trends (W m^{-2}) for three deep range		
Research Group	0–700 m	700–2000 m	2000–6000 m
MRI/JMA	0.36 ± 0.06	0.24 ± 0.05	—
CSIRO/ACE/CRC/IMAS/UTAS	0.40 ± 0.06	—	—
PMEL/JPL/JIMAR	0.39 ± 0.13	0.32 ± 0.03	—
NCEI	0.39 ± 0.06	0.19 ± 0.06	—
Met Office Hadley Centre	0.37 ± 0.13	0.14 ± 0.04	—
IAP/CAS	0.41 ± 0.04	0.19 ± 0.01	—
Purkey and Johnson	—		0.06 ± 0.03

from June 1992 to July 2011, using repeat hydrographic section data collected from 1981 to 2019 to update the estimate of Purkey and Johnson (2010). Summing the three layers (with their slightly different time periods), the full-depth ocean heat gain rate for the period from approximately 1993 to 2019 ranges from 0.55 to 0.79 W m–2. Estimates starting circa 2005 have much smaller uncertainties (e.g., Johnson et al. 2016).

d. Salinity—G. C. Johnson, J. Reagan, J. M. Lyman, T. Boyer, C. Schmid, and R. Locarnini

1) Introduction—G. C. Johnson and J. Reagan

Salinity, the fraction of dissolved salts in water, and temperature determine the density of seawater at a given pressure. At high latitudes where vertical temperature gradients are small, low near-surface salinity values can be responsible for much of the density stratification. At lower latitudes, fresh near-surface barrier layers can limit the vertical extent of ocean exchange with the atmosphere (e.g., Lukas and Lindstrom 1991). Salinity variability can alter the density patterns that are integral to the global thermohaline circulation (e.g., Gordon 1986; Broecker 1991). One prominent limb of that circulation, the Atlantic meridional overturning circulation (AMOC; section 3h), is particularly susceptible to changes in salinity (e.g., Liu et al. 2017). Salinity is a conservative water property, indicating where a water mass was originally formed at the surface and subducted into the ocean's interior (e.g., Skliris et al. 2014). Where precipitation dominates evaporation, near-surface conditions are fresher (i.e., along the Intertropical Convergence Zone [ITCZ] and at high latitudes), and where evaporation dominates precipitation, they are saltier (i.e., in the subtropics). With ~80% of the global hydrological cycle taking place over the ocean (e.g., Durack 2015), near-surface salinity changes over time can serve as a broad-scale rain gauge (e.g., Terray et al. 2012) used to diagnose hydrological cycle amplifications associated with global warming (e.g., Durack et al. 2012). Finally, besides atmospheric freshwater fluxes, other factors modify salinity, such as advection, mixing, entrainment, sea ice melt/freeze, and river runoff (e.g., Ren et al. 2011).

To investigate interannual changes of subsurface salinity, all available salinity profile data are quality controlled following Boyer et al. (2018) and then used to derive 1° monthly mean gridded salinity anomalies relative to a long-term monthly mean for the period 1955–2012 (World Ocean Atlas 2013 version 2 [WOA13v2]; Zweng et al. 2013) at standard depths from the surface to 2000-m depth (Boyer et al. 2013). In recent years, the largest source of salinity profiles is the profiling floats of the Argo program (Riser et al. 2016). These data are a mix of real-time (preliminary) and delayed-mode (scientific quality controlled) observations. Hence, the estimates presented here could change after all data are subjected to scientific quality control. The sea surface salinity (SSS) analysis relies on Argo data downloaded in January 2020, with annual maps generated following Johnson and Lyman (2012) as well as monthly maps of bulk (as opposed to skin) SSS data from the Blended Analysis of Surface Salinity (BASS; Xie et al. 2014). BASS blends in situ SSS data with data from the *Aquarius* (Le Vine et al. 2014; mission ended in June 2015), Soil Moisture and Ocean Salinity (SMOS; Font et al. 2013), and recently from Soil Moisture Active Passive (SMAP; Fore et al. 2016) satellite missions. Despite the larger uncertainties of satellite data relative to Argo data, their higher spatial and temporal sampling allows higher spatial and temporal resolution maps than are possible using in situ data alone at present. All salinity values used in this section are dimensionless and reported on the Practical Salinity Scale-78 (PSS-78; Fofonoff and Lewis 1979).

2) Sea surface salinity—G. C. Johnson and J. M. Lyman

Unlike sea surface temperature (SST), for which anomalies tend to be damped by air–sea heat exchanges, SSS has no direct feedback with the atmosphere, so large-scale SSS anomalies can more easily persist over years. For instance, the 2019 fresh subpolar SSS anomaly observed in the northeast Pacific (Fig. 3.7a) arguably began in 2016, centered more in the central subpolar North Pacific, shifting eastward and building somewhat in strength and size between then and

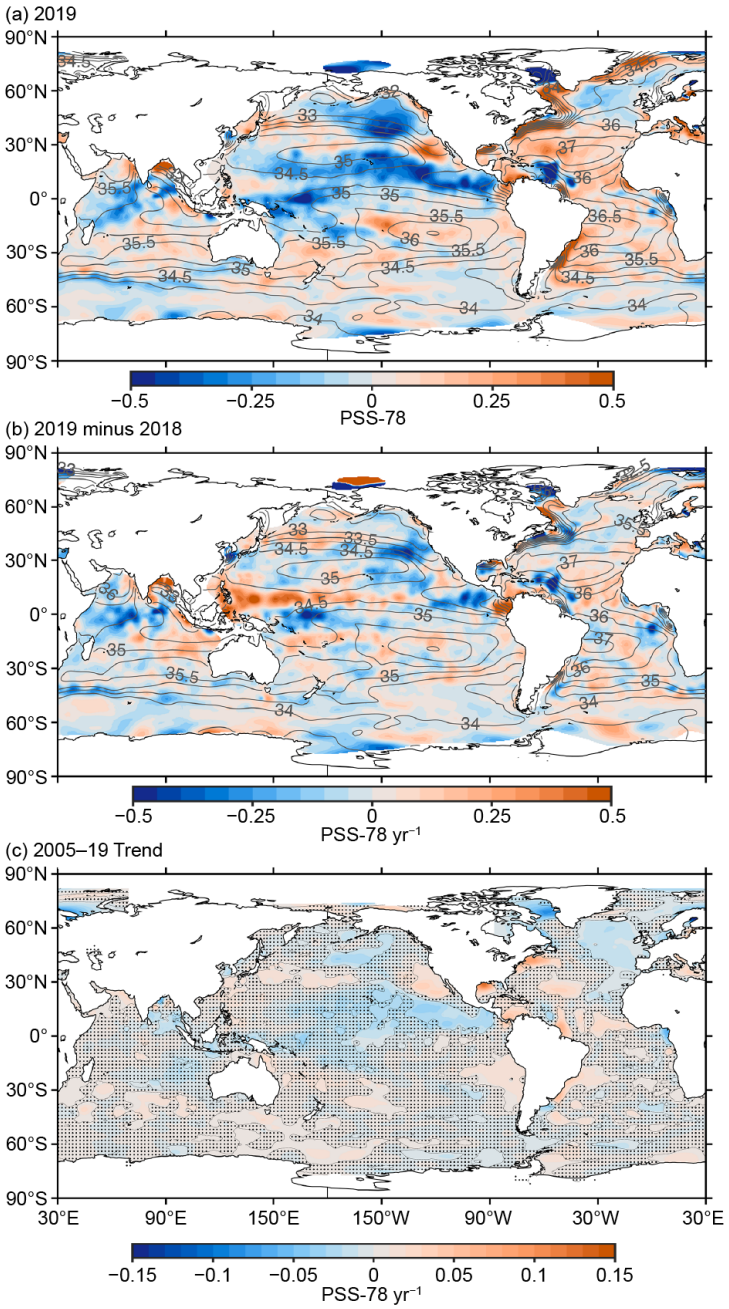

Fig. 3.7. (a) Map of the 2019 annual surface salinity anomaly (colors, PSS-78) with respect to monthly climatological 1955–2012 salinity fields from WOA13v2 (yearly average, gray contours at 0.5 intervals, PSS-78). (b) Difference of 2019 and 2018 surface salinity maps (colors, PSS-78 yr^{-1}). White ocean areas are too data-poor (retaining < 80% of a large-scale signal) to map. (c) Map of local linear trends estimated from annual surface salinity anomalies for 2005–19 (colors, PSS-78 yr^{-1}). Areas with statistically insignificant trends at 5%–95% confidence are stippled. All maps are made using Argo data.

now (see previous *State of the Climate* reports). This fresh anomaly may be associated with the marine heat waves in the area that occurred in 2014–16 (e.g., Gentemann et al. 2017) and again in 2019 (see Fig. 3.1a). A fresh anomaly like this one would tend to increase stratification and reduce the ability of storms to deepen the mixed layer into colder subsurface water during winter, possibly even promoting warm SST anomalies.

In the tropical Pacific, the fresh 2019 SSS anomaly (Fig. 3.7a) observed over much of the ITCZ and South Pacific Convergence Zone (SPCZ) began around 2015 (see previous *State of the Climate* reports). While the location and strength have fluctuated somewhat, the persistence of this feature may be linked to increased precipitation in the area expected during El Niño conditions, which have occurred twice between 2015 and 2019. In the tropical Atlantic, the fresh anomaly north of the Amazon and Orinoco River outlets has grown from 2016 to 2019. In contrast to these longer-term patterns, the tropical Indian Ocean was mostly anomalously salty in the east and anomalously fresh in the west in 2019 (Fig. 3.7a), a pattern dominated by the changes from 2018 to 2019 (Fig. 3.7b) and perhaps related to the strongly positive phase of the Indian Ocean dipole (IOD) in 2019 (Fig. 3.1), which brings more precipitation to the west and drier conditions to the east (Fig. 3.11).

In 2019, salty SSS anomalies are associated with the subtropical salinity maxima in the South Indian, the South Pacific, and the North and South Atlantic Oceans (Fig. 3.7a), patterns that have largely persisted since at least 2006, the first year the *State of the Climate* reported on SSS. Also in the subtropics, the 2005–19 SSS trend is toward saltier conditions, with some subtropical regions in all of those oceans exhibiting salinification statistically significantly different from zero with 5%–95% uncertainty ranges (Fig. 3.7c, unstippled orange areas). In contrast, the subpolar North Pacific and North Atlantic both have large regions with statistically significant freshening trends over 2005–19. These patterns are all consistent with an increase in the hydrological cycle over the oceans as the atmosphere warms and, therefore, can carry more water from regions (i.e., subtropical) where evaporation dominates to regions (i.e., subpolar) where precipitation (and river runoff) dominates (Rhein et al. 2013). In

the Indian Ocean, there are also 2005–19 trends toward saltier values in the already salty Arabian Sea and fresher values in the already fresh Bay of Bengal. Finally, both the Brazil Current in the subtropical South Atlantic and the Gulf Stream extension are anomalously salty in 2019 (Fig. 3.7a) and show statistically significant trends toward saltier values from 2005 to 2019, with both areas having strong warming trends from 0–700 m as well (Fig. 3.4c).

In 2019, the seasonal BASS (Xie et al. 2014) SSS anomalies (Fig. 3.8) show the persistence of the Northern Hemisphere (NH) subpolar fresh anomalies and subtropical salty anomalies in both hemispheres. Tropical anomalies tend to be more seasonal, with the fresh anomaly in the Pacific ITCZ being strongest in boreal winter and spring, and the fresh anomaly north of the Amazon and Orinoco outflows in the western tropical Atlantic being strongest in boreal summer and autumn. With their higher spatial and temporal resolution, BASS data also confirm the persistent salty anomalies in the Brazil Current and the Gulf Stream extension, both regions with large SSS gradients near the coast, where the relatively sparse Argo sampling could cause mapping artifacts.

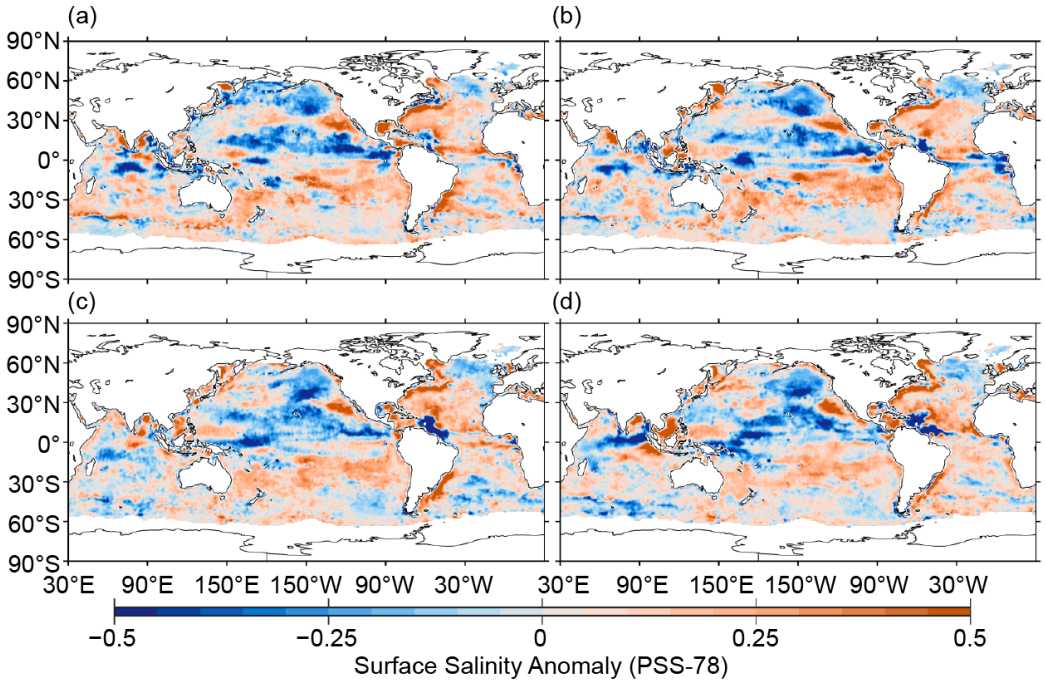

Fig. 3.8. Seasonal maps of SSS anomalies (colors, PSS-78) from monthly blended maps of satellite and in situ salinity data (BASS; Xie et al. 2014) relative to monthly climatological 1955–2012 salinity fields from WOA13v2 for (a) Dec–Feb 2018/19, (b) Mar–May 2019, (c) Jun–Aug 2019, and (d) Sep–Nov 2019. Areas with maximum monthly errors exceeding 10 PSS-78 are left white.

3) Subsurface salinity—J. Reagan, T. Boyer, C. Schmid, and R. Locarnini

Subsurface salinity anomalies primarily originate near the surface where they are largest and then weaken with depth; however, as these anomalies enter ocean's deeper depths they may persist for years or even decades. The Atlantic basin-average monthly salinity anomalies (relative to the long-term mean from the World Ocean Atlas 2013; Zweng et al. 2013) exhibited a similar pattern for the entire 2010–19 decade (Fig. 3.9a). Salty (>0.01) anomalies dominated the upper 500 m with increasing salty anomalies near the surface (>0.05) and mostly weak anomalies (< |0.005|) at depths greater than 500 m throughout the decade. In 2019, and for the second consecutive year, the Atlantic Ocean basin experienced salty anomalies throughout the year from 0–1500 m. Since late 2015, large salinity anomalies (>0.04) that initially only existed near the surface have deepened to ~200 m in late 2019. There is also evidence of salty anomalies (>0.01) deepening

between 200 and 600 m from 2018 to 2019 (Figs. 3.9a,b). The progression of these deepening salinity anomalies since 2015 can be seen in prior year-to-year changes (Figs. 3.9b in Reagan et al. 2017, 2018, 2019). From 2018 to 2019 there was also an increase in salinity of ~0.15 in the upper 50 m of the Atlantic Ocean (Fig. 3.9b), which is a reversal of the freshening seen between 2017 and 2018 (Fig. 3.9b in Reagan et al. 2019).

The 2018–19 statistically significant (> ±1 std. dev., see description of significance in Fig. 3.9) changes in the Atlantic basin zonal-average salinity anomalies (Fig. 3.9c) show salinification (>0.03) between 7°–20°N from the surface down to ~250 m, which may be the main driver for the salinification in the upper 50 m of the Atlantic basin (Fig. 3.9b), and freshening from 40°–45°N extending from the surface (maximum of ~ −0.15) down to 300 m (~ −0.03). There also is salinification in the upper 100 m north of 60°N. In the South Atlantic, weak salinification (~0.03) from the surface to ~200 m centered near 45°S and subsurface freshening (~ −0.03) centered near 25°S and 150 m are evident.

The 2019 Pacific basin-average monthly salinity anomalies revealed a similar pattern to that present since mid-2014 (Fig. 3.9d). There were large fresh anomalies (< −0.02) in the upper 100 m, salty anomalies (>0.01) from 125 to 225 m, fresh anomalies (< −0.005) from 300 to 550 m, and mostly weak anomalies (< |0.005|) below 700 m. From 2017 to 2018 there was a notable deepening of salty anomalies in the Pacific centered around 200 m (Figs. 3.9c,d in Reagan et al. 2019); however, this deepening of salty anomalies ceased in 2019 (Figs. 3.9d,e). Additionally, from 2018 to 2019 there is freshening (~ −0.01 maximum at 75 m) between 50 and 125 m (Fig. 3.9e) corresponding to a slight deepening of freshening in the Pacific (Fig.

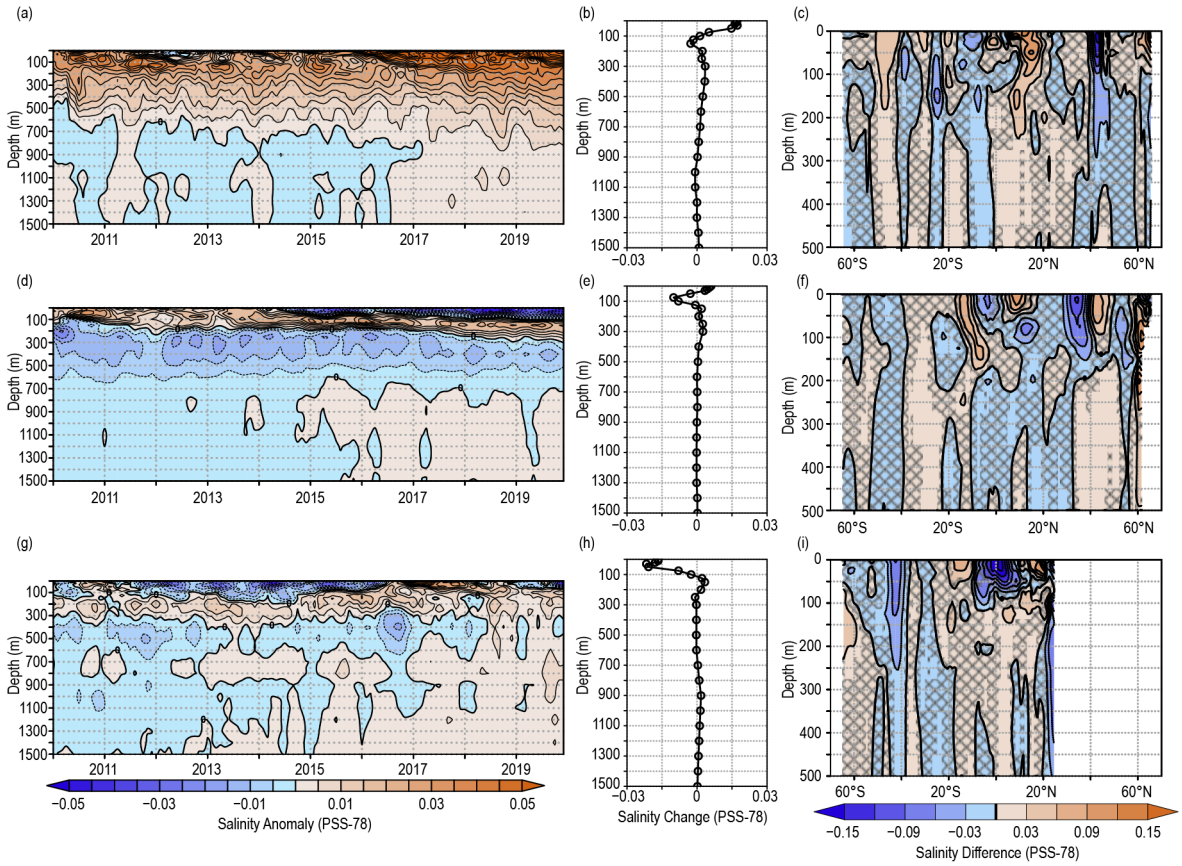

Fig. 3.9. Average monthly salinity anomalies from 0–1500 m for 2010–19 for the (a) Atlantic, (d) Pacific, and (g) Indian basins. Change in salinity from 2018 to 2019 for the (b) Atlantic, (e) Pacific, and (h) Indian basins. Change in the 0–500 m zonal-average salinity from 2018 to 2019 in the (c) Atlantic, (f) Pacific, and (i) Indian basins with areas of statistically insignificant change, defined as < ±1 std. dev. and calculated from all year-to-year changes between 2005 and 2019, stippled in dark gray. Data were smoothed using a 3-month running mean. Anomalies are relative to the long-term (1955–2012) WOA13v2 monthly salinity climatology (Zweng et al. 2013).

3.9d). However, in the upper 30 m there was slight salinification between 2018 and 2019 (~0.005 maximum at 0 m, Fig. 3.9e), which is the first basin-average SSS in the Pacific since 2015–16 (Fig. 3.9d in Reagan et al., 2017).

The statistically significant changes in the Pacific basin zonal-average salinity anomalies (Fig. 3.9f) from 2018 to 2019 are mainly confined to the upper 200 m. There is salinification (>0.06) in a narrow zonal band near 13°S (at 0 m) extending to ~150 m at 8°S, as well as salinification (>0.06) in the upper 40 m between 5°N and 15°N, between 40°N and 47°N extending from the surface to ~75 m, and finally in the subsurface north of 58°N. The main region of freshening (< −0.03) is between 28°N and 39°N, extending from the surface to 150 m. Other statistically significant freshening tendencies occurred in a subsurface pocket centered at 12°N and 75 m and near the surface at 5°S.

The 2019 Indian basin-average monthly salinity anomalies (Fig. 3.9g) revealed freshening (< −0.02) during the later months (October–December) of 2019 in the upper 50 m, with salinification (>0.005) at deeper depths. Unlike the Atlantic and Pacific, the Indian basin has not demonstrated repeating patterns of basin-average monthly salinity anomalies throughout this past decade. The change in the basin-average salinity between 2018 and 2019 reveals strong freshening (< −0.015) in the upper 50 m (Fig. 3.9h), with weak salinification (<0.005) between 125–200 m.

Statistically significant changes in zonal-average monthly salinity anomalies from 2018 to 2019 (Fig. 3.9i) in the Indian basin show that much of the near-surface freshening in Fig. 3.9h is a product of freshening (< −0.03) between 10°S and 10°N, extending from the surface down to 75 m, which may be related to the positive IOD in 2019 (Fig. 3.1) and its accompanying anomalous precipitation (Fig. 3.11) and zonal currents (Fig. 3.17). Additional freshening (< −0.03) occurred between 47°S and 39°S that extends from the surface to 250 m, narrowing with increasing depth. Salinification (>0.03) occurred in multiple pockets south of 60°S centered at 150 m and in two areas near the surface centered at 15°S and 18°N.

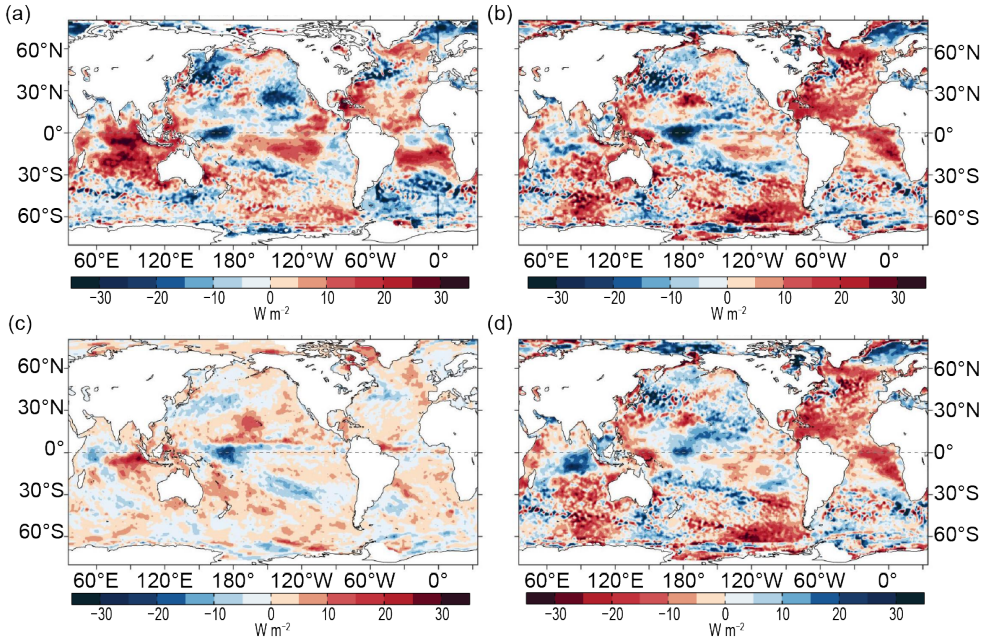

Fig. 3.10. (a) Surface heat flux (Q_{net}) anomalies (W m^{-2}) for 2019 relative to the 2001–15 climatology. Positive values denote ocean heat gain. (b) 2019 minus 2018 change for Q_{net}, (c) surface radiation (SW+LW), and (d) turbulent heat fluxes (LH+SH), respectively. Positive (negative) changes denote more ocean heat gain (loss) in 2019 than in 2018, consistent with the reversal of the color scheme in (d). LH+SH are produced by the OAFlux2 satellite-based high-resolution analysis, and SW+LW by the NASA FLASHFlux project.

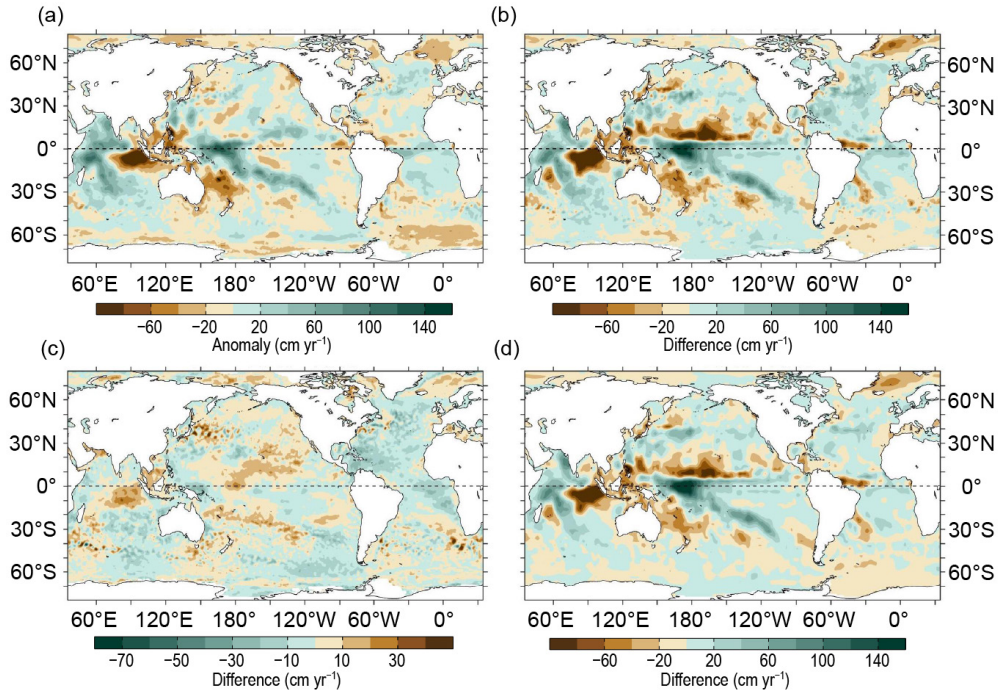

Fig. 3.11. (a) Surface freshwater (*P*–*E*) flux anomalies (cm yr^{-1}) for 2019 relative to the 1988–2015 climatology. 2019 minus 2018 changes for (b) *P*–*E*, (c) evaporation (*E*), and (d) precipitation (*P*). Green colors denote anomalous ocean fresh water gain, and browns denote loss, consistent with the reversal of the color scheme in (c). *P* is computed from the GPCP version 2.3 product, and *E* from OAFlux2.

e. Global ocean heat, freshwater, and momentum fluxes—L. Yu, Paul. W. Stackhouse, A. C. Wilber, and R. A. Weller

The ocean and the atmosphere communicate via interfacial exchanges of heat, freshwater, and momentum. These air–sea fluxes are the primary mechanisms for keeping the global climate system in balance with the incoming insolation at Earth's surface. Most of the shortwave radiation (SW) absorbed by the ocean's surface is vented into the atmosphere by three processes: longwave radiation (LW), turbulent heat loss by evaporation (latent heat flux, or LH), and by conduction (sensible heat flux, or SH). The residual heat is stored in the ocean and redistributed by the ocean's circulation, forced primarily by the momentum transferred to the ocean by wind stress. Evaporation connects heat and moisture transfers, and the latter, together with precipitation, determines the local surface freshwater flux. Identifying changes in the air–sea fluxes is essential in deciphering observed changes in ocean circulation and its transport of heat and salt from the tropics to the poles.

Air–sea heat flux, freshwater flux, and wind stress in 2019 and their relationships with ocean surface variables are examined here. The net surface heat flux, Q_{net}, is the sum of four terms: SW + LW + LH + SH. The net surface freshwater flux into the ocean (neglecting riverine and glacial fluxes from land) is simply precipitation (*P*) minus evaporation (*E*), or the *P*–*E* flux. Wind stress is computed from satellite wind retrievals using the bulk parameterization of Edson et al. (2013). The production of the global maps of Q_{net}, *P*–*E*, and wind stress (Figs. 3.10–3.13) and the long-term perspective of the change of the forcing functions (Fig. 3.13) are made possible through integrating multi-group efforts. Ocean-surface LH, SH, *E*, and wind stress are from the Objectively Analyzed air-sea Fluxes (OAFlux) project's second-generation products (hereafter OAFlux2). Surface SW and LW radiative fluxes are from the Clouds and the Earth's Radiant Energy Systems (CERES) Fast Longwave And Shortwave Radiative Fluxes (FLASHFlux) Ed3A product (Stackhouse et al. 2006). Global P is from the Global Precipitation Climatology Project (GPCP) version 2.3 products (Adler et al. 2018). The CERES Energy Balanced and Filled (EBAF) surface SW and LW version 4.1 products (Loeb et al. 2018; Kato et al. 2018) are used in the time series analysis.

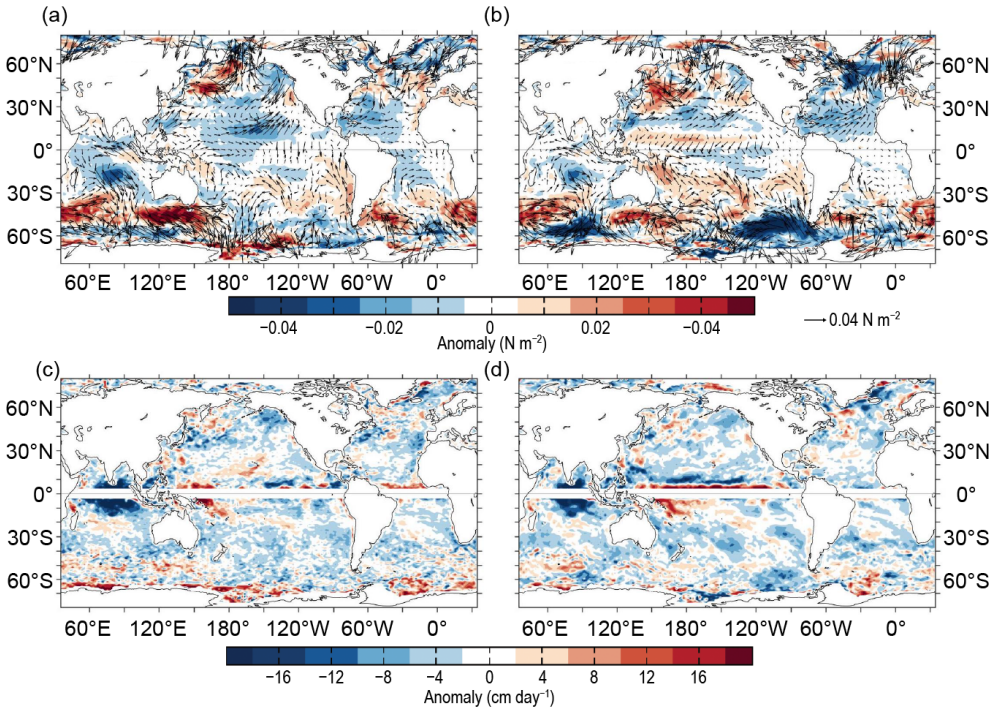

Fig. 3.12. (a) Wind stress magnitude (colors) and vector anomalies (N m^{-2}) for 2019 relative to the 1988–2015 climatology, (b) 2019 minus 2018 changes in wind stress, (c) Ekman vertical velocity (W_{EK}; cm day^{-1}) anomalies for 2019 relative to the 1988–2015 climatology, and (d) 2019 minus 2018 changes in W_{EK}. In (c) and (d), positive values denote upwelling change, and negative downwelling change. Winds are computed from OAFlux2.

1) Surface heat fluxes

The 2019 anomaly field (Fig.3.10a) is dominated by pronounced oceanic heat gain anomalies (positive Q_{net} anomalies) in the tropical Indian Ocean, with the maximum anomalies exceeding 30 W m^{-2} located off the equator near 5°S. These anomalies were associated with an unusually strong positive Indian Ocean dipole (IOD) event in 2019, featuring warmer-than-average waters in the western Indian Ocean and cooler waters in the eastern Indian Ocean. The positive event started to develop in June 2019 and peaked in October–November 2019. The Dipole Mode Index (DMI; Saji et al. 1999; see section 4h) suggested that the event was one of the strongest in history. A positive IOD is typically characterized by higher pressures, less cloud, and less rain over the cooler waters in the eastern basin and vice versa in the western basin. Both SW+LW and LH+SH 2018/19 changes (Figs. 3.10c,d) displayed a dipole-like pattern in the tropical Indian Ocean corresponding to the changing sea surface temperature anomaly (SSTA) pattern. In the east, SW+LW increased and had a warming effect on the surface water. Meanwhile, ocean turbulent heat loss (positive LH+SH anomalies, blue colors) also increased, which tended to vent the surface radiative flux back to the atmosphere and cool the surface water. Note that the color scheme for LH+SH is reversed so that increased LH+SH (positive anomalies) have a cooling effect (blue colors) on the ocean surface and, conversely, reduced LH+SH (negative anomalies) have a warming effect (red colors). The competing effects between SW+LW and LH+SH 2018/19 changes canceled out the impacts of each other, leading to slight net heat loss changes over most of the tropical basin. The Q_{net} 2018/19 change map in the Indian Ocean differs considerably from the Q_{net} anomaly map (Figs. 3.10a,b). The reason is that there was a short-lived IOD event in 2018; although it was weak, a similar SSTA pattern triggered similar responses in the atmosphere (Yu et al. 2019). Thus, the eastern Indian Ocean received anomalous heating in both 2018 and 2019, and the differences in Q_{net} between the two years were relatively small.

The equatorial Pacific experienced a transition from a diminishing La Niña in 2018 to the development of a weak El Niño in 2019. Both SW+LW and LH+SH showed a tendency to induce an anomalous ocean warming in the central and eastern equatorial Pacific where SSTA were

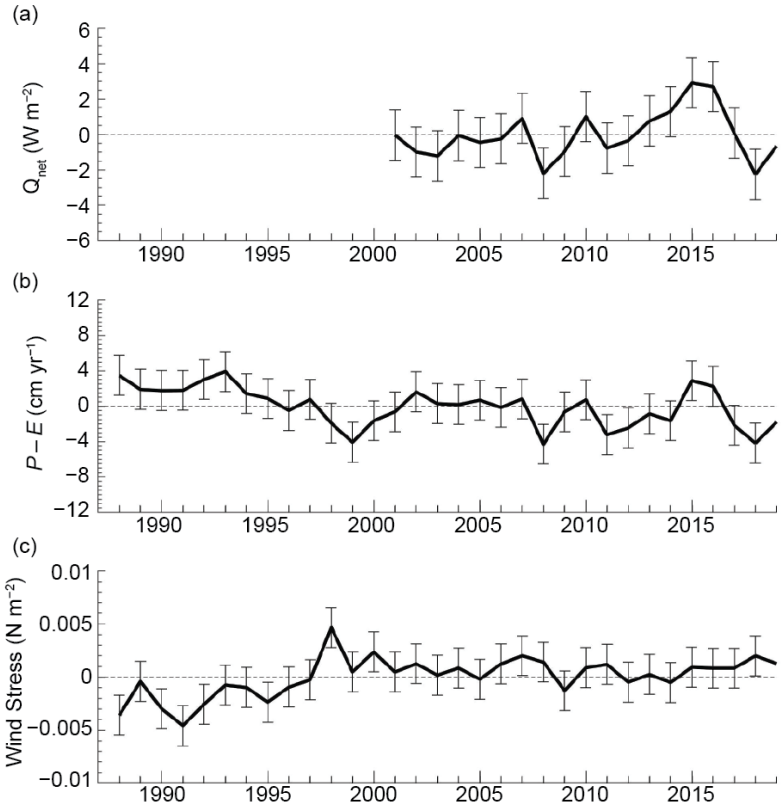

Fig. 3.13. Annual-mean time series of global averages of (a) net surface heat flux (Q_{net}; W m^{-2}) from the combination of CERES EBAF4.1 SW+LW and OAFlux2 LH+SH. The 2019 Q_{net} estimate is based on FLASHFlux and OAFlux-HR. (b) Net freshwater flux ($P-E$; cm yr^{-1}) from the combination of GPCP P and OAFlux2 E and (c) wind stress magnitude (N m^{-2}) from OAFlux2. The shaded area denotes 1 std. dev. of annual mean variability.

positive, and an anomalous ocean cooling in the western Pacific warm pool where SSTA were negative. Q_{net} is positively correlated with El Niño–Southern Oscillation (ENSO) SSTA. Outside of the equatorial Pacific, the radiative and turbulent heat flux 2018/19 changes both created a cooling effect in the vicinity of the Kuroshio-Oyashio Extension. Weak positive Q_{net} anomalies were observed in the northeast Pacific off the shores of Alaska where a "warm blob" (Bond et al. 2015) with weak SSTAs anomalies surged back briefly. In general, LH+SH changes dominated the Q_{net} changes. The large oceanic turbulent heat loss (blue colors) in the central Pacific between the equator and 30°N appears to be associated with the Pacific Meridional Mode (PMM; Chiang and Vimont 2004).

In the Atlantic Ocean, 2019 started with a positive phase of the North Atlantic Oscillation (NAO), switched to negative in May, and then was slightly positive in November–December, with an annual mean index of ~ −0.3. There was a tripole-like SSTA pattern in the North Atlantic, showing negative SSTA in the Gulf Stream and extension and positive SSTAs elsewhere between the equator and 60°N (see Fig. 3.1). Positive SSTA occurred also in the tropical Atlantic corresponding to the development of an Atlantic Niño. Corresponding to the SSTA pattern, there were widespread positive Q_{net} 2018/19 changes from 30°S to 60°N, and this anomalous oceanic heat gain was also large compared to the climatological mean condition.

2) Surface freshwater fluxes

The 2019 $P-E$ anomaly fields (Fig. 3.11a) show that net freshwater input at the ocean surface increased in the western tropical Indian Ocean (positive anomalies, green colors) but decreased considerably in the eastern Indian Ocean (negative anomalies, brown colors). The pattern was the result of the unusually strong 2019 IOD. The colder sea surface in the eastern Pacific corresponded with enhanced evaporation and reduced precipitation, both of which produced anomalously evaporative conditions in the region. In the tropical Pacific, the oceanic net freshwater input was slightly above the climatological condition along the Intertropical Convergence Zone (ITCZ) and South Pacific Convergence Zone (SPCZ).

The 2018/19 changes in the tropical Pacific (Fig. 3.11b) were associated with the transition of the ENSO cycle from a diminishing La Niña in 2018 to the development of a weak El Niño in 2019. The *P*–*E* changes are attributable to the *P* changes (Fig. 3.11d) and are consistent with the SW+LW changes, showing that SW+LW decreased in areas of increased ITCZ rainfall and increased in areas of reduced ITCZ rainfall.

Outside the tropics, the largest evaporative 2018/19 changes occurred in the Nordic Seas, produced by the combined effect of an increase of *E* and a reduction of *P*, indicating that the region had a deficit in surface freshwater input in 2019. In the Gulf of Alaska where a "warm blob" surged back briefly, a weak evaporative condition was induced by a weak reduction in *P* flux. The *E* anomalies pattern in the North Pacific resemble the SSTA associated with the PMM, indicating that ocean evaporation was enhanced when SST increased in this region.

3) Wind stress

The 2019 wind stress anomaly pattern (Fig. 3.12a) shows that the trade winds weakened (negative anomalies) in two major regions: the central tropical North Pacific and the tropical South Indian Ocean. The former is related to the PMM (Chiang and Vimont 2004) and the latter to the IOD. Marked increase of westerly winds is noted in the Indian (20°–160°E) and Atlantic (60°W–30°E) sectors along the Atlantic Circumpolar Current (ACC; 40°–60°S). Weakening of surface winds in the North Atlantic is also seen, as is the weakening of surface winds in the northeast Pacific associated with the occurrence of the "warm blob." The 2018/19 wind stress changes (Fig. 3.12b) show a similar pattern, except for the band of positive anomalies located north of equator in the Pacific. The trade winds in this region, although still weaker than the climatological mean state, enhanced slightly from the 2018 condition.

The spatial variations of winds cause divergence and convergence of the Ekman transport, leading to a vertical velocity, denoted by Ekman pumping (downward) or suction (upward) velocity W_{EK} at the base of the Ekman layer. Computation of W_{EK} follows the equation: $W_{EK} = 1/r\tilde{N}´(t/f)$, where *r* is the density, t is the wind stress magnitude, and *f* the Coriolis parameter. The 2019 W_{EK} anomaly pattern (Fig. 3.12c) is dominated by large downwelling (negative) anomalies in the equatorial Indian Ocean, indicating that the typical upwelling conditions in the region weakened considerably during the 2019 IOD event. Outside the tropical region, the 2019 W_{EK} anomalies were generally weak and less organized except for the Indian Ocean sector along the ACC, where the typical upwelling condition was slightly enhanced. The 2018/19 W_{EK} change pattern (Fig. 3.12d) has similar features.

4) Long-term perspective

A long-term perspective on the change of ocean-surface forcing functions in 2019 is examined in the context of multi-decade annual-mean time series of Q_{net}, *P*–*E*, and wind stress averaged over the global ice-free oceans (Figs. 3.13a–c). The Q_{net} time series commenced in 2001, when CERES EBAF4.1 surface radiation products became available. The *P*–*E* and wind stress time series are each 32 years long, starting from 1988 when higher quality global flux fields can be constructed from Special Sensor Microwave/Imager (SSM/I) satellite retrievals. Q_{net} anomalies are relative to the 2001–15 climatology, with positive (negative) anomalies denoting increased (reduced) net downward heat flux into the ocean. *P*–*E* anomalies are relative to the 1988–2015 climatology, with positive (negative) anomalies denoting increased (reduced) freshwater flux into the ocean. Wind stress anomalies are also relative to the 1988–2015 climatology, with positive (negative) anomalies denoting increased (reduced) wind stress magnitude over the ocean.

Q_{net} was relatively constant between 2001 and 2007 but had large interannual fluctuations thereafter. The total downward heat flux into the global ocean increased by about 3 W m^{-2} during 2011–16, when the tropical Pacific switched from a strong La Niña event in 2011 to a strong El Niño event in 2016. This period of increasing oceanic heat gain coincided with an increase of global

mean SST by about 0.35°C (Fig. 3.3). Q_{net} reduced sharply by about 4 W m^{-2} during the 2017/18 La Niña but bounded back slightly in 2019. *P–E* shows similar interannual variability to that of Q_{net}. In particular, the freshwater input into the ocean increased during the transition from the 2011 La Niña to the 2016 El Niño, reduced during the 2017/18 La Niña, and bounced back slightly in the 2019 weak El Niño phase. It should be noted that the interannual variability in the Q_{net} record is dominated by turbulent heat flux components (LH and SH), while that in the *P–E* record is governed by the *P* component. The time series of wind stress was flat in the most recent two decades after a regime shift around 1999, and the 2019 winds were slightly down from the 2018 level.

f. Sea level variability and change—P. R. Thompson, M. J. Widlansky, E. Leuliette, W. Sweet, D. P. Chambers, B. D. Hamlington, S. Jevrejeva, J. J. Marra, M. A. Merrifield, G. T. Mitchum, and R. S. Nerem

Global mean sea level (GMSL) during 2019 became the highest annual average in the satellite altimetry record (1993–present), rising to 87.6 mm (3.4 in) above the 1993 average (Fig. 3.14a). This marks the eighth consecutive year (and 24th out of the last 26) that GMSL increased relative to the previous year. The new high reflects an ongoing multi-decadal trend in GMSL during the satellite altimetry era, 3.2 ± 0.4 mm yr^{-1} (Fig. 3.14a). Acceleration in GMSL (i.e., two times the quadratic coefficient in a second-order polynomial fit) during the altimetry era is 0.097 ± 0.04 mm yr^{-2}. When effects of the Pinatubo volcanic eruption and El Niño–Southern Oscillation (ENSO) are subtracted from GMSL variability, the estimated climate-change-driven rise in GMSL over the altimeter record is 2.3 ± 0.7 mm yr^{-1} with an acceleration of 0.084 ± 0.025 mm yr^{-2} (Nerem et al. 2018).

Variations in GMSL (Fig. 3.14a) result from changes in both the mass and density of the global ocean (Leuliette and Willis 2011; Cazenave et al. 2018). Steric (i.e., density-related) sea level rise observed by the Argo profiling float array during 2005–19, 1.3 ± 0.2 mm yr^{-1}, which is mostly due to ocean warming, accounted for about one-third of GMSL change since 2005, 3.7 ± 0.4 mm yr^{-1}. Increasing global ocean mass observed by the NASA Gravity Recovery and Climate Experiment (GRACE) and GRACE Follow-On (GRACE-FO) missions, 2.8 ± 0.4 mm yr^{-1}, contributed the remaining two-thirds of the GMSL trend during 2005–19. The positive trend in ocean mass primarily

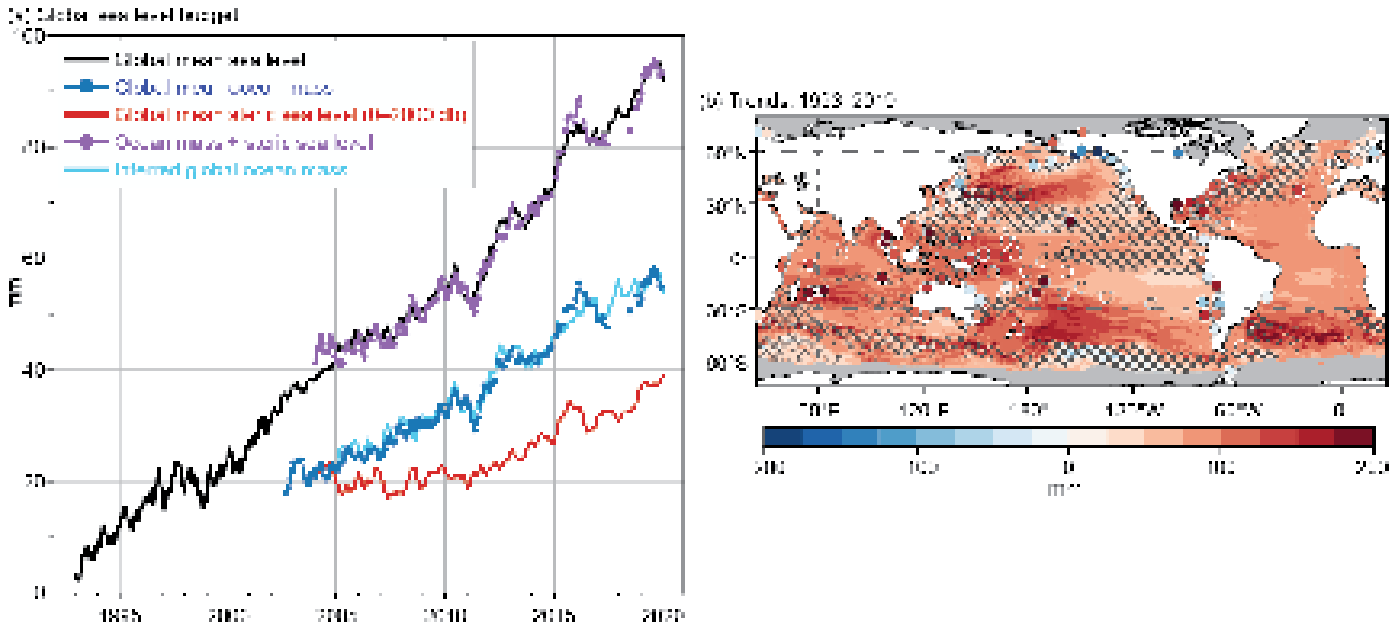

Fig. 3.14. (a) Monthly averaged GMSL observed by satellite altimeters (black, 1993–2019 from the NOAA Laboratory for Satellite Altimetry), global ocean mass (blue, 2003–19 from the Gravity Recovery and Climate Experiment), global mean steric sea level (red, 2004–19) from the Argo profiling float array, mass plus steric (purple), and inferred global ocean mass (cyan) calculated by subtracting global mean steric sea level from global mean sea level. All time series have been smoothed with a 3-month filter. (b) Total local sea level change during 1993–2019 as measured by satellite altimetry (contours) and tide gauges (circles). Hatching indicates trends that are not statistically significant.

resulted from melting of glaciers and ice sheets (see sections 5e,f, 6e), which was partially offset by increased hydrological storage of fresh water on land, −0.7 ± 0.2 mm yr^{-1} (Reager et al. 2016).

Annually averaged GMSL from satellite altimetry increased by 6.1 mm from 2018 to 2019 (Fig. 3.14a). Annual global mean steric sea level observed by Argo (0–2000 m) increased by 4.5 mm from 2018 to 2019 (Fig. 3.14a), which was primarily due to an increase in heat content over the upper 700 m of the ocean (see Fig. 3.6a). Due to lack of complete GRACE data during 2018, we cannot directly assess the contribution of global mean ocean mass to GMSL change from 2018 to 2019. Failure of an accelerometer and degrading batteries resulted in a lack of valid data after June 2017 and termination of the original GRACE mission in October 2017. GRACE-FO first provided valid ocean mass estimates in June 2018 after an 11-month gap in ocean mass data. Despite this gap, we can attempt to infer the contribution from ocean mass by subtracting global mean steric sea level from GMSL (Fig. 3.14a) and assuming no steric change below 2000 m. The inferred ocean mass curve suggests a modest contribution of 1.5 mm from ocean mass to the year-over-year increase in GMSL.

The spatial structure in sea level change over the relatively short altimeter record is primarily due to natural fluctuations in coupled modes of atmosphere–ocean variability, such as the relationship between east-west differences in Pacific trends and a multidecadal tendency toward La Niña-like conditions and stronger Pacific trade winds (e.g., Merrifield 2011, Fig. 3.14b). However, there is growing evidence that at least a portion of the sea level trend pattern from altimetry, particularly in the Indian Ocean and southwest Pacific, represents the response of the ocean to anthropogenic forcing (Fasullo and Nerem 2018; Hamlington et al. 2019), which may continue into future decades. The natural and forced contributions combine to produce substantial spatial differences in rates of rise. For example, sea surface height from satellite altimetry has increased 150 mm since 1993 around Sydney, while Los Angeles has experienced just over 20 mm during that time. It is also important to note that sea level change relative to land (i.e., relative sea level, the quantity measured by tide gauges) is most relevant for societal impacts and can differ substantially from satellite-derived changes in tectonically active regions (e.g., Japan) and areas strongly affected by glacial isostatic adjustment (e.g., Alaska; Fig. 3.14b).

Positive annual sea level anomalies occurred almost everywhere during 2019 (Fig. 3.15a), which is consistent with the global pattern of sea level rise since 1993 (Fig. 3.14b). Other than

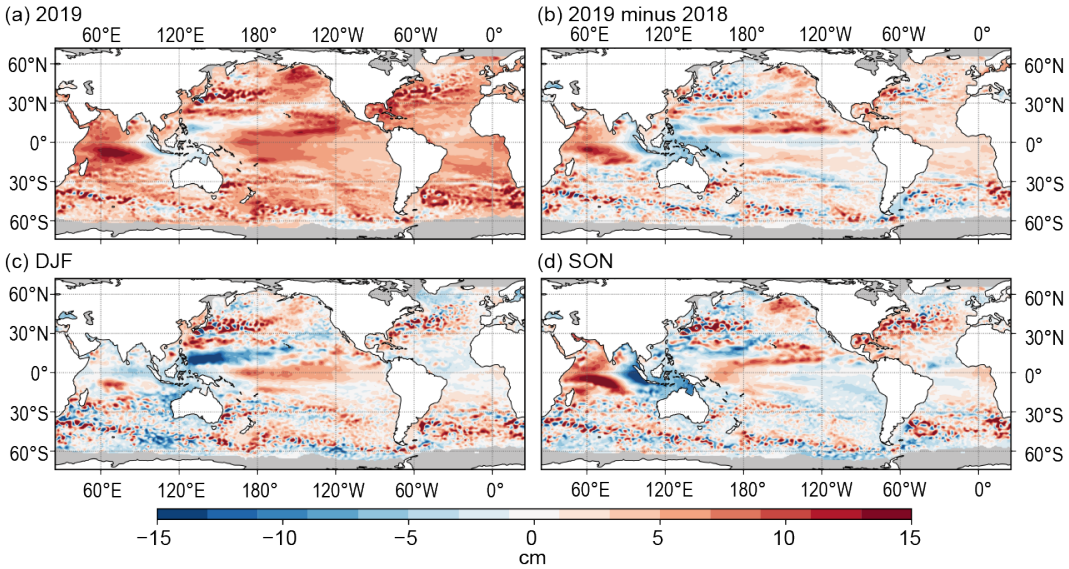

Fig. 3.15. (a) Annual average sea level anomaly during 2019 relative to the average sea level at each location during 1993–2019. (b) Average 2019 sea level anomaly minus 2018. (c) Average sea level anomaly during DJF 2019 relative to 1993–2019 average. (d) Same as (c), but for SON. GMSL was subtracted from panels (c),(d) to emphasize regional, non-secular change. Altimetry data were obtained from the gridded, multi-mission product maintained by the Copernicus Marine and Environment Monitoring Service (CMEMS).

isolated negative anomalies associated with upwelling mesoscale eddies (mostly in midlatitudes), the only large-scale region of negative height anomalies during 2019 is near the equator in the eastern Indian and western Pacific Oceans. In this broad region of below-normal sea levels that includes around parts of Indonesia, the Philippines, and New Guinea, the annual mean sea level decreased 5–10 cm from 2018 to 2019 (Fig. 3.15b) and reached the lowest levels near the end of the year (exceeding 15 cm below normal in the eastern Indian Ocean; Figs. 3.15c,d). To the west, in much of the remainder of the tropical Indian Ocean, sea levels increased by up to 15 cm relative to 2018 (Fig. 3.15b). Above- and below-normal sea levels in the Indian Ocean correspond to the regions of largest ocean heat content (OHC) anomalies (see Fig. 3.4a; higher in the west, lower in the east) and are consistent with the positive phase of the Indian Ocean dipole (IOD) that emerged in sea surface temperature (SST) observations during the second half of 2019 (see Figs. 3.2c,d).

Elsewhere in the Pacific Ocean, changes from 2018 to 2019 were for higher sea levels in much of the Northern Hemisphere (NH) away from the equator (Fig. 3.15b). In the tropical and central North Pacific, including around Hawaii, sea levels rose from below to above normal during 2019 (reaching as much as 15 cm above normal by the end of the year; Figs. 3.15c,d). A similar rise in sea level occurred in the Gulf of Alaska, whereas, along the equator east of the date line, sea levels dropped during the year (Figs. 3.15c,d). Overall, the Pacific sea level 2018/19 changes (i.e., lowering in the equatorial eastern Pacific and rising in the eastern half of the North Pacific) are consistent with the ending of El Niño (see section 3b; Fig. 3.1b) and ongoing positive Pacific Meridional Mode (PMM) conditions, which are both known to affect the OHC tendency (see Fig. 3.4b) in the respective regions (Long et al. 2020). In the tropical South Pacific, especially near the date line (i.e., between Fiji and the Samoan Islands), 2019 sea levels continued to rise from 2018 anomalies, which were already above normal due to wind stress curl anomalies there (see Fig. 3.12d).

In the Atlantic Ocean, the basin-scale change was for sea levels to rise from 2018 to 2019 (Fig. 3.15b). The increase was largest in the Caribbean Sea, Gulf of Mexico, and along the U.S. East Coast with the increase in these regions occurring primarily toward the end of 2019 (Figs. 3.15c,d). Including the long-term sea level rise trend (Fig. 3.14b), sea level anomalies generally exceeded 10 cm above the 1993–2019 average along the U.S. Gulf and East Coasts (Fig. 3.15a). Ocean heat content anomalies were similarly high in this region during 2019 (Fig. 3.4a), although changes relative to 2018 were small (see Fig. 3.4b). Ekman-pumping anomalies across the tropical North Atlantic were weakly negative (i.e., downward; Fig. 3.12d) and may have contributed to the high sea levels in the western North Atlantic via generation of downwelling Rossby waves (e.g., Calafat et al. 2018). Surface heat flux into the western Atlantic Ocean increased substantally in 2019 relative to 2018 (Figs. 3.10b,d), which likely contributed to higher sea levels as well via warming and expansion of the upper ocean.

Ongoing trends and year-to-year changes in sea level impact coastal communities by increasing the magnitude and frequency of positive sea level extremes that cause flooding and erosion. In many areas, coastal infrastructure is currently exposed to minor high tide flooding when water levels exceed a threshold defined by the top 1% of observed daily maxima from a global network of tide gauges (Sweet et al. 2014). These thresholds vary geographically (Fig. 3.16a) but are typically around 0.5 m above mean higher high water (MHHW)—the average of observed daily maxima—and are expected to be exceeded 3–4 times per year. The Gulf of Mexico and southeast U.S. coasts experienced greater-than-expected numbers of threshold exceedances during 2019 (Fig. 3.16b), which is directly related to positive sea level trends (Fig. 3.14b) and 2019 anomalies (Fig. 3.15a) in the region. Year-over-year increases in threshold exceedances occurred at a variety of locations, many of which correspond to regions in which mean sea level increased from 2018 to 2019. Specifically, the increase in mean sea level in the central North Pacific (Fig. 3.15b) contributed to an increase of more than five threshold exceedances in Hawaii compared to the previous year (Fig. 3.16b). Likewise, stations in the western Indian Ocean experienced a substantial increase

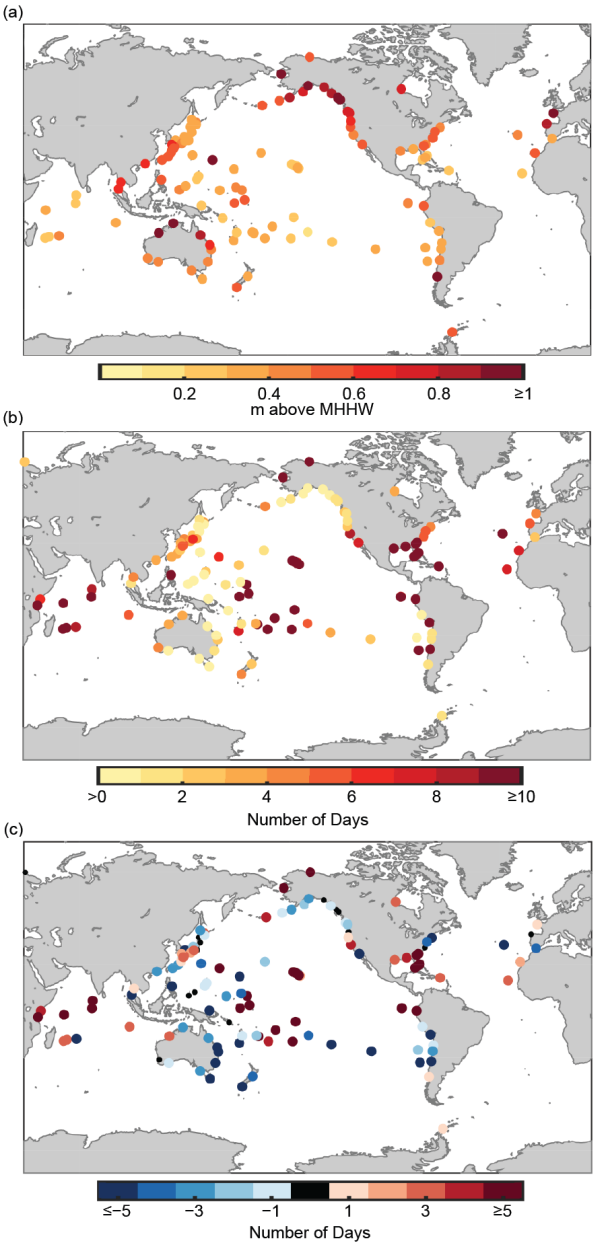

Fig. 3.16. (a) Nuisance-level flooding thresholds defined by the level of the top 1% of observed daily maxima during 2000–18 from tide gauge records. Units are in meters above mean higher high water (MHHW) calculated over 2000–18. (b) Number of daily maximum water levels during 2019 above the thresholds in (a). Small, black circles in (b) and (c) indicate a value of zero. (c) Same as in (b), but for 2019 minus 2018. Daily maximum water levels were calculated from hourly tide gauge observations obtained from the University of Hawaii Sea Level Center Fast Delivery database. Only records with at least 80% completeness during 2000–18 and 80% completeness during 2019 were analyzed.

in threshold exceedances related to high mean sea levels associated with the IOD event. In general, the changes in minor threshold exceedances highlight the importance of large-scale mean sea level anomalies for producing extremes.

g. Surface currents—R. Lumpkin and G. Goni

This section describes ocean surface current changes, transports derived from ocean surface currents, and features such as rings inferred from surface currents. Surface currents for this analysis are obtained from in situ (global array of drogued drifters and moorings) and satellite (altimetry and wind stress) observations. Transports are derived from a combination of sea surface height anomaly (from altimetry) and climatological hydrography. See the *State of the Climate in 2011* report for details of these calculations. Geostrophic zonal surface current anomalies are calculated with respect to 1993–2007 climatology and are discussed below for individual ocean basins.

1) Pacific Ocean

In 2019, the equatorial Pacific basin exhibited an annual mean zonal eastward geostrophic current anomaly of 10–12 cm s^{-1} from 152°E–180° (Fig. 3.17a). Between 112°–156°W, alternating eastward (at 10°N) and westward (6°–7°N) anomalies of 6–8 cm s^{-1} indicate that the North Equatorial Countercurrent (NECC) was shifted north of its climatological position, a pattern also seen in 2018. Because 2018 was characterized by an anomalously strong NECC spanning much of the basin, the 2019 minus 2018 anomaly difference (Fig. 3.17b) primarily reflects a weakening from the 2018 anomalies.

Figure 3.18 shows the development of zonal geostrophic current anomalies with respect to monthly climatology, averaged season by season. Eastward anomalies of ~10 cm s^{-1} along the path of the NECC, seen earlier in 2018, persisted in December–February 2018/19 (Fig. 3.18a), indicating a stronger-than-average current. Eastward anomalies exceeding 10 cm s^{-1} were present from 155°–160°E, 2°N–3°S, with peak anomalies of 28 cm s^{-1} on the equator. These anomalies weakened significantly in March–May (Fig. 3.18b). In June–August (Fig. 3.18c), westward anomalies of 10–12 cm s^{-1} developed in the northern core of the South Equatorial Current (nSEC) at 180°–110°W, 0°–4°N, a strengthening of this westward current. Westward anomalies were present across much of the basin by September–November (Fig. 3.18d) from 4°–8°N, but had weakened to 2–6 cm s^{-1}; north of this, eastward anomalies of 5–6 cm

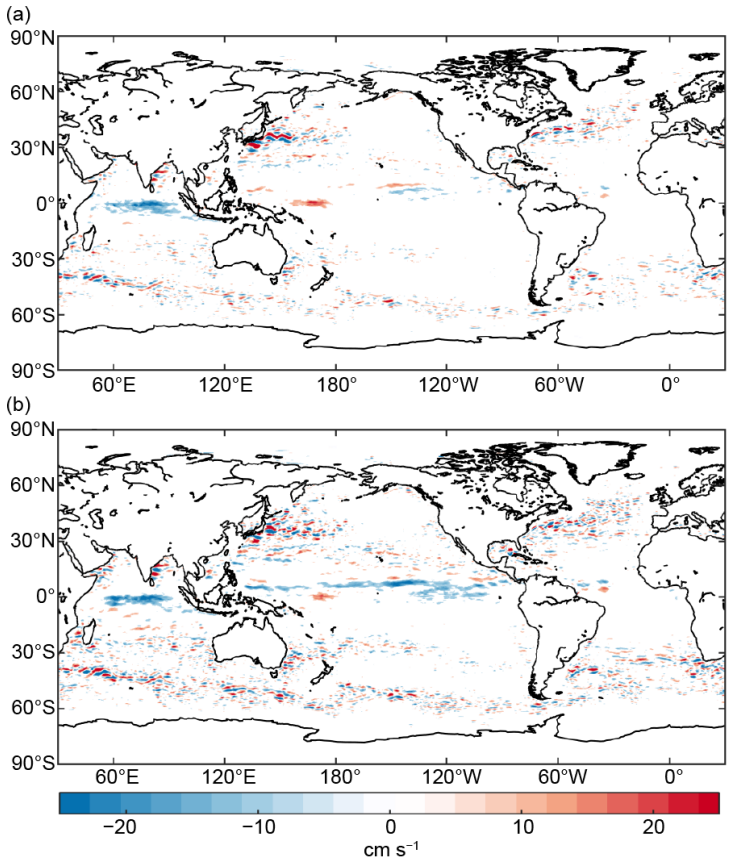

Fig. 3.17. Annually averaged geostrophic zonal current anomalies (cm s^{-1}) with respect to 1993–2007 climatology for (a) 2019 and (b) 2019 minus 2018 derived from a synthesis of drifters, altimetry, and winds. Values not shown where they are not significantly different from zero.

s^{-1} were centered on 10°N. These anomalies indicated a stronger-than-average nSEC and a northward shift of the nSEC and NECC.

Away from the equator, the largest surface velocity anomalies in the Pacific were observed in the Kuroshio region. Shifts in the location of the Kuroshio Jet are associated with a decadal stable/unstable oscillation (Qiu and Chen 2005). The Kuroshio shifts to the north when it intensifies and becomes stable, thus lowering eddy kinetic energy (EKE). Averaged in the downstream Kuroshio Jet region 141°–153°E, 32°–38°N (Qiu and Chen 2005), EKE was low in 1993–95, elevated in 1999–2001, low in 2002–04, high in 2005–08, and low in 2015–18 (not shown). EKE increased from 0.094 m^2 s^{-2} in 2018 to 0.129 m^2 s^{-2} in 2019, compared to the 1993–2019 average of 0.117 m^2 s^{-2}, while the annually averaged strength of the Kuroshio Jet decreased slightly but remained above its climatological mean. The location of the jet also remained north of its climatological mean, inconsistent with a phase shift of this decadal mode. Weakening of the Kuroshio and North Pacific Subtropical Gyre has been driven by the positive phase of the Atlantic Multidecadal Oscillation (AMO) since 1989/90 (Wu et al. 2019).

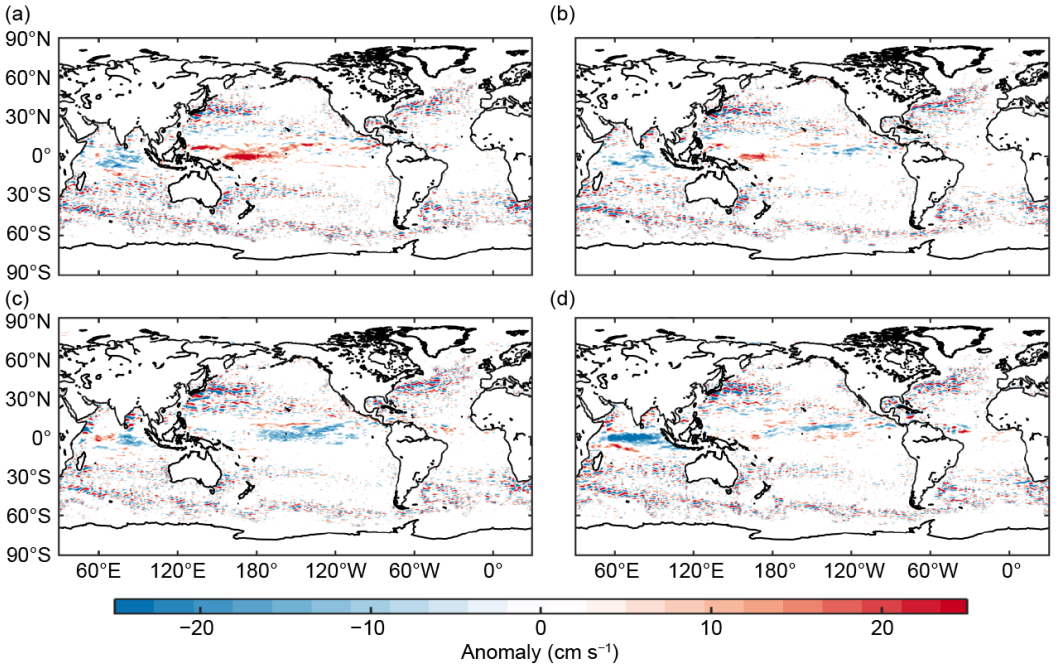

Fig. 3.18. Seasonally averaged zonal geostrophic anomalies with respect to seasonal climatology for (a) Dec–Feb 2018/19, (b) Mar–May 2019, (c) Jun–Aug 2019, and (d) Sep–Nov 2019. Values not shown where they are not significantly different from zero.

2) Indian Ocean

Annually averaged zonal currents in the Indian Ocean demonstrated 10–16 cm s^{-1} westward anomalies at 55°–95°E, 1°N–2°S, with weaker westward anomalies extending south to 10°S (Fig. 3.17a). Because 2018 was close to climatology, the 2019 – 2018 annual anomaly map (Fig. 3.17b) is dominated by the 2019 anomalies. These anomalies first developed in December–February 2018/19 (Fig. 3.18a) when they exceeded 5 cm s^{-1} from 1°N–9°S and reached 10 cm s^{-1} at 4°S. These westward anomalies persisted in March–May (Fig. 3.18b) with maximum anomalies of 10 cm s^{-1} westward on the equator and in June–August (Fig. 3.18c), with two maxima of 10–12 cm s^{-1} at 0°–1°S and 4°–5°S coinciding with the IOD reaching a its highest value in more than two decades (Figs. 3.2c,d). The westward anomalies dramatically increased in September–November (Fig. 3.18d), strengthening to exceed 10 cm s^{-1} at 2°N–5°S, and reached a dramatic 40 cm s^{-1} at 1°S; these anomalies led to the development of the intense east-to-west sea level anomaly gradient across the Indian Ocean basin (Fig. 3.15d). In this latitude band, where the Southwest Monsoon Current is 10–20 cm s–1 eastward in seasonal climatology, the total current was instead 20–30 cm s^{-1} westward.

3) Atlantic Ocean

Annual mean zonal currents in the tropical Atlantic Ocean were close to their climatological values in 2019 (Fig. 3.17a) and in each of the seasonal averages (Fig. 3.18).

Atlantic Ocean changes in baroclinic transport and in the location of several surface currents, and the mesoscale rings associated with them, are continuously monitored using satellite altimetry observations (www.aoml.noaa.gov/phod/altimetry/cvar/index.php). We summarize here the state of four key dynamic features in the Atlantic Ocean: 1) During 2019, satellite altimetry observations indicated that the number of rings shed by the Agulhas Current into the South Atlantic remained similar to the 1993–2019 mean of four to six rings per year. The transport by these rings, which represents a portion of the water mass exchange between the Indian and Atlantic Oceans, is thus expected to have remained unchanged. 2) In the southwest Atlantic Ocean, the separation of the Brazil Current front from the continental shelf break (located at 37.6°S in the mean) reveals the intrusion of subtropical waters into the subpolar region (c.f., Lumpkin and Garzoli 2010; Goni et al. 2011). In 1998, the annual mean latitude of this separation shifted abruptly southward and remained anomalously south afterward, apart from a one-year northward shift in 2016 (Fig. 3.19). In 2017 the separation latitude shifted south by 2° latitude to its most southward location in the altimeter time period (1993–present). In 2018–19, the separation latitude was slightly north of its 2017 location but remained well south of the 1993–2019 mean (Fig. 3.19). 3) The North Brazil Current, which transports waters from the South Atlantic into the North Atlantic basin, continued shedding a large number of rings (approximately six rings). These rings may eventually make their way into the Caribbean Sea, carrying with them fresh waters from the Amazon River; this fresh water creates barrier layers in the Caribbean Sea that often contribute to Atlantic hurricane intensification and may be associated with the fresh water anomalies seen here in late 2019 (Balaguru et al. 2012; see Fig. 3.8). 4) Altimetry-derived annual averaged transports of the Yucatan and Florida current for 2019 do not show significant deviation from their climatological annual means of 24–26 Sv and 28–30 Sv, respectively. Nearly all of the transport of the Florida Current enters

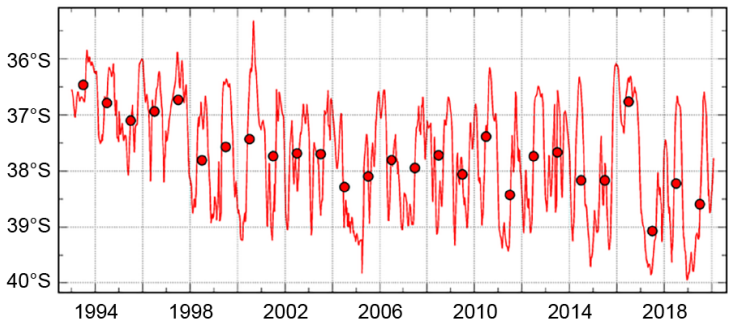

Fig. 3.19. Time series of the latitude of separation of the Brazil Current (BC) front from the continental shelf, defined as the intersection between the –1000-m bathymetry contour and the contour when the 10°C isotherm is 200 m deep. Solid red curve: 28-day running mean. Red dots: annual averages. The mean latitude of separation is 37.7°S ± 0.1°. (Source: www.aoml.noaa.gov/phod/altimetry/cvar/mal/BM_ts.php.)

the Gulf of Mexico via the Yucatan Channel, according to transport measurements at key locations including the Northwest Providence Channel (Candela et al. 2019). One recent study (Domingues et al. 2019) demonstrated that westward-propagating eddies play a key role in modulating the phase of the Florida Current transport interannual variability, but not its amplitude.

h. Atlantic meridional overturning circulation and associated heat transport—D. L. Volkov, C. S. Meinen, C. Schmid, B. Moat, M. Lankhorst, S. Dong, F. Li, W. Johns, S. Lozier, R. Perez, G. Goni, M. Kersalé, E. Frajka-Williams, M. Baringer, D. Smeed, D. Rayner, A. Sanchez-Franks, and U. Send

The Atlantic meridional overturning circulation (AMOC) is a key component of the ocean circulation system that is constantly moving water, heat, salt, carbon, nutrients, and other substances around the globe. The AMOC impacts the Atlantic Ocean in a unique way, making it the only ocean basin where heat is carried northward in both hemispheres. Recognizing the role of the AMOC in Earth's climate and, hence, the importance of monitoring and understanding it, several AMOC-observing systems have been established over the last two decades (e.g., Frajka-Williams et al. 2019; McCarthy et al. 2020; Fig. 3.20). This section describes the most recent findings derived from the existing observations of the volume (MOC) and the associated meridional heat transports (MHT). Because some of the key boundary current arrays have been observed for longer than the fully trans-basin arrays, key results on those boundary currents are also reviewed.

Due to the complexities of measuring meridional flows across an entire ocean basin, early observations of the MOC were generally done via direct and indirect calculations using data from trans-basin hydrographic cruises (e.g., Bryden et al. 2005; Lumpkin and Speer 2007; Dong et al. 2009). Continuous measurements of the overturning circulation began with systems measuring the western boundary components of the AMOC, such as the Florida Current (FC) at 27°N since 1982, part of the upper limb of the MOC (e.g., Meinen et al. 2010), and the Deep Western Boundary Current (DWBC) of the lower limb of the MOC at 53°N since 1997 (Zantopp et al. 2017) and at 16°N since 2000 (MOVE array; Send et al. 2011). Direct continuous fully trans-basin AMOC monitoring started in 2004, when the first-ever basin-wide array was established at approximately 26.5°N (now known as Rapid Climate Change/Meridional Overturning Circulation Heat-flux Array/Western Boundary Time Series [RAPID/MOCHA/WBTS] array; e.g., Smeed et al. 2018). Since then, continuous trans-basin AMOC observations have expanded to the South Atlantic, with the South AMOC Basin-wide Array (SAMBA) at 34.5°S since 2009 (Meinen et al. 2013, 2018), and the subpolar North Atlantic with the Overturning in the Subpolar North Atlantic Program (OSNAP) array since 2014 (Lozier et al. 2017, 2019). Significant efforts have also been made to obtain near-continuous estimates of the

Fig. 3.20. AMOC continuous observing arrays producing transport estimates today (black lines) or expected to produce data soon (dashed lines). Arrows represent a simple schematic of the upper (red) and lower (blue) limbs of the overturning circulation. The conventional deep water formation regions in the Greenland (GS) and Labrador (LS) Seas are shown by blue-shaded circles.

AMOC using combinations of satellite altimetry and in situ (mainly Argo and eXpendable Bathy-Thermographs [XBT]) data (e.g., Hobbs and Willis 2012; Dong et al. 2015; Majumder et al. 2016). Furthermore, new AMOC arrays have been developed based on long-term western boundary arrays at both 47°N (NOAC; e.g., Rhein et al. 2011; Mertens et al. 2014; Roessler et al. 2015) and 11°S (e.g., Schott et al. 2005; Hummels et al. 2015) and are expected to produce AMOC estimates soon. Note that the methodologies used to estimate the AMOC and boundary current transports are dictated by array design and instrumentation used and, therefore, differ from one array to another.

The Florida Current, a regional name for the Gulf Stream as it passes through the Florida Straits, carries the bulk of the northward upper-limb of the overturning transport in the subtropical North Atlantic. Its daily transport has been measured almost continuously since 1982 using a submarine cable between Florida and the Bahamas (e.g., Larsen and Sanford 1985; Baringer and Larsen 2001; Meinen et al. 2010), which makes it perhaps the longest climate record of a boundary current in existence. The record-length time-mean FC transport is 31.8 ± 0.4 Sv (henceforth the ± uncertainty shows 95% confidence limits for monthly averaged data) and the standard deviation of the monthly mean values is 2.5 Sv (Fig. 3.21a). Over the entire observational period, the FC transport has been rather stable with a statistically insignificant mean negative trend of −0.03 ± 0.04 Sv per year. In 2019, the annual mean FC transport was 30.2 ± 1.1 Sv, which is lower than the 32.4 ± 2.3 Sv observed in 2018 and the 31.7 ± 1.4 Sv observed in 2017 (but the differences are not significant based on the estimated uncertainties). Not all variations in the FC transport record are necessarily associated with variations in the overturning circulation. For example, the lower mean transport in 2019 was partly due to Hurricane Dorian passing over the Bahamas and along the U.S. southeast coast between 31 August and 6 September, causing a pronounced FC slowdown that helped to establish the new record minimum FC transport of 17.1 Sv on 4 September. Earlier studies have demonstrated that hurricanes passing over the Gulf Stream can dramatically reduce the flow of the current (e.g., Todd et al. 2018), and the previous record low was set during Hurricane Sandy on 28 October 2012 with a value of 17.2 Sv.

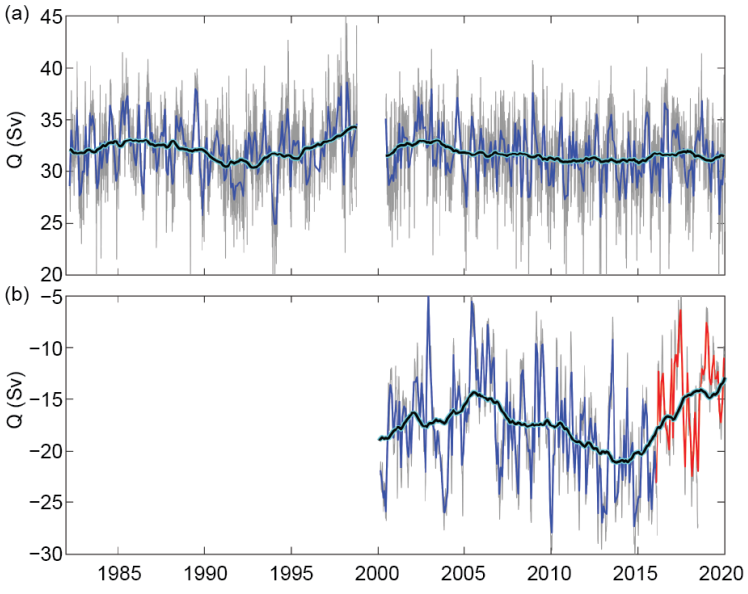

Fig. 3.21. Daily (gray) and monthly mean (blue and red) estimates of the volume transport of (a) the FC at 27°N (WBTS) and (b) the DWBC at 16°N (MOVE). Note, the period with remaining calibration issues for MOVE array after Feb 2016 is shown by red curve in panel (b). The black curves with cyan edges show the moving averages with a 3-year window, with the window size reduced at the endpoints.

The longest continuous observational record of the DWBC transport has been collected in the tropical western Atlantic by the MOVE array at about 16°N. At this location, the basin geometry is particularly well suited for monitoring the deep branch of the AMOC with a small number of moorings (currently three). The records have been updated to the end of 2019 (Fig. 3.21b), although there are still remaining issues with calibration after February 2016 (highlighted in red in Fig. 3.21b). Furthermore, records since mid-2018 are estimates based on the two western moorings only, because data from the eastern mooring have not yet been collected. For transport estimates, the eastern mooring data were kept constant using the average of the last six months of available data (the first half of 2018). The record-length time mean and the standard deviation of the monthly time series are −17.3 ± 1.4 Sv and 4.8 Sv, respectively. As documented in previous *State of the Climate* reports, the 16°N observations continue to demonstrate decadal-scale

variability (see the low-pass filtered time series in Fig. 3.21b). The years immediately prior to 2016 had stronger southward flow, and since then a weaker southward flow has been observed. In 2019, the southward flow was particularly weak, possibly suggesting a minimum value of the decadal variability. A similar swing from stronger to weaker southward flow occurred in the 2000–07 time frame (Send et al. 2011).

The RAPID/MOCHA/WBTS array at 26.5°N targets the latitude of the maximum northward heat transport in the North Atlantic. Presently, the array features 24 tall moorings and includes instruments for direct velocity measurements near the boundaries (e.g., Kanzow et al. 2007; McCarthy et al. 2015). The moorings in this array are recovered and redeployed every 18 months, and here we present the most up-to-date 12-hourly and monthly time series from April 2004 to September 2018 (Fig. 3.22b; Smeed et al. 2019). The record-length time-mean MOC at 26.5°N is 17.7 ± 0.9 Sv, with a monthly standard deviation of 3.5 Sv. There is a substantial seasonal variability with amplitudes of 2 Sv and 0.7 Sv for the annual and semi-annual harmonics, respectively. The interannual variability is larger and has a peak-to-peak range of about 6 Sv. The MHT at 26.5°N is strongly correlated with the MOC (r = 0.96), which means that velocity variations dominate over temperature variations. The time-mean MHT is 1.2 ± 0.1 PW (1 PW = 10^{15} W), which constitutes about two-thirds and one-quarter of the total oceanic and atmospheric MHT, respectively (e.g., Trenberth and Fasulo 2017). From 2004–08 to 2008–12 the MOC and MHT at 26.5°N reduced from 18.8 to 15.9 Sv and from 1.3 to 1.1. PW, respectively (significantly different from zero at 95% confidence; Smeed et al. 2018), and they have remained in a low state compared to the prior period. The latest results (through 2018) conclude that while the MOC at 26.5°N has been increasing since 2009 at a rate of 0.3 ± 0.3 Sv per year, this trend is not statistically significant (Moat et al. 2019, 2020). One of the main discoveries made possible by the continuous MOC monitoring at 26.5°N is that the largest variability is concentrated at sub-annual frequencies (periods from 10 days to months) with a peak-to-peak amplitude exceeding 30 Sv. This indicates that infrequent quasi-synoptic measurements (e.g., snapshots from ship transects) cannot accurately capture the low-frequency variability or establish the annual mean transport, for which continuous monitoring is required.

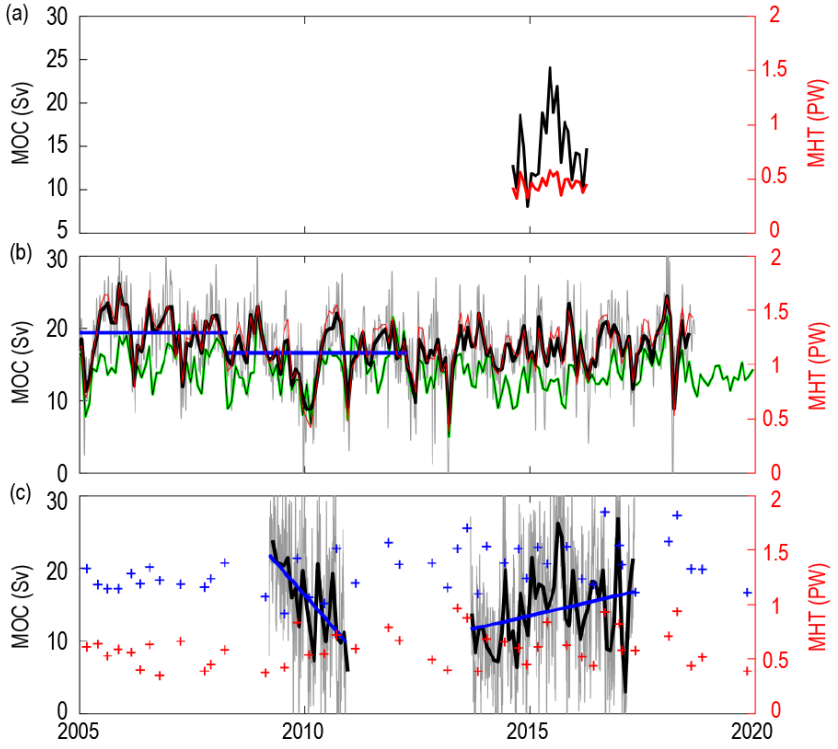

Fig. 3.22. Estimates of the northward MOC and MHT transports: (a) across OSNAP array, (b) at 26.5°N, and (c) at 34.5°S. Gray curves show 12-hourly values for RAPID/MOCHA/WBTS in (b) and daily values for SAMBA in (c); black curves show MOC monthly values. The blue lines show averages during 2004–08 and 2008–12 in panel (b) and linear trends in 2009–10 and 2013–17 in panel (c). MHT estimates are shown by red curves for OSNAP and RAPID/MOCHA/WBTS arrays. The green curve in (b) shows the MOC estimate at 26.5°N from the combination of altimetry and Argo data. The blue/red crosses in (c) show MOC/MHT estimates obtained from XBT data along AX18 transect in the South Atlantic.

The MOC anomalies observed in the North Atlantic can either be of a local origin or originate upstream in the South Atlantic and beyond, in the Southern and Indian Oceans. It has been suggested that freshwater flux into the South Atlantic may control the stability of the entire AMOC system (e.g., Rahmstorf 1996;

Dijkstra 2007; Drijfhout et al. 2011; Garzoli et al. 2013; Weijer et al. 2019). To monitor the impact of inter-ocean exchanges on the AMOC, the SAMBA moorings at 34.5°S began being deployed in 2009 (e.g., Meinen et al. 2013; Ansorge et al. 2014). Similar to what has been found at 26.5°N, the SAMBA results have demonstrated that continuous measurements are imperative to resolve the annual mean and to avoid aliasing high-frequency signals. Currently, the array includes 20 moorings at 34.5°S consisting mostly of pressure-equipped inverted echo sounders (PIES); many of them are also equipped with a near-bottom current meter (CPIES). The available MOC time series at SAMBA is daily and spans the period March 2009–April 2017 (more recent data have not been recovered yet), with a data gap during December 2010–September 2013 (Fig. 3.22c). The record-length time-mean northward transport is 14.7 Sv, and the monthly standard deviation is 5.3 Sv, which is larger than the standard deviation observed at 26.5°N and is consistent with previous results showing that the MOC variability decreases northward (Dong et al. 2015; Majumder et al. 2016; Frajka-Williams et al. 2019). Measurements from SAMBA have revealed that the MOC has strong independent barotropic (pressure-driven), baroclinic (density-driven), and Ekman (wind-driven) variations at 34.5°S at a wide range of time scales from a few days to seasonal and interannual (Meinen et al. 2018). Seasonal variations are significantly influenced by both baroclinic and barotropic variations near the boundaries, with the strongest contributions coming from the density variations near the eastern boundary. The Ekman and barotropic seasonal anomalies nearly balance one another, so the total MOC seasonality varies nearly in phase with the seasonality of the baroclinic contribution (Meinen et al. 2018). Interannual variations of the MOC at 34.5°S are primarily driven by baroclinic and barotropic variations, with the Ekman contributions being quite weak in comparison (Meinen et al. 2018). Although the MOC appears to be strengthening in 2013–17 at a rate of 1.4 ± 1.9 Sv per year (blue line in Fig. 3.22c), this change is not statistically significant.

It is also important to monitor the AMOC in the proximity of key regions of deep water formation and thus provide direct assessments of the relationships that have been suggested in past modeling studies (Biastoch et al. 2008; Zhang 2010; Yeager and Danabasoglu 2014). These assessments are particularly important in light of dramatic climate changes in the Arctic, including large increases in air and sea temperatures, Greenland glacier melt, and extensive sea ice reduction. The OSNAP array, started in 2014 to make these important measurements (Lozier et al. 2017), consists of 57 moorings supplemented with glider and float measurements along two legs: one extending from southern Labrador to the southwestern tip of Greenland across the mouth of the Labrador Sea (OSNAP West; ~52°–60°N), and the second extending from the southeastern tip of Greenland to Scotland (OSNAP East; ~57°–60°N) (Fig. 3.22a). As of today, the data records span a nearly four-year period from 2014 to 2018, with published estimates of the MOC and MHT being available for the initial 21-month period of the array from August 2014 to April 2016. The MOC across the entire OSNAP section has the time-mean of 14.9 ± 1.8 Sv and shows considerable temporal variability, with 30-day means ranging from 8.1 to 24.1 Sv and a standard deviation of 4.1 Sv (Lozier et al. 2019). One of the main findings over the observational period is that the conversion of warm, salty, shallow Atlantic waters into cold, fresh, deep overflow waters moving southward in the Irminger and Iceland basins is largely responsible for the bulk of the overturning and its variability in the subpolar basin. This result challenges the dominant view that changes in deep water formation in the Labrador Sea dominate the AMOC variability (Lozier et al. 2019). The time-mean MHT across the entire OSNAP is 0.45 ± 0.04 PW with a standard deviation of 0.08 PW. Similar to 26.5°N, the MHT and MOC are strongly correlated (r = 0.9). Therefore, the MHT is principally accomplished by the overturning, which is dominated by flows across OSNAP East. Weak overturning in the Labrador Sea during 2014–16 can be explained by strong density compensation of salinity and temperature transformation in that basin (Zou et al. 2020a). Another interesting result is that RAFOS floats entering the western subpolar gyre as they exit the Charlie Gibbs Fracture Zone do not

show a dominant pathway northward into the Irminger basin, in contradiction to the traditional view of the way the overflow water spreads (Zou et al. 2020b).

Existing time series of the AMOC transports from trans-basin in situ observing arrays are limited in both number and temporal extent due to the cost of maintaining such arrays. So other methods for estimating the AMOC transports still have important roles to play. The long-term observations from XBT ship sections, including the high-density AX18 XBT transect near 34.5°S, represent some of the longest in situ time series, in the case of AX18 dating back to 2002 (e.g., Dong et al. 2009; Garzoli et al. 2013). Another strength of the XBT transects is that they have high horizontal-resolution information about upper ocean temperatures in the ocean, making them extremely useful for calculating MHT. The time-means of MOC and MHT across AX18 since 2002 are 19.9 ± 0.8 Sv and 0.6 ± 0.1 PW, respectively, and the standard deviations are 3.1 Sv and 0.2 PW (blue and red crosses in Fig. 3.22c). The correlation between the MOC and MHT from AX18 is 0.78. In 2019, there was only one occupation of AX18 yielding MOC and MHT estimates of 16.7 Sv and 0.4 PW, respectively.

Other newer methods for calculating the MOC using blended in situ and satellite observations have also been producing interesting results. Methods combining altimetry (available since 1992) and Argo profiling floats (good spatial coverage since 2004) help in advancing the understanding of the latitudinal connectivity of the MOC system. Willis (2010) and Hobbs and Willis (2012) first combined altimeter-derived surface geostrophic velocities with the Argo-measured temperature and salinity profiles as well as float-drift velocities at 1000-m depth to estimate the MOC/MHT at 41°N. This time series has not been updated since the 2017 *State of the Climate* report. Similar blended MOC/MHT estimates based on satellite altimetry and in situ data (XBT, Argo, CTD) covering the period 1993–2020 have recently been obtained for 26.5°N in the North Atlantic, taking into account the FC transport measured by the cable (Fig. 3.22b; McCarthy et al. 2020), and for several latitudes in the South Atlantic between 20° and 35°S (Schmid 2014; Dong et al. 2015; Majumder et al. 2016). The 1993–2019 mean MOC at 26.5°N from the blended product is 14.1 ± 0.4 Sv, which is lower than the time-mean MOC measured by the RAPID/MOCHA/WBTS array. Nevertheless, the variability is reproduced reasonably well, with the exception that the blended product does not reproduce the higher-than-average MOC state in 2004–09 observed by moorings (Fig. 3.22b). The blended product at 26.5°N also shows that the annual mean MOC in 2019 was 13.5 ± 0.8 Sv, i.e., not statistically different from the full record mean. Comparison of the XBT-based and various blended satellite/in situ estimates at 34.5°S (updated from Schmid 2014; Dong et al. 2009, 2015; Majumder et al. 2016) with the SAMBA continuous time series, and with one another, generally yields low correlation values (not shown). On one hand, this can be expected given the differing temporal resolution of the observations in the face of the strong high-frequency variability measured by moored arrays. On the other hand, this suggests that these blended estimates are sensitive to the methodology used to derive them. Reconciling the different estimates made by the multiple AMOC estimation techniques in use today represents an area for ongoing research.

i. Global ocean phytoplankton—B. A. Franz, I. Cetinić, J.P. Scott, D. A. Siegel, and T.K. Westberry

Photosynthetic production of carbon-containing compounds by marine phytoplankton fuels oceanic ecosystems and drives biogeochemical cycles (e.g. Falkowski et al. 1998; Field et al. 1998), contributing roughly 50% to global net primary production (NPP). Phytoplankton distribution, growth, and diversity are governed by light and nutrient availability, successively controlled by physical conditions (e.g., Behrenfeld et al. 2006). Spaceborne radiometers such as SeaWiFS (McClain 2009) and MODIS (Esaias et al. 1998) allow detection of spatio-temporal changes in the distribution of phytoplankton, either through near-surface concentration of the phytoplankton pigment chlorophyll-*a* (Chl*a*; mg m^{-3}) or phytoplankton carbon (C_{phy}, mg m^{-3}). Both parameters are useful tools to quantify variability of phytoplankton biomass in the ocean; discrepancies between their distributions (shifts in Chl*a*:C_{phy} ratios) are indicators of physiological variability

within the cell (due to the changes in light and nutrient conditions) or changes in species composition (Westberry et al. 2016; Dierssen 2010; Geider et al. 1997). The combination of these two measurements thus provides a synoptic view of phytoplankton biomass in the ocean as well as its response to climate-associated variability in the environment.

In this report, we evaluate global Chl*a* and C_{phy} distributions for the one-year period from October 2018 through September 2019, within the context of the continuous 22-year record provided through the combined observations of SeaWiFS (1997–2010) and MODIS on *Aqua* (MODIS-A, 2002–present). The MODIS-A daytime sea surface temperature (SST; °C) is also assessed for the same period to provide context on the physical state of the oceans. The Chl*a* product was derived using the ocean color index (OCI) algorithm of Hu et al. (2012), while C_{phy} was derived from the particle backscattering coefficient, b_{bp}, at 443 nm (GIOP algorithm, Werdell et al. 2013) and a linear relationship between b_{bp} and C_{phy} as described in Graff et al. (2015). In combining the ocean color records, the overlapping period from 2003 through 2010 was used to assess and correct for residual bias between the two mission datasets.

Changes in phytoplankton distribution over the year were evaluated by subtracting monthly climatological means for MODIS-A (October 2002–September 2018) from the mean values for MODIS-A Chl*a* and C_{phy} in each month of the year. These monthly fields were then averaged to produce the global Chl*a* and C_{phy} anomaly maps for 2019 (Figs. 3.23a,b). Similar calculations were performed on MODIS-A SST data to produce an equivalent SST annual mean anomaly for the same time period (Fig. 3.23c). The permanently stratified ocean (PSO) is defined as the region, spanning the tropical and subtropical oceans, where annual average SST is greater than 15°C and surface mixed layers are typically low in nutrients and shallower than the nutricline (black lines near 40°N and 40°S in Fig. 3.23; Behrenfeld et al. 2006).

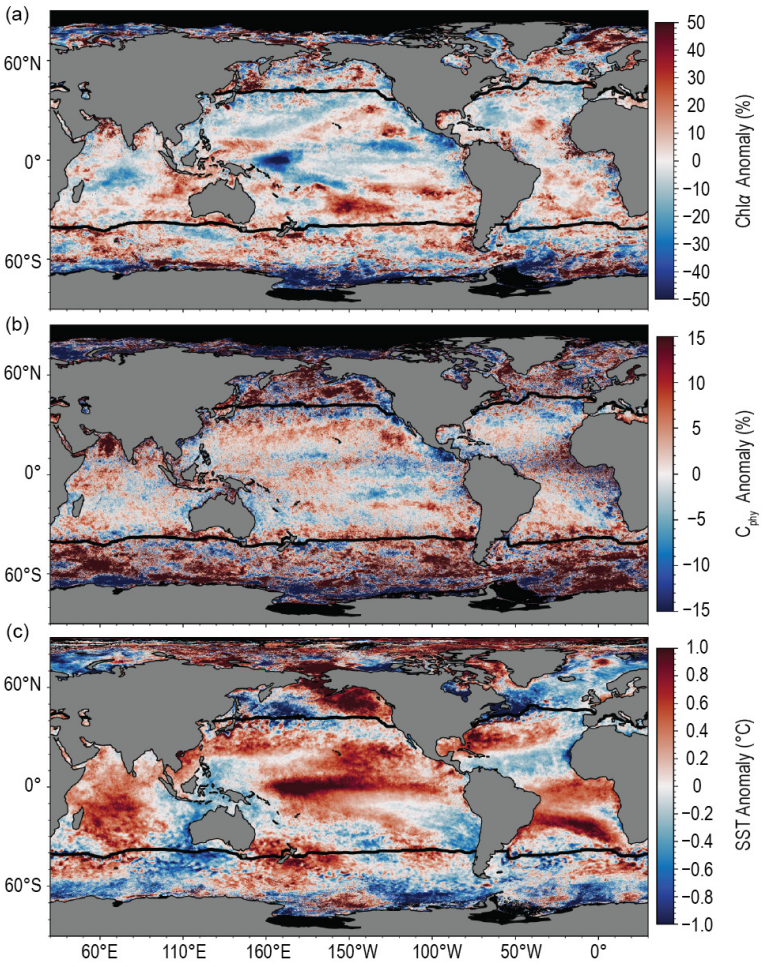

Fig. 3.23. Spatial distribution of average monthly (a) MODIS-A Chl*a* anomalies, (b) MODIS-A C_{phy} anomalies, and (c) MODIS-A SST anomalies, where monthly differences were derived relative to a MODIS-A 16-year climatological record (Oct 2002–Sep 2018). Chl*a* and C_{phy} are stated as % difference from climatology, while SST is shown as an absolute difference. Also shown in each panel is the location of the mean 15°C SST isotherm (black lines) delineating the PSO.

Chl*a* concentrations for 2019 (Fig. 3.23a) were suppressed 10%–30% relative to the climatological mean (0.142 mg m^{-3}) in the western Pacific warm pool, northern region of the tropical Pacific, western North Pacific, and central Indian Ocean. These locations correspond to regions of strongly elevated SSTs (Fig. 3.23c). Positive SST anomalies in these permanently stratified ocean regions generally coincide with shallower surface mixed layer depths (MLD), which increases light exposure within the mixed layer. Response of the phytoplankton to this increased insolation manifests as a decrease in cellular chlorophyll concentrations (Behrenfeld et al. 2015). This effect, in combination with the physiological response to low nutrient conditions, leads to decreased

cellular chlorophyll to carbon ratios (Westberry et al. 2016) and thus a decoupling of the Chl*a* and C_{phy} anomalies. Like Chl*a*, concentrations of C_{phy} within the tropical Pacific show similar but weaker patterns of negative anomalies in the east (–5%) but contrasting neutral to positive anomalies (+5%) in the west compared to the 22-year average (23.7 mg m^{-3}), with C_{phy} anomalies generally more homogeneous across the Atlantic and Pacific Oceans (Fig. 3.23b), consistent with prior-year observations (Franz et al. 2019). Notably, a region of strongly elevated SST in the South Atlantic, extending from the east coast of South America to the Horn of Africa (Fig. 3.23c), shows neutral to positive Chl*a* anomalies and neutral to negative C_{phy} anomalies. Elevated phytoplankton biomass, evident from both Chl*a* and C_{phy} anomalies, were visible in the Mediterranean Sea, Arabian Sea, and Bay of Bengal, and the southern Pacific subtropical gyre. Outside of the PSO, a much weaker correlation is generally observed between phytoplankton biomass anomalies and SST anomalies, consistent with past reports (e.g., Franz et al. 2019), with patches of high biomass visible throughout the Southern Ocean and northern subpolar Atlantic (negative SST anomaly) and the northeastern subpolar Pacific (positive SST anomaly).

Seasonal changes in phytoplankton biomass in the PSO typically display two pronounced peaks, reflecting vernal increases in biomass in the Northern Hemisphere (NH) and Southern Hemisphere (SH; Fig. 3.24). Peaks in monthly climatological C_{phy} tend to trail behind peaks in Chl*a* with a two-month delay, likely due to a reduction in phytoplankton chlorophyll to carbon ratios as the seasonal bloom progresses (e.g., Westberry et al. 2016). During 2019, primary and

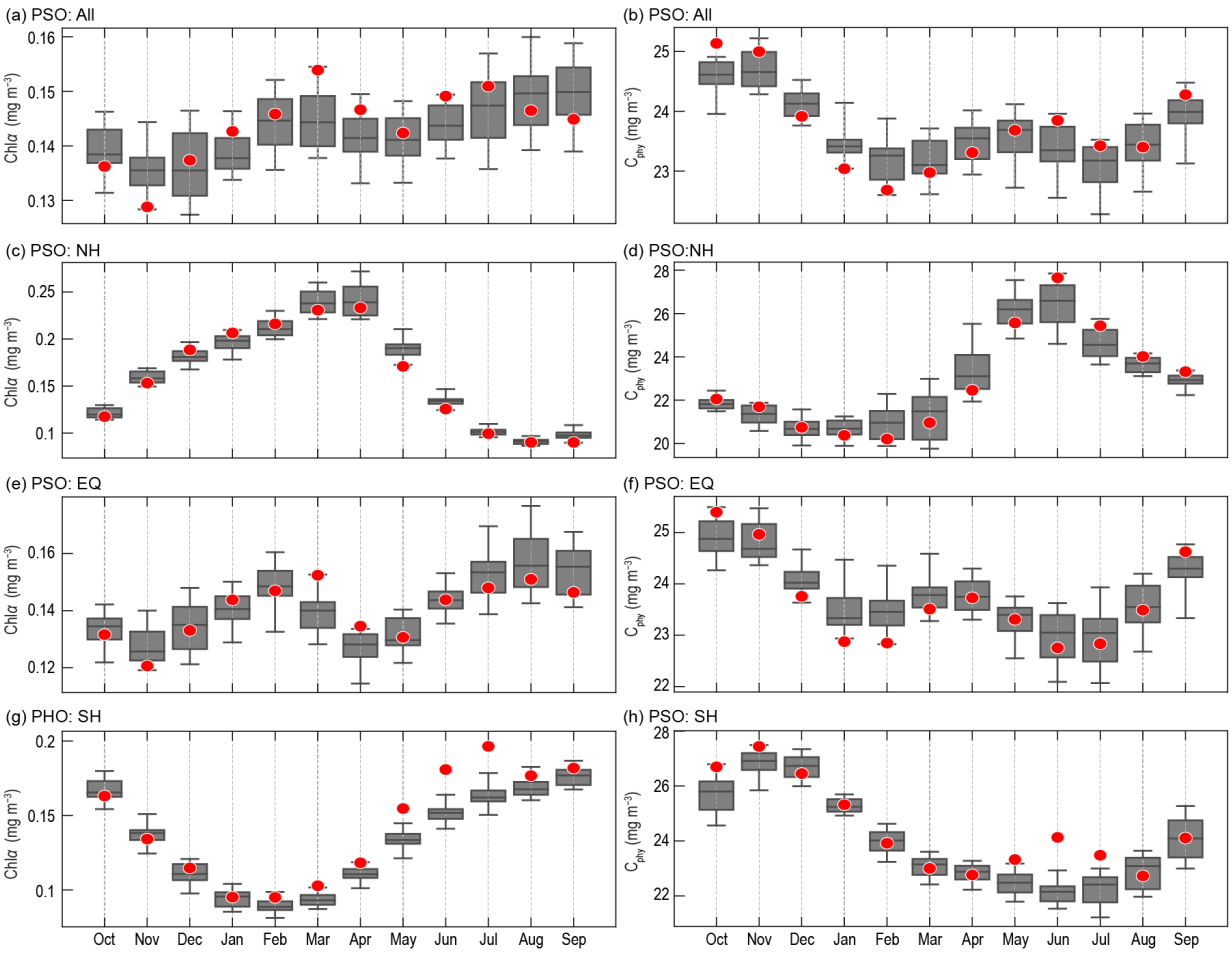

Fig. 3.24. Distribution of Oct 2018–Sep 2019 monthly means (red circles) for (a) MODIS-A Chl*a* and (b) MODIS-A C_{phy} for the PSO region, superimposed on the climatological values as derived from the combined time series of SeaWiFS and MODIS-A over the 20-year period 1998–2017. The gray boxes show the interquartile range of the climatology, with a black line for the median value and whiskers extending to the 5th and 95th percentiles. Subsequent panels show latitudinally segregated subsets of the PSO for the NH north of 23°N (c),(d), tropical ±23.5° latitude subregion (e),(f), and SH south of 23°S (g),(h).

secondary peaks in Chl*a* (Fig. 3.24a) occurred in March and July, followed by C_{phy} maxima in June and October (Fig. 3.24b), corresponding with the associated seasonal cycles of the NH and SH, respectively (Figs. 3.24c–h), and with timing consistent with prior-year observations (Franz et al. 2019). Monthly mean values of Chl*a* and C_{phy} for 2019 fell generally within the range of climatological norms, with the notable exception of highly elevated concentrations observed in the SH in May–July.

Over the 22-year time series of spatially integrated monthly mean Chl*a* within the PSO (Fig. 3.25a), concentrations varied by ~15% (±0.02 mg m^{-3}) around a long-term average of 0.142 mg m^{-3} (Fig. 3.25a). This variability includes significant seasonal cycles in Chl*a* distributions and responses to climatic events, as has been observed previously (e.g., Behrenfeld et al. 2006; Franz et al. 2019). C_{phy} over the same 22-year period varied by ~7% (±1.5 mg m^{-3}) around an average of 23.7 mg m^{-3} (Fig. 3.25c). The October 2018–September 2019 monthly anomalies varied by ±2% around that average (Fig. 3.25d), consistent with neutral ENSO conditions. Seasonal cycles in C_{phy} are more clearly defined than those of Chl*a*, consistent with the assertion that C_{phy} represents true variability in phytoplankton biomass that is insensitive to local and global environmental conditions that alter cell pigmentation through physiological processes.

Chl*a* monthly anomalies within the PSO (Fig. 3.25b) show variations of ±10% (±0.015 mg m^{-3}) over the multi-mission time series, with largest deviations generally associated with ENSO events. This link between ENSO variability and mean Chl*a* response in the PSO is demonstrated by the correspondence of anomaly trends with the Multivariate ENSO Index (MEI; Wolter and Timlin 1998), presented in the inverse to illustrate the covariation. For 2019, variability in monthly Chl*a* anomalies was modest (±6%) and centered around zero, consistent with neutral to weak ENSO conditions during this year (Fig 3.1b). Similar observations can be made of the C_{phy} anomalies (±2%), which also track well with the MEI over the 22-year timeseries.

Observed trends and variability in C_{phy} reflect changes in phytoplankton biomass, while Chl*a* variability reflects changes in both biomass and physiology (or health). These two properties are mechanistically linked to physical conditions of the upper ocean, as well as to ecological interactions between phytoplankton and their zooplankton predators. Our ability to track subtle variations in the distribution of Chl*a* and C_{phy} on the global scale thus contributes to our understanding of climate-driven changes in the functionality of the ocean. Unraveling the diversity

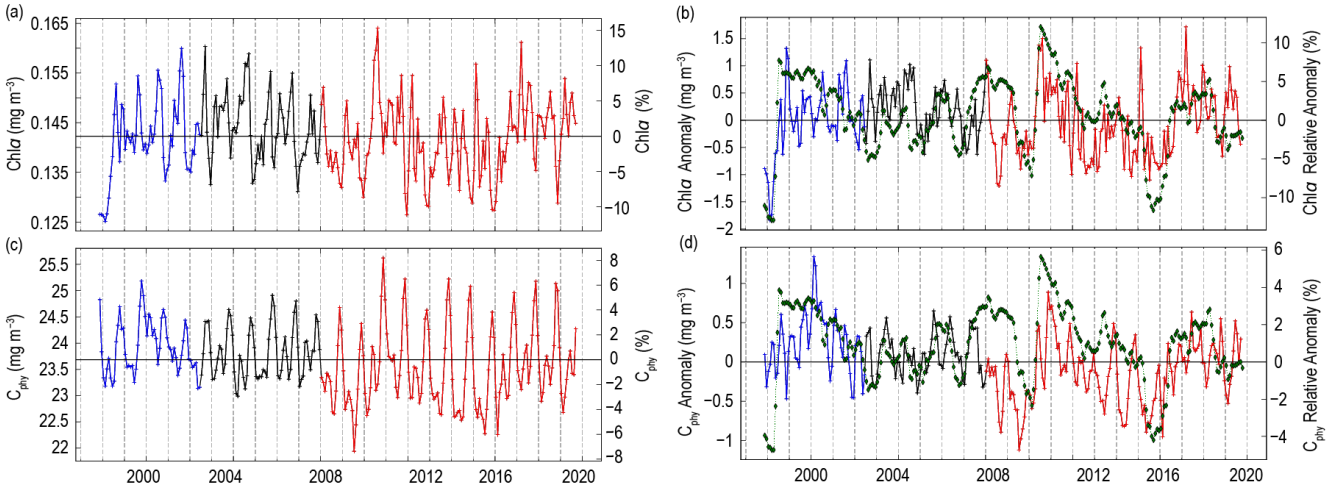

Fig. 3.25. The 22-year, multi-mission record of Chl*a* and C_{phy} averaged over the PSO for SeaWiFS (blue), MODIS-A (red), and combined (black). (a) Shows Chl*a* from each mission, with the horizontal line indicating the multi-mission mean Chl*a* concentration for the region. (b) Shows the monthly Chl*a* anomaly from SeaWiFS and MODIS-A after subtraction of the 20-year multi-mission climatological mean (Fig. 3.24). Both (c) and (d) show the same as (a) and (b), respectively, but for C_{phy}. Green diamonds show the MEI, inverted and scaled to match the range of the Chl*a* and C_{phy} anomalies.

and covariation of factors that influence Chl*a* concentrations, however, is essential for correctly interpreting the implications of Chl*a* anomalies on ocean biogeochemistry and food webs. An additional complication is that measured changes in ocean color often contain a contribution from chromophoric dissolved organic matter (Siegel et al. 2005) or from the changing phytoplankton population (with its type-specific optical characteristics; Dierssen 2010) that can be mistakenly attributed to changes in Chl*a* (Siegel et al. 2013). C_{phy} provides a more direct measurement of phytoplankton biomass and thus offers complementary information on the state of the oceans. Future satellite missions, such as the upcoming hyperspectral Plankton, Aerosol, Cloud, ocean Ecosystem mission (PACE), will enable the rigorous separation of phytoplankton absorption features from non-algal features, as well as the assessment of changes in phytoplankton species or functional group distributions (Werdell et al. 2019). Such data will provide a major step forward in our ability to disentangle the impacts of climate forcing on global phytoplankton communities.

Sidebar 3.1: **BioGeoChemical Argo**—K. S. JOHNSON, M. B. BIF, S. M. BUSHINSKY, A. J. FASSBENDER, AND Y. TAKESHITA

As atmospheric CO_2 rises, the ocean warms, winds shift, and ice melts (IPCC 2019). Numerical models suggest that large changes in ocean chemistry and biology will result (Beaugrand et al. 2019; IPCC 2019). Traditionally, the biogeochemical (BGC) measurements used to identify such changes have been made from research vessels, particularly for the ocean interior, which is not accessible by satellite remote sensing and not sampled by voluntary observing ships. However, the number of basic BGC properties observed from ships has been steadily declining over the past three decades as science objectives have changed (Boyer et al. 2013; Johnson et al. 2015), making it more difficult to observe these ocean changes in this critical moment.

Declining trends in the number of ship-based temperature and salinity observations have been mitigated through the global profiling float array established by the Core-Argo program (Riser et al. 2016). The BGC-Argo array of profiling floats is beginning a similar revolution for BGC processes (Johnson and Claustre 2016; Claustre et al. 2020). The accuracy and stability of the BGC sensor observations from profiling floats have been demonstrated by recent studies (Johnson et al. 2017; Mignot et al. 2019), and an implementation plan for a global array of 1000 BGC-floats has been developed by the Biogeochemical-Argo Planning Group (BAPG 2016; Roemmich et al. 2019). The remainder of this sidebar focuses on two of the longer-term records from BGC-Argo profiling floats to illustrate the applicability of such datasets in climate related studies.

North Pacific nitrate

Primary production in the sub-Arctic northeast Pacific Ocean mainly takes place during spring and summer months, fueled by vertical nutrient inputs from previous wintertime mixing events as well as increasing seasonal light levels (Wong et al. 2002). This region is directly affected by climate processes, such as El Niño–Southern Oscillation (ENSO) and the Pacific Decadal Oscillation (PDO). These events lead to changing heat content and stratification of the upper ocean (Wong et al. 2007; Bond et al. 2015), which alters the seasonal vertical nutrient exchanges (Bif et al. 2019). BGC-Argo profiling floats equipped with nitrate sensors have been deployed since 2008 at Ocean Station Papa (OSP; 50°N, 145°W), one of the oldest ocean time-series monitoring programs still in operation. These floats record annual cycles of net community production (NCP) based on seasonal nitrate depletion (Plant et al. 2016).

A significant warm anomaly developed in the region beginning in 2013 (Bond et al. 2015) and was intensified by an extreme El Niño in 2015 (Bif et al. 2019). Changes in physical and chemical properties before, during, and after the warm event were recorded by the BGC floats near OSP (Fig. SB3.1).

Float observations revealed that the potential density anomaly of 25.5 kg m^{-3} did not reach the surface during the warm years of 2013–15 as usually happens (Bif and Hansell 2019; Bif et al. 2019; Fig. SB3.1). Enhanced stratification restricted vertical mixing between the upper ocean and the deeper, nutrient-enriched

waters, resulting in anomalously low nitrate concentrations in the upper ocean (Fig. SB3.1). NCP computed from the nitrate record shows unusually low values in 2015 (Bif et al. 2019) that led to an unprecedented ecosystem response including shifts in plankton community composition (Peterson et al. 2017), impacts on fisheries (Richerson and Holland 2017), and large-scale mortality in seabirds (Piatt et al. 2020).

Similar warming conditions in the region since September 2018 can be clearly seen in the most recent data (Fig. SB3.1). The extended time series shows persistent winter stratification in 2018/19 and 2019/20 and reduced surface nitrate concentrations. As the ongoing warm event continues to evolve in 2020, one can only wonder if organic carbon production in the upcoming spring and summer months will respond as previously observed.

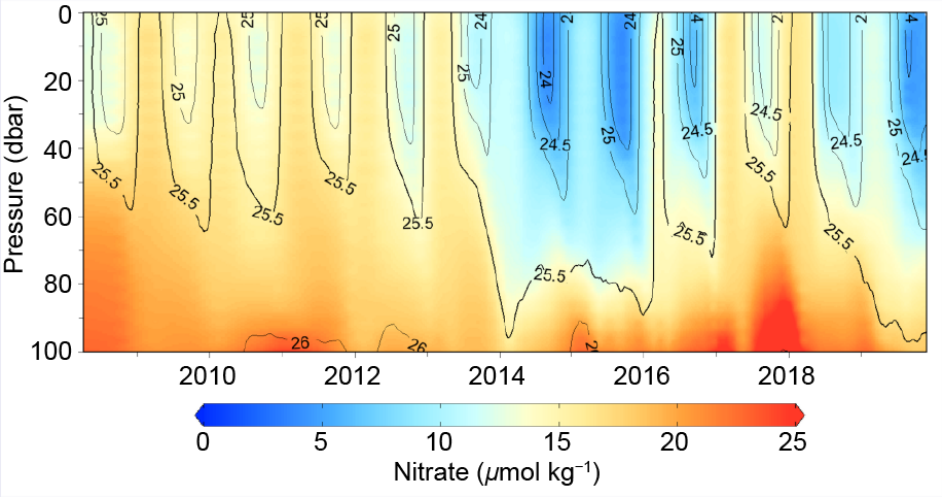

Fig. SB3.1. Nitrate concentrations (μmol kg^{-1}) in the upper 100 m measured since 2008 by BGC-Argo profiling floats launched at Ocean Station Papa (48°–54°N, 135°–152°W) in the North Pacific. Contours show the density anomaly (sigma theta, kg m^{-3}). Data were collected with 5-m vertical resolution every 5 days, with the exception of a gap from 27 Mar 2018 to 16 Aug 2018 that was filled by contouring. Updated from Fig. 9 in Bif and Hansell (2019).

Southern Ocean oxygen

Significant oxygen concentration decreases have occurred in the world ocean (Oschlies et al. 2018; Breitburg et al. 2018) and continued decreases are "very likely" (IPCC 2019). Some of the largest oxygen declines in the mesopelagic zone (200–1000 m below the surface) of the open ocean have occurred in the Southern Ocean (Helm et al. 2011). However, this region is not well sampled from ships. BGC-Argo profiling floats can produce the high-quality measurements needed to fill this gap.

Initial deployments of BGC-Argo floats equipped with oxygen sensors began in 2002 (Riser and Johnson 2008). These early data demonstrated the need for systematic corrections to oxygen data that result from calibration errors (Emerson and Bushinsky 2014; Bittig and Körtzinger 2015). Protocols to correct the early data using ocean climatologies were developed (Takeshita et al. 2013; Drucker and Riser 2016). Starting in 2014, the Southern Ocean Carbon and Climate Observations and Modeling program has deployed BGC-Argo floats that use atmospheric oxygen as an absolute in situ calibration, i.e., independent of ocean climatologies (Johnson et al. 2015; Bittig and Körtzinger 2015; Bushinsky et al. 2016). These developments allowed the first direct estimate of the Southern Ocean annual air–sea oxygen flux (Bushinsky et al. 2017) and revealed a much larger transfer of oxygen to the Southern Ocean than was previously estimated (Gruber et al. 2001). This is significant because the Southern Ocean represents one of the main ventilation pathways for the global interior ocean.

The float oxygen record defines clear seasonal cycles throughout Southern Ocean surface waters (not shown). Here we update the float oxygen record published in Bushinsky et al. (2017) for the Polar Frontal Zone (PFZ; Fig. SB3.2). Monthly mean oxygen values are displayed when mean float-determined sea surface temperatures (SSTs) agree with the NOAA Optimal Interpolation record. This was done to remove variance due to under-sampling. From records such as these, we can now determine an annual mean value and the associated variance at the surface and in the subsurface. Here we have shown the lightest layer of water that does not seasonally outcrop in the PFZ (Fig. SB3.2), but such results can be obtained down to 2000-m depth. Understanding the statistical variability in ocean oxygen is the first step in using the data to understand possible change linked to climate variation. Comparable assessments of oxygen variability are much more difficult to obtain from ships. Such observations are essential for quantifying interior ocean oxygen declines over time and the mechanisms that might drive any change (Bronselaer et al. 2020).

Conclusions

BGC sensors on profiling floats can now provide the high-quality and long-term observations needed to detect climate signals in the ocean; however, the current system is based on a framework of independent science experiments and operates with only a small fraction of the desired number of floats (BAPG 2016). A fully realized system would be transformative. As with Core-Argo salinity measurements, a reference database of deep (1000–2000 m) measurements is required to correct BGC pH and nitrate sensors for offsets or drifts (Johnson et al. 2017). Research programs that can accommodate float deployments will be essential partners to BGC-Argo. Programs such as GO-SHIP (Talley et al. 2016), which provide high-quality BGC observations in the deep sea, will become even more valuable as they provide the data needed to validate a distributed network of sensor observations.

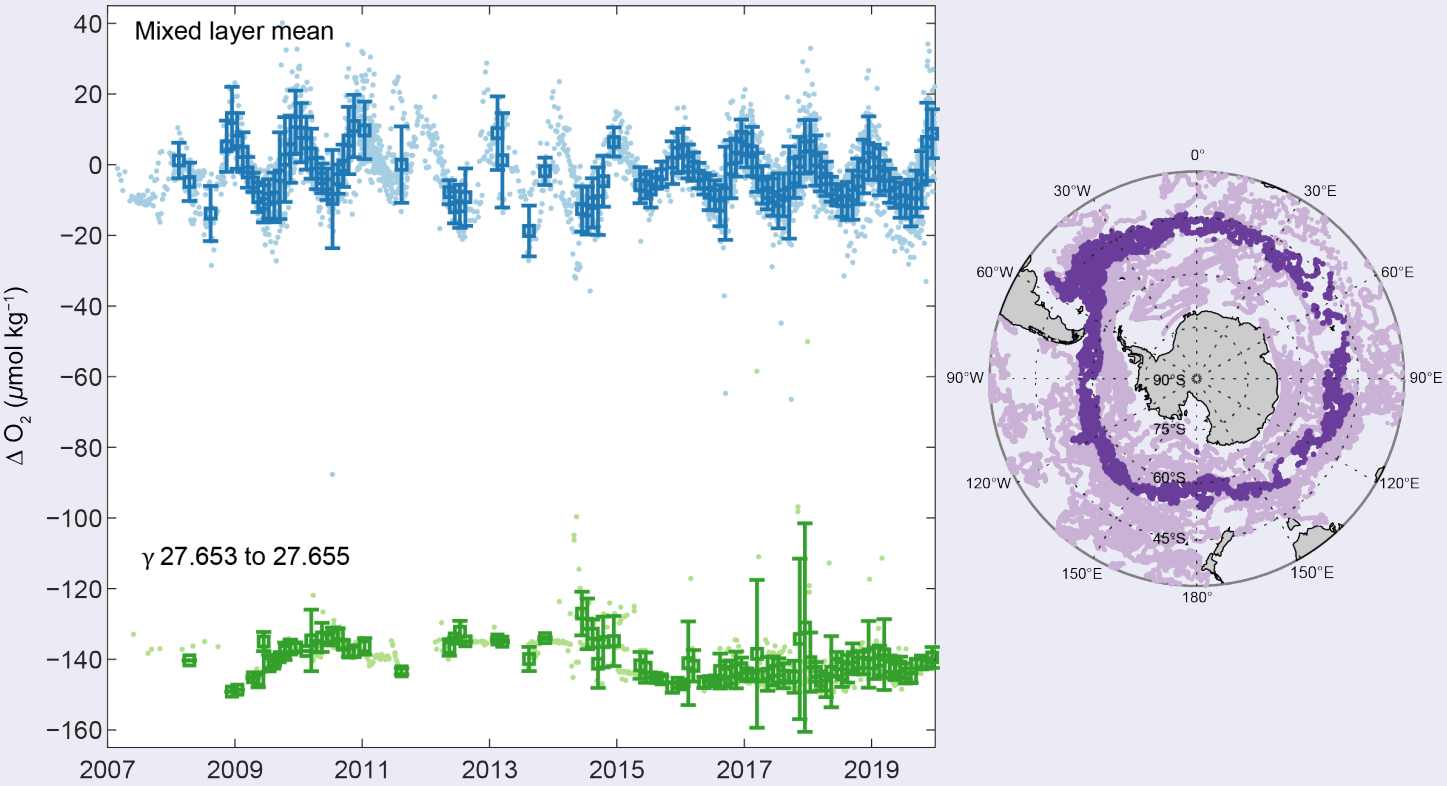

Fig. SB3.2. Time series of ΔO_2 ($[O_2] - [O_2]_{sat}$) for the Polar Frontal Zone of the Southern Ocean. Blue dots represent individual float profile mixed layer mean values and blue boxes with error bars represent monthly mean values ± 1 std. dev. Green dots and boxes are profile and monthly means for samples between neutral density (γ) surfaces 27.653 and 27.655, which represent the lightest waters for this zone that do not outcrop seasonally. Inset map indicates the spatial distribution of surface samples from the Polar Frontal Zone (dark purple) and the entire Southern Ocean (light purple) for 2002–19. Monthly values are only shown for months where mean float temperatures agreed with NOAA Optimal Interpolation SSTs (see Bushinsky et al. 2017 for more detail).

j. Global ocean carbon cycle—R. A. Feely, R. Wanninkhof, P. Landschützer, B. R. Carter, and J. A. Triñanes

1) Introduction

The oceans play a major role in the global carbon cycle by taking up a significant fraction of the excess carbon dioxide that humans release into the atmosphere. As a consequence of humankind's collective release of CO_2 emissions into the atmosphere from fossil fuel burning, cement production, and land-use changes over the last two-and-a-half centuries, commonly referred to as "anthropogenic $CO_{2\,anth}$ (C)" emissions, the atmospheric CO_2 concentration has risen from pre-industrial levels of about 278 ppm (parts per million) to ~410 ppm in 2019. The atmospheric concentration of CO_2 is now 47% higher than preindustrial levels (Friedlingstein et al. 2019). As discussed in previous *State of the Climate* reports, marine C_{anth} is the major cause of anthropogenic ocean acidification. Here the discussion is updated to include recent estimates of the ocean C_{anth} sink. Over the last decade the global ocean has continued to take up a substantial fraction of the C_{anth} emissions and therefore is a major mediator of global climate change. Of the 11 (±0.9) Pg C yr–1 C_{anth} released during the period 2009–18, about 2.5 (±0.6) Pg C yr–1 (23%) accumulated in the ocean, 3.2 (±0.6) Pg C yr–1 (29%) accumulated on land, and 4.9 (±0.1) Pg C yr–1 (44%) remained in the atmosphere with an imbalance of 0.4 Pg C yr–1 (4%; Fig. 2 of Friedlingstein et al. 2019). This decadal ocean carbon uptake estimate is a consensus view from a combination of measured decadal CO_2 inventory changes, models, and global air–sea CO_2 flux estimates based on surface ocean partial pressure of CO_2 (pCO_2) measurements from ships and moorings. Using ocean circulation models that include biogeochemical parameterizations and inverse models that are validated against or fit to observed air–sea exchange fluxes and basin-scale ocean inventories, Friedlingstein et al. (2019) showed that the oceanic anthropogenic carbon sink has grown from 1.0 (±0.6) Pg C yr–1 in the decade of the 1960s to 2.6 (±0.6) Pg C yr–1 in 2018. Riverine contributions supply an additional 0.45 to 0.78 Pg C yr–1 of natural carbon to the ocean.

2) Air–sea carbon dioxide fluxes

Ocean uptake of CO_2 is estimated from the net air–sea CO_2 flux derived from the bulk flux formula with air–sea differences in CO_2 partial pressure (ΔpCO_2) and gas transfer coefficients as input. Gas transfer is parameterized with wind as described in Wanninkhof (2014). This provides a net flux estimate. To determine the C_{anth} fluxes into the ocean, several other processes need to be taken into account. A steady contribution of carbon from riverine runoff, originating from organic and inorganic detritus from land, recently revised upward from 0.45 to 0.78 Pg C yr–1 (Resplandy et al. 2018) needs to be included. Other factors, such as natural carbon deposition into/onto the sea floor and margins and natural variations in the balance of CO_2 between the atmosphere and ocean, are assumed to be small. C_{anth} is therefore defined as the sum of the net flux and the riverine contribution. The data sources for pCO_2 are annual updates of surface water pCO_2 observations from the Surface Ocean CO_2 Atlas (SOCAT) composed of mooring and ship-based observations (Bakker et al. 2016) and the Lamont-Doherty Earth Observatory (LDEO) database with ship-based observations (Takahashi et al. 2017). The increased observations and improved mapping techniques including neural network methods (Rödenbeck et al. 2015) provide annual global pCO_2 fields on a 1° latitude × 1° longitude grid at monthly time scales. This allows investigation of variability on sub-annual to decadal time scales.

The monthly 2019 ΔpCO_2 maps are based on the observation-trained neural network approach of Landschützer et al. (2013, 2014). The 2019 values are projections based on observed sea surface temperature (SST), sea surface salinity (SSS), satellite chlorophyll-*a*, and atmospheric CO_2 for 2019; climatological mixed layer depths (MLD); and a neural network approach for pCO_{2w} developed from the data from 1982 through January 2019. The 2019 estimate uses the monthly wind fields from 2018, but changes in winds over time have a small effect on annual global air–sea CO_2 fluxes (Wanninkhof and Triñanes 2017). The C_{anth} fluxes from 1982 to 2019 suggest a decreasing ocean sink in the first part of the record and a strong increase from 2001 onward that continued

unabated into 2019 with a 0.2 Pg C yr–1 increase from 2018 to the 2019 estimate (Fig. 3.26). The amplitude of seasonal variability is large (≈1 Pg C yr–1) compared to the long-term trend with minimum uptake in the June–September timeframe. The C_{anth} air–sea flux of 3.2 Pg C yr–1 in 2019 is 33% more than the revised 1997–2017 average of 2.40 (±0.46) Pg C yr–1.

The average fluxes in 2019 (Fig. 3.27a) show the characteristic pattern of effluxes (ocean-to-air fluxes) in the tropical regions, in coastal upwelling zones, and in the high-latitude Southern Ocean around 60°S. Coastal upwelling regions include the Arabian Sea, off the west coasts of North and South America, and the coast of Mauritania. The western Bering Sea in the northwest Pacific was a strong CO_2 source as well in 2019, particularly in the March–April timeframe. The region with the largest efflux is the upwelling region of the eastern equatorial Pacific. The regions of effluxes are significant CO_2 sources to the atmosphere. The primary uptake regions are in the subtropical and subpolar regions. The largest sinks are observed poleward of the sub-tropical fronts. The frontal positions determine the location of the maximum uptake. This position is farther south and weaker in the Pacific sector of the Southern Ocean compared to the other basins.

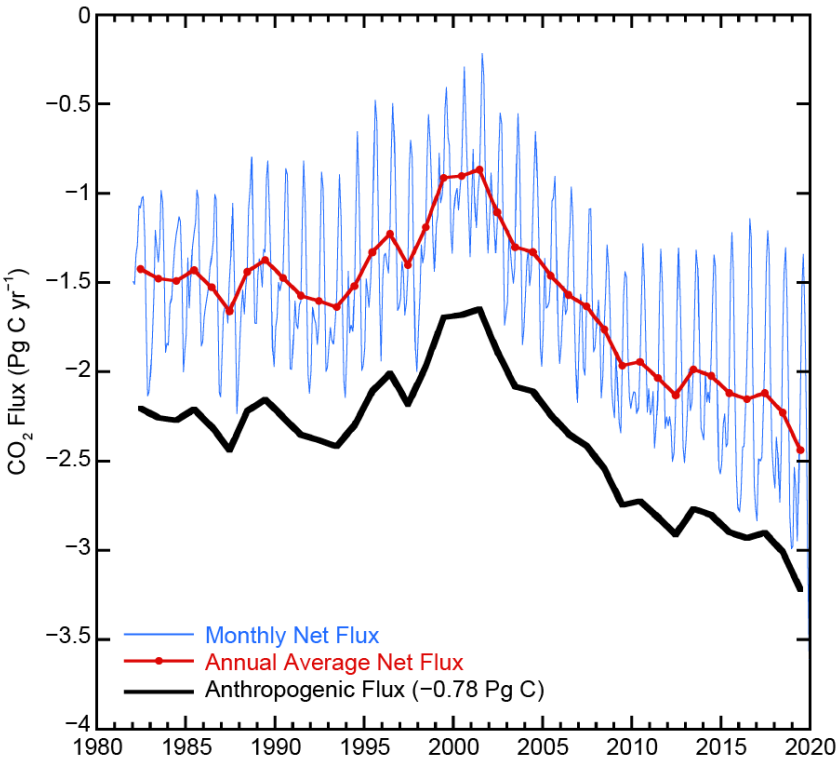

Fig. 3.26. Global annual (red line) and monthly (blue line) net CO_2 fluxes (Pg C yr–1) for 1982–2019. The black line is the anthropogenic CO_2 flux that is the net flux plus the riverine component. Negative values indicate CO_2 uptake by the ocean.

In the Northern Hemisphere (NH), there is a significant asymmetry in fluxes in the sub-Arctic gyre, with the North Atlantic being a large sink while the North Pacific is a source of CO_2. This is, in part, due to the position of the western boundary currents that are known CO_2 sinks at high latitudes. The Gulf Stream/North Atlantic Drift in the Atlantic extends farther north than the Kuroshio in the Pacific.

Ocean carbon uptake anomalies (Fig. 3.27c) in 2019 relative to the 1997–2017 average are attributed to the increasing ocean CO_2 uptake with time (Fig. 3.26) and to variations in large-scale climate modes. The long-term air–sea flux trend since the minimum uptake in 2000 is 0.75 Pg C $decade^{-1}$, which leads to greater ocean CO_2 uptake (blue colors in Fig. 3.27a). Despite this trend, there are several large regions showing positive anomalies (efflux) for 2019, notably the eastern equatorial Pacific, the sub-polar Northwest Pacific (centered at ≈ 40°N), and the high-latitude Southern Ocean. The increased effluxes in the eastern equatorial Pacific are related to a mostly negative sign of the Oceanic Niño Index (ONI) that followed an extensive period of predominantly positive ONI (i.e., more El Niño-like) conditions in the preceding 20 years. The neutral sea surface temperature anomaly (SSTA; see Fig. 3.1a) indicates normal upwelling of waters with high CO_2 content has returned after a period of lower-than-normal upwelling. Positive anomalies (efflux) in the northwest Pacific regions, including the western Bering Sea, are related to the positive SSTA over the past year compared to the long-term average (Fig. 3.27c).

The differences between the air–sea CO_2 fluxes in 2019 compared to 2018 (Fig. 3.27b) are relatively small compared to previous years with anomalies roughly in the same regions as the difference of 2019 from the 20-year average. This indicates that conditions in 2019 resemble conditions in 2018. The increase in CO_2 effluxes in the northwest Pacific from 2018 to 2019 are associated with increased temperature and associated increase in pCO_{2w} caused by the return of the marine heatwave in this area (see also Fig. SB3.1). The Southern Ocean (south of 40°S) shows a decreasing sink in the polar front region (≈50°S) and increasing source to the south for the Atlantic sector of the Southern Ocean compared to 2018. The correlations with SSTA (2019 minus 2018) are more nuanced. The large positive SSTAs in the northwest Pacific from 30° to 60°N are indicative of the warm water anomaly and associated positive CO_2 flux anomaly (efflux; Fig. 3.27b). The large negative CO_2 flux anomaly (uptake) in the southeastern Pacific has a positive SSTA associated with it, and the positive flux anomaly around 45°S in the South Atlantic is associated with a negative SSTA. These flux differences are not readily explained in terms of SSTA and suggest that in this band, SSTAs and flux anomalies are decoupled. The North Atlantic near Greenland shows a large increase in sink strength with a positive SSTA that again cannot be readily explained in terms of local SSTA. Rather, it appears that changes in the ocean currents and biological productivity changes between 2019 and 2018 are the cause of the greater uptake.

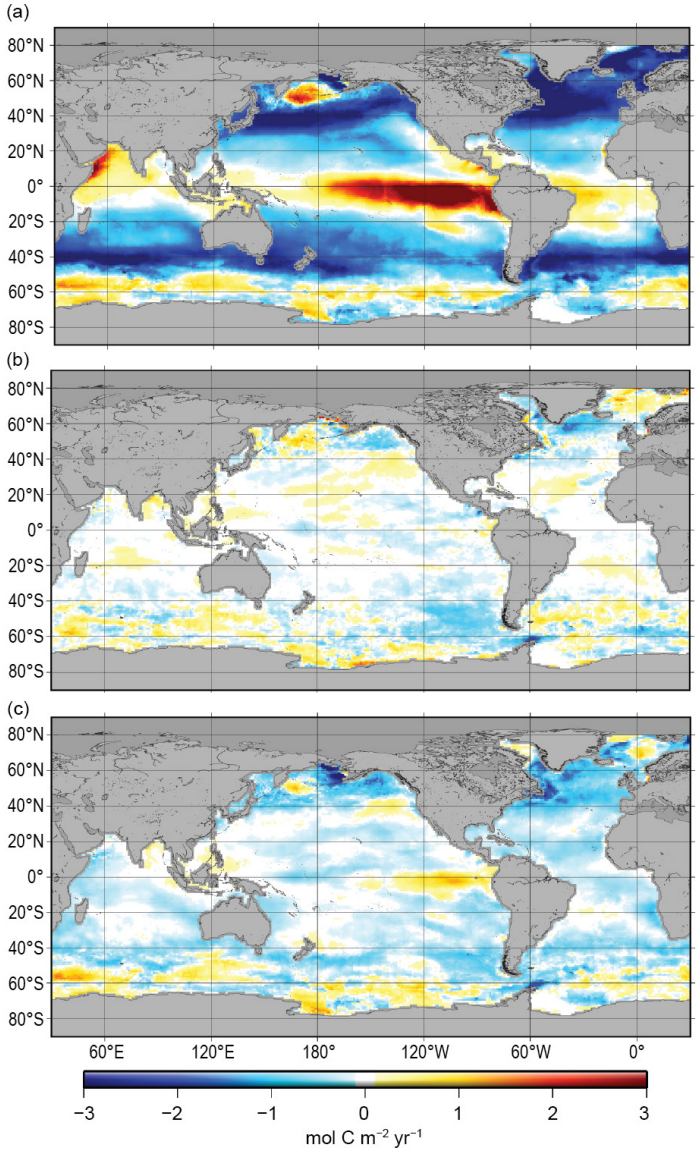

Fig. 3.27. Global map of (a) net air–sea CO_2 fluxes for 2019, with ocean CO_2 uptake regions shown in the blue colors, (b) net air–sea CO_2 flux anomalies for 2019 minus 2018 values following the method of Landschützer et al. (2013), and (c) net air–sea CO_2 flux anomalies for 2019 relative to a 1997–2017 average. All maps have units of mol C m^{-2} yr^{-1}.

Some of the pCO_2 and CO_2 flux anomalies can be attributed to variations in large-scale climate modes and associated physical anomalies, notably temperature, but the causality is often complex. For example, the behavior of pCO_2 with respect to temperature includes competing processes: thermodynamics dictate decreasing pCO_2 with decreasing SST, but waters originating from the deep with a cold temperature signal will have a high pCO_2. As the equilibration time of pCO_2 in surface seawater with atmospheric CO_2 is on the order of a year, CO_2 and CO_2 flux anomalies can be propagated by ocean currents. Moreover, the drawdown of pCO_2 due to biology is often associated with increasing temperature, but this depends on region and season. The strong trend of increasing CO_2 uptake since 2000–02 has continued through 2019, with an increase in 2019 of 0.2 Pg C yr–1 above the 2018 estimate. This increase meets the overall expectation that the ocean will remain an increasing sink if atmospheric CO_2 levels continue to rise. The sequestration of CO_2 by the ocean partially mitigates the atmospheric CO_2 rise but it comes at a cost of increased acidification of surface and subsurface waters (Feely et al., 2016; Carter et al. 2017; Lauvset et al. 2020).

3) Large-scale carbon and pH changes in the ocean interior

Global-scale CO_2 emissions from human activities are causing ocean interior C_{anth} increases and acidification. These large-scale changes can affect marine organisms and impact fisheries with implications for food security (Gattuso et al. 2015). Delineating how the biogeochemical processes in the ocean interior will be affected by the changing heat content and C_{anth} uptake is essential for developing future mitigation and adaptation responses to climate change. A major aim of the international Global Oceans Ship-based Investigations Program (GO-SHIP) is to determine the C_{anth} input to the ocean interior and the changing patterns of oceanic CO_2 over time (Talley et al. 2016; Sloyan et al. 2019). Field observations and inverse models have provided estimates of the uptake of C_{anth} into the ocean both over the last 250 years and over the last two decades. Simulations of C_{anth} inventories with models suggest that the ocean accumulated 24–34 Pg of C_{anth} between 1994 and 2007 (Gruber et al. 2019; Fig. 3.28a), accounting for about 25% of the total anthropogenic CO_2 emissions over that time period. This uptake has increased the total inventory of C_{anth} since 1750 from 118 ± 20 Pg C in 1994 to 170 ± 20 Pg C in 2018 (Sabine et al. 2004; Friedlingstein et al. 2019). Change in C_{anth} storage is determined by the change in C_{anth} between repeat surveys. This approach utilizes several newly developed methods and procedures for determining C_{anth} from the often much larger changes in the natural carbon content due to changes in transport ventilation and remineralization (e.g., Woosley et al. 2016; Clement and Gruber 2018; Carter et al. 2017, 2019). The approaches have been extended to allow for estimation of global ocean C_{anth} as well as extrapolation into coastal regions (Feely et al. 2016). These approaches have indicated that significant variability at interannual and decadal time scales occurs in some regions, particularly in the tropics due to El Niño–Southern Oscillation (ENSO) forcing, and in the subtropics and high-latitude regions due to changing ventilation processes that can alter the globally integrated sink (Carter et al. 2017, 2019; Rödenbeck et al. 2015; Landschützer et al. 2016; DeVries et al. 2017; Friedlingstein et al. 2019).

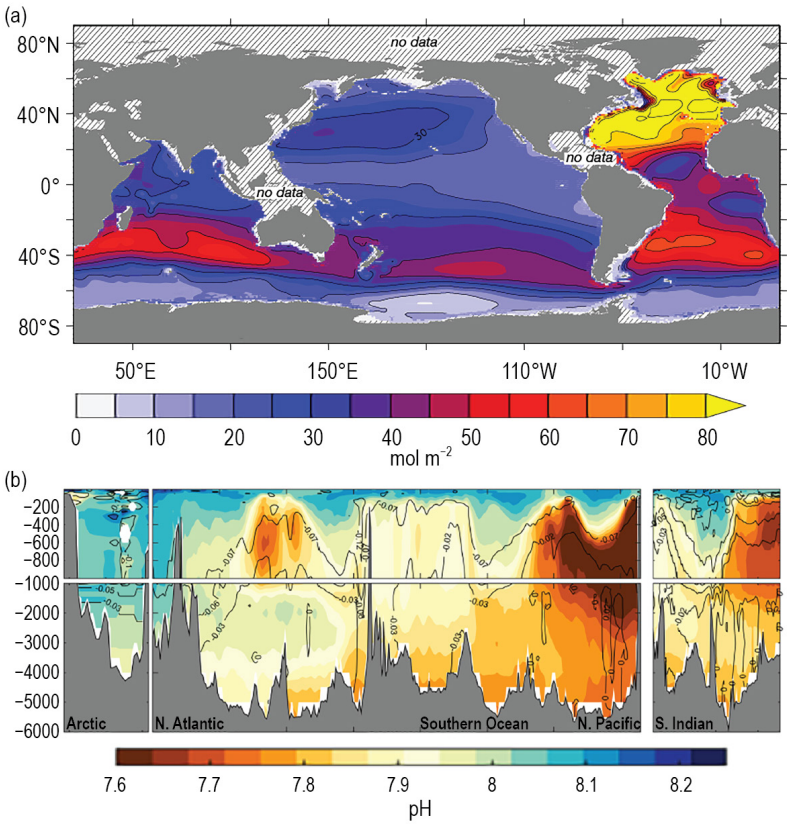

Fig. 3.28. (a) Change in full water column inventory of anthropogenic CO_2 in mol m^{-2} from 1994 to 2007, based largely on WOCE and GO-SHIP BGC data in the GLODAPv2 data product (modified from Gruber et al. 2019). (b) Vertical cross sections of pH (color) in the major ocean basins, from GO-SHIP transects from the Arctic (left) south through the Atlantic to the Southern Ocean (middle), then north through the Pacific along 152°W (middle, right) and north through the Indian Ocean along 85°E (right). The pH (total scale) is reported for in situ temperature and pressure and are normalized to year 2002 as in the GLODAPv2 data product (Lauvset et al. 2015). Anthropogenic change in pH from preindustrial to year 2002 is contoured (after Lauvset et al. 2020).

The GO-SHIP surveys have also been used to determine the long-term biogeochemical changes in carbonate chemistry including pH and calcium carbonate saturation state in the global oceans (Carter et al. 2017, 2019; Lauvset et al. 2015, 2020). From 1750 through 2018, surface ocean pH has declined by 0.018 ± 0.004 units decade^{-1} in 70% of the ocean basins (Fig. 3.28b), and the surface aragonite saturation state has fallen by an average rate of 0.34% per year, causing more stress on carbonate mineral-forming organisms. The sensitivity of pH to changing atmospheric CO_2

concentration increases as temperature decreases. Hence the magnitude of ΔpH is largest in cold high-latitude waters. Anthropogenic changes in pH are amplified at depths where pH is naturally lower and dissolved inorganic carbon (DIC) is naturally higher, implying a larger change in pCO_2 and pH for a given change in DIC. As atmospheric CO_2 concentration increases, changes in the carbonate system and the individual carbonate system species will be directly affected with the changing buffer capacity of seawater (Feely et al. 2018). Continued observations and modeling studies are needed to determine how oceans keep pace with the atmospheric CO_2 increase.

Sidebar 3.2: OceanObs'19 —S. CHIBA, M. DAI, T. LEE, E. LINDSTROM, N. ROME, S. SPEICH, M. VISBECK, AND W. YU

OceanObs: A thirty-year history

Every 10 years, the ocean-observing community convenes to evaluate opportunities for innovation and improved collaboration to sustain and enhance global observations of the ocean. The third, and most ambitious, community-driven conference—OceanObs'19—convened in Honolulu, Hawaii, on 16–20 September 2019. It brought together people from all over the world to communicate the decadal advances made in observing technologies and the remarkable science that observing networks have enabled—and to chart innovative solutions to society's growing needs for ocean information and ways in which collaborations can accelerate progress. The first OceanObs'99 conference, held October 1999 in Saint Raphaël, France, was a galvanizing force for ocean observations and climate. Ten years later, OceanObs'09, held September 2009 in Venice, Italy, moved the community toward a common vision for the acquisition of routine and sustained global information on the marine environment sufficient to meet society's needs for describing, understanding, and forecasting marine and climate variability and weather; sustainably managing living marine resources; and assessing longer-term trends.

OceanObs'19: An ocean of opportunity

OceanObs'19 assembled more than 1500 ocean scientists, engineers, and users of ocean observing technologies from 74 countries and across many disciplines. The community submitted 140 community white papers (CWPs) with over 2500 contributing authors. The conference goal was to improve governance of a global ocean observing system by improving advocacy, funding, and alignment with best practices, encompassed by the conference statement (www.oceanobs19.net/statement/) with the following key points:

1. Engage observers, data integrators, information providers, and users from the scientific, public, private, and policy sectors in the continuous process of planning, implementation and review of an integrated and effective ocean observing system;
2. Focus the ocean-observing system on addressing critical human needs, scientific understanding of the ocean and the linkages to the climate system, real-time ocean information services, and promotion of policies that sustain a healthy, biologically diverse, and resilient ocean ecosystem;
3. Harness the creativity of the academic research and engineering communities, and work in partnership with the private and public sectors to evolve sensors and platforms, better integrate observations, revolutionize information products about the ocean, increase efficiency, and reduce costs at each step of the ocean-observing value chain;
4. Advance the frontiers of ocean-observing capabilities from the coast to the deep ocean, all aspects of the marine biome, disease vectors, pollutants, and exchanges of energy, chemicals and biology at the boundaries between the ocean and air, seafloor, land, ice, freshwater, and human populated areas;
5. Improve the uptake of ocean data in models for understanding and forecasting of the Earth system;
6. Ensure that all elements of the observing system are interoperable and that data are managed wisely, guided by open data policies and that data are shared in a timely manner;

7. Use best practices, standards, formats, vocabularies, and the highest ethics in the collection and use of ocean data;
8. Involve the public through citizen-engaged observations, information products, outreach, and formal education programs;
9. Evolve ocean-observing governance to learn and share, coordinate, identify priorities, increase diversity, promote partnerships, and resolve conflicts through a process of continuing assessment to improve observing; and
10. Promote investments in ocean observing and information delivery and sustain support.

OceanObs'19: Ocean and climate observing focus

Two of the themes of OceanObs'19 focused on 1) climate change and variability and 2) ocean, weather, and climate forecasting. One of the primary recommendations is improving the connection between observations, models, and reanalysis to enhance our ability to detect, monitor, understand, and predict climate. Enhanced effort is needed to study oceanic physical processes and their relationships with the atmosphere, cryosphere, land, and biosphere to inform Earth prediction. These processes, linked to ocean circulation, heat, and carbon storage and exchange, among others, also deepen our understanding of the ocean's biogeochemical and ecosystem function. The progress since Ocean Obs'99 is reflected by the evolution from a platform-based ocean observing system to the current, integrated observing system featured in OceanObs'19. Meeting expanding end-user needs is the next major challenge facing our ocean and climate observing systems (e.g., Sloyan et al. 2019).

Forecasting abilities have progressed substantially over the past two decades thanks to the advances in ocean observing systems, prediction models, and data assimilation methods. Operational data streams, such as those from satellite altimetry and Argo profiling floats, have played key roles in these advances. Yet the ocean climate observing system must be sustained and evolved over long periods of time to adapt to new sampling needs and to take advantage of technological innovations. Ensuring better integration of data, technology, and standards also requires substantial coordination and capacity building across regional and international communities (Heimbach et al. 2019). These priorities will guide the actions of programs such as Global Ocean Observing System (GOOS) and OceanPredict to leverage the synergy of the integrated observing networks to maximize their value, improving services to users, and gaining scientific and technical efficiencies.

OceanObs living action plan

The OceanObs'19 organizers and sponsors will launch several efforts during 2020 and 2021 to facilitate ongoing post-conference actions by the community, in coordination with community organizations such as the Research Coordination Network, Global Climate Observing System (GCOS), GOOS, and Ocean Observations Panel for Climate. These efforts help determine more effective pathways for cooperation, sharing, and funding sustained and integrated ocean observations. The outcomes of this process will inform a growing GOOS and provide critical energy toward the United Nation's Decade of Ocean Science for Sustainable Development (2021–30).

All recommendations from the conference, including those from the CWPs, are being incorporated into a "Living Action Plan," which will organize outcomes from continuous engagement with the OceanObs community. This categorization is not meant to restrict or confine the substance of outcomes in any way; instead, the community will capture present and future aspirations of those involved in sustained ocean observing. The ultimate objective is to inform governance of the GOOS, mobilize communities of practice, and strengthen partnerships for enhanced ocean science and technology moving forward.

APPENDIX 1: Acronym List

ACC	Atlantic Circumpolar Current
AMO	Atlantic Multidecadal Oscillation
AMOC	Atlantic meridional overturning circulation
BAPG	Biogeochemical-Argo Planning Group
BASS	Blended Analysis of Surface Salinity
BGC	biogeochemical
CERES	Clouds and the Earth's Radiant Energy Systems
Chl*a*	chlorophyll-a
C_{phy}	phytoplanktonic carbon
CWPs	community white papers
DIC	dissolved inorganic carbon
DJF	December–February
DMI	Dipole Mode Index
DOISST	Daily Optimum Interpolation SST version 2
DWBC	Deep Western Boundary Current
E	evaporation
EBAF	Energy Balanced and Filled
EKE	eddy kinetic energy
ENSO	El Niño–Southern Oscillation
ERSSTv5	Extended Reconstruction Sea-Surface Temperature version 5
FC	Florida Current
FLASHFlux	Fast Longwave And Shortwave Radiative Fluxes
GCOS	Global Climate Observing System
GMSL	global mean sea level
GOOS	Global Ocean Observing System
GO-SHIP	Global Oceans Ship-based Investigations Program
GPCP	Global Precipitation Climatology Project
GRACE	Gravity Recovery and Climate Experiment
GRACE-FO	GRACE Follow-On
HadSST	U.K. Met Office Hadley Centre SST
IOD	Indian Ocean dipole
ITCZ	Intertropical Convergence Zone
JIMAR	Joint Institute for Marine and Atmospheric Research
JJA	June–August
JPL	Jet Propulsion Laboratory
LDEO	Lamont-Doherty Earth Observatory
LH	latent heat flux
LW	longwave radiation
MAM	March–May
MEI	Multivariate ENSO Index
MHHW	mean higher high water
MHT	meridional heat transports
MLD	mixed layer depths
MOC	meridional overturning circulation
NAO	North Atlantic Oscillation
NCP	net community production
NECC	North Equatorial Countercurrent

NH	Northern Hemisphere
NPP	net primary production
nSEC	northern core of the South Equatorial Current
OAFlux2	Objectively Analyzed air-sea Fluxes second generation
OCI	ocean color index
OHC	ocean heat content
OHCA	ocean heat content anomaly
ONI	Oceanic Niño Index
OSNAP	Overturning in the Subpolar North Atlantic Program
OSP	Ocean Station Papa
P	precipitation
PACE	Plankton, Aerosol, Cloud, ocean Ecosystem
PDO	Pacific Decadal Oscillation
PFZ	Polar Frontal Zone
PIES	pressure-equipped inverted echo sounders
PMEL	Precision Measurement Equipment Laboratory
PMM	Pacific Meridional Mode
ppm	parts per million
PSO	permanently stratified ocean
PSS-78	Practical Salinity Scale-78
Q_{net}	net surface heat flux
SAMBA	South AMOC Basin-wide Array
SH	sensible heat flux
SH	Southern Hemisphere
SMAP	Soil Moisture Active Passive
SMOS	Soil Moisture and Ocean Salinity
SOCAT	Surface Ocean CO_2 Atlas
SON	September–November
SPCZ	South Pacific Convergence Zone
SSM/I	Special Sensor Microwave Imager
SSS	sea surface salinity
SST	sea surface temperature
SSTA	sea surface temperature anomaly
std. dev.	standard deviation
SW	shortwave radiation
WOA13v2	World Ocean Atlas 2013 version 2
XBT	eXpendable BathyThermographs
ZJ	Zettajoules